DEVELOPMENT OF ADVANCED SPECTRALLY SELECTIVE COATING FOR THE APPLICATION OF ENERGY-EFFICIENT WINDOWS

SHEN BOXU

PhD

The Hong Kong Polytechnic University

2022

The Hong Kong Polytechnic University

Department of Building Environment and Energy Engineering

Development of Advanced Spectrally Selective Coating for The Application of Energy-efficient Windows

Shen Boxu

A thesis submitted in partial fulfillment of the requirements for
the Degree of Doctor of Philosophy
July 2021

CERTIFICATE OF ORIGINALITY

I hereby declare that this thesis is my own work and that, to the best of my knowledge and belief, it reproduces no materials previously published of written, nor material that has been accepted for the award of any other degree or diploma, except where due acknowledgement has been made in the next.

____ (Signed)

__________ SHEN BOXU ________________ (Name of student)

ABSTRACT

Abstract of thesis entitled: Development of advanced spectrally selective coating for the application of energy-efficient window

Submitted by: SHEN Boxu

For the degree of: Doctor of Philosophy

at The Hong Kong Polytechnic University in July 2021

The building sector makes up 36 % of the terminal energy use and accounts for 28 % of energy-related carbon emission in 2019. Heating, ventilation, and air conditioning (HVAC) systems in buildings contribute to about half of the energy used in buildings. Buildings in Hong Kong receive abundant of sunlight throughout the year, and sunlight flowing through windows is the primary source of heat gain in buildings. The transmittance of traditional soda-lime window glass for visible and near-infrared light is about 75 % to 90 % for the popular 4 mm thickness, indicating that the glazing lacks the spectrally selective property. Accordingly, strong solar radiation increases the indoor air temperature of buildings, which leads to the increase of air-conditioning energy consumption, especially for regions with cooling-demand climate. Thus, the development of spectrally selective material for energy-efficient glazing has been one of the effective means to reduce electricity consumption of air-conditioning and corresponding CO_2 emission. This thesis is to present my new contribution in this academic area.

Although Low-E glass exhibits quite good spectrally selective performance, the extra cost of one more glass pane and encapsulating configuration, complex fabrication procedure with slow

sputter rate and the use of noble metals make it hard to conduct window retrofit for existing buildings. Antimony-doped tin oxide nanocrystals (ATO) have been regarded as a promising alternative due to its low cost and good stability, which can effectively block the solar radiation of wavelength from 1500 nm to 2500 nm. One general trouble for the synthesis of ATO by the co-precipitation way is that nanoparticles often agglomerate micron-sized secondary particles during annealing process. In addition, the coating with the fillers of cesium doped hexagonal tungsten bronze nanocrystals (Cs-HTBs) has been proved that the Cs-HTBs-based film exhibited excellent near-infrared shielding property in the wavelength below 1500 nm. Specifically, the Cs-HTBs, which exhibit good spectral selectivity without the need for post-heating in a N_2/H_2 atmosphere, were frequently prepared via a one-pot approach employing WCl_6 and CsOH as raw materials. However, due to their greater price, inconvenient storage, and environmental pollution, WCl_6 and CsOH are not suitable for scaling up manufacturing.

This thesis aims to develop a new type of spectrally selective coating with superior near-infrared shielding performance by in-situ polymerization spraying process based on the functional nanofillers of ATO and Cs-HTBs. Firstly, a novel dual-titration co-precipitation method was developed for the synthesis of the scalable preparation of low-agglomerated ATO with high near-infrared shielding property. Specifically, two separating funnels were employed to load the Sn^{4+}/Sb^{3+} solution and $NH_3 \cdot H_2O$ precipitant respectively. After that, the liquid in the two separatory funnels was simultaneously dropped into the flask, while the blades of the mixer in the flask were stirred. The method is conducive to synthesize weakly agglomerated ATO nanoparticles to prevent optical distortion. The effects of pH value of the reaction system on the antimony doping level and optical performance of the ATO nanocrystals were investigated.

The size distribution and mean crystalline size were conducted by counting enough nanoparticles in the TEM images and using the Gaussian fitting function. The ATO nanoparticles prepared by the dual-titration method demonstrated lower agglomeration than the nanoparticles prepared by the traditional method, which is beneficial to reduce the optical scattering.

Secondly, a novel one-pot synthesis without post heat-treatment was developed for the scalable production of Cs-HTBs, using ammonium metatungstate hydrate (AMT) as the W source and cesium carbonate (Cs_2CO_3) as Cs source. The Cs_xWO_3 nanocrystals were prepared by ethanol with tartaric acid of 1 mol/L and a certain amount of chloroplatinic acid through one-pot method. The reducing mechanism of the tartaric acid and the tartaric acid with the assistance of the chloroplatinic acid for the synthesis of Cs_xWO_3 were studied. The relationships between the different reducing agents used in the synthetic process and the crystalline composition of the as-prepared nanocrystals were discussed and the possible synthesis mechanism was subsequently proposed. Besides, the impacts of charge carrier density and free carrier mobility on LSPR and small polaron transfer have been studied in length, as well as the method for boosting near-infrared shielding performance. The results indicate that tartaric acid with the presence of chloroplatinic acid could promote most W^{5+} ions in the hexagonal Cs_xWO_3 nanocrystals. Chloroplatinic acid has been shown to improve tartaric acid reducibility. In addition, Li, F-codoped Cs_xWO_3 nanocrystals have been successfully produced using a controlled one-pot approach for use in energy-efficient windows. which expands the spectral tunability of LSPR and small polaron transfer. The effects of Li and F on the phase composition, valence state distribution of W, optical properties and microstructure of the as-prepared

products have been investigated.

Finally, the new type of spectrally selective coating composed of ATO and Li, F-codoped Cs_xWO_3 nanocrystals as functional additives was developed via in-situ polymerization. Compared with the sputtering process of traditional Low-E coating, the spraying preparation is flexible and easily performed by manual operation which can prevent the complicated conditions like vacuum environment, sophisticated pre-process for glass surface and limited glazing size for depositing. The employment of spraying fabrication provides a more effective way to modify the window glazing that has been installed.

The established synthetic strategy is critical for increasing the scale of manufacturing of antimony-doped tin oxide and cesium tungsten bronze with superior near-infrared shielding performance and promoting its practical application in the field of energy-efficient glazing, which plays an important role for developing carbon neutral buildings in Hong Kong and other cities.

Keywords: Sb-doped SnO_2; Cs_xWO_3; spectral selectivity; localized surface plasmon resonance; small polaron transfer; spectrally selective coating; in-situ polymerization; spraying fabrication; energy-efficient windows

PUBLICATIONS DURING PHD STUDY

Journal papers:

[1] Shen B, Wang Y, Lu L, Yang H. Spraying fabrication of spectrally selective coating with improved near-infrared shielding performance for energy-efficient glazing. Ceramics International. 2021.

[2] Shen B, Wang Y, Lu L, Yang H. pH-dependent doping level and optical performance of antimony-doped tin oxide nanocrystals as nanofillers of spectrally selective coating for energy-efficient windows. Ceramics International. 2021.

[3] Shen B, Wang Y, Lu L, Yang H. Synthesis and characterization of Sb-doped SnO2 with high near-infrared shielding property for energy-efficient windows by a facile dual-titration co-precipitation method. Ceramics International. 2020;46:18518-25.

[4] Shen B, Wang Y, Lu L, Yang H. Novel one-pot synthesis and growth mechanism of hexagonal Cs_xWO_3 nanocrystals with superior near-infrared shielding property for energy-efficient windows. (Under preparation)

ACKNOWLEDGEMENTS

This thesis is an outcome of three years with considerable assistance and supports from a lot of people in different ways.

First and foremost, I want to convey my gratitude to Prof. Yang Hongxing, my chief supervisor, for his assistance, advice, and attention. Thank him for providing this opportunity of learning in PolyU to me and always giving me encouragements and support to get over the difficult problems. It is a great honor for me to undertake my research work in RERG.

My special tanks also go out to my co-supervisor Dr. Lu Lin and Dr. Wang Yuanhao for their insightful suggestions and help. I'd want to thank all of my RERG colleagues as well. Thank them for their help in life and spending wonderful time together.

Finally, but certainly not least, I want to express my gratitude to my family and girlfriend for their unwavering love and support. I won't be able to conclude my studies without their love. Thank you, and much love!

TABLE OF CONTENTS

LIST OF FIGURES

LIST OF TABLES

NOMENCLATURE

Abbreviations

NIR	Near-infrared radiation
UV	Ultraviolet
SEM	Scanning electron microscope
TEM	Transmission electron microscope
HRTEM	High resolution transmission microscope
SAED	Selected area electron diffraction
XRD	X-ray diffraction
ATO	Antimony-doped tin oxide
ITO	Tin-doped indium oxide
TCO	Transparent conducive oxides
SSMs	Spectrally selective materials
WPUA	Waterborne polyurethane acrylate
LSPR	Localized surface plasmon resonance
VB	Valence band
CB	Conduction band
XPS	X-ray photoelectron spectroscopy
VOC	Volatile organic compounds

Symbols

N	Free carrier density
m^*	Effective electron mass
e	Electron charge
ω_p	Collective electronic collective oscillation frequency

Chapter 1

Introduction

1.1 Background

HVAC (heating, ventilation, and air conditioning) systems account for roughly half of the energy consumed in buildings. Buildings in Hong Kong can receive enough of sunlight throughout the year, and sunlight flowing through windows is the primary source of heat gain in buildings. [1-3]. A window can be divided as two parts: the glazing material, which accounts for 80-90% of its area, and the framework, which is applied to sustain the glass pane on the building walls and to act as a peripheral seal. [4-7]

Glazing materials are increasingly used as an important component in modern construction industry for structural, aesthetic and daylight purposes as shown below.

1) For structural purpose: they can be easily installed in the walls at the construction site. Also, they are lightweight and easy to be cut into different shapes for various applications.
2) For aesthetic purpose: they can be applied to the specific architecture to satisfy its artistic styles.
3) For daylight purpose: they can let a large amount of solar light enter into the indoor environment and are also the bridge connecting inside and outside spaces to provide an external view for occupants.

Generally, the glazing used for windows refers to the soda-lime glass which is made of silica, sodium oxide, lime and small amount of other additives via floating process. Sunlight is made up of ultraviolet, visible, and near-infrared light with wavelengths ranging from 300 nm to 2500 nm. [7-9]. Among them, near-infrared radiation is invisible, accounting for about 50% of the total energy from the solar radiation. The transmittance of clear soda-lime glass for visible and near-infrared light is about 75 % to 90 % at 4 mm thickness, indicating that the glazing lacks the spectrally selective property. Accordingly, strong radiation can increase the indoor temperature in buildings, which leads to the increase of air-conditioning power consumption, especially for regions with cooling-demand climate [10-12].

Glass functionalization is usually realized by a thin film layer based on spectrally selective materials applied on the glazing surface. Therefore, the development of spectrally selective material for energy-efficient glazing has been one of the effective means to reduce electricity consumption of air-conditioning and corresponding CO_2 emission. So far, the most commonly used spectrally selective materials for energy-efficient glazing involve silver and transparent conductive oxides (TCOs). The most commercialized product on the market today is silver-based Low-Emissivity (Low-E) glass. The silver-based Low-E coating is fabricated using the vacuum sputter method, and the Low-E glass is made up of two glass panes to prevent the Low-E coating from being exposed to the ambient environment [13-17]. As for TCOs, tin doped indium oxide (ITO) and aluminum-doped zinc oxide (AZO) are most frequently reported spectrally selective materials for energy-efficient glazing. The requirements of the coatings to enhance the performance of glazing pane are as follows: (i) reduced transmittance in the range of near-infrared wavelength; (ii) high visible transmittance; (iii) a more cost-effective preparation technique [18-21].

To further achieve the above requirements, a novel combination of spectrally selective materials and in-situ polymerization fabrication technique have been developed. Antimony-doped tin oxide nanocrystals (ATO) have been regarded as a promising alternative due to its low cost and good stability, which can effectively block the solar radiation from 1500 nm to 2500 nm [22-36]. Besides, the coating with the fillers of cesium doped hexagonal tungsten bronze nanocrystals (Cs-HTBs) has been proved that the Cs-HTBs-based film exhibited excellent near-infrared shielding property in the wavelength below 1500 nm [37-51]. Consequently, comprehensive studies on the scalable synthesis of ATO and Cs-HTBs nanocrystals and spectrally selective mechanisms are required to promote the practical application of the spectrally selective coating in the field of energy-efficient windows.

1.2 Research gap

The most commonly used metal material for spectral selectivity is silver. Silver-based low-emissivity (low-E) glazing is composed of two glass panes for preventing the exposure of the low-E coating which is usually fabricated by magnetron sputtering method which requires expensive equipment and complex operating parameters. This type of energy-saving glass is not favorable for retrofitting the installed single-glazed windows due to its double structure. Metal oxides used for solar heat-shielding mainly refers to tin-doped indium oxide (ITO). However, ITO can only exhibit strong heat-shielding performance in part of near-infrared wavelength ranging from 1500 nm to 2500 nm and there is still high near-infrared transmittance in the wavelength below 1500 nm. Besides, indium is not very abundant and is expensive.

Consequently, antimony-doped tin oxide nanocrystals (ATO), a kind of relatively affordable TCO, have been regarded as a promising alternative due to its low cost and good stability. At present, the most widely used way for synthesizing ATO nanocrystals is the liquid-phase method, mainly including the co-precipitation method and the solvothermal method. The solvothermal method, despite showing the advantages of better control of the particle morphology and dispersibility, requires long reaction time and the extensive use of organic solvents (such as benzyl alcohol and toluene), which is not sufficient environmental-friendly. Besides, the output of the powder is limited by the size of the autoclave, which is hard to scale up the production. By contrast, the co-precipitation method is a more efficient way to prepare ATO nanocrystals, which is not time-consuming and avoids the large consumption of organic solvents [32]. In this method, $NH_3 \cdot H_2O$ was widely used as the precipitant for the formation of the tin/antimony hydroxide. However, few studies have been reported to discuss the effect of pH value for the reaction system on the antimony doping level and the optical performance of ATO nanocrystals.

Both of ITO and ATO can only exhibit strong heat-shielding performance in part of near-infrared wavelength ranging from 1500 nm to 2500 nm and there is still high near-infrared transmittance in the wavelength below 1500 nm. Cesium doped hexagonal tungsten bronze nanocrystals (Cs-HTBs) has been proved that the Cs-HTBs-based film exhibited excellent near-infrared shielding property in the wavelength below 1500 nm. At present, the synthesis of Cs-HTBs mainly includes solid-state reaction and liquid-phase method. Generally, Cs-HTBs prepared by conventional solid-state reaction requires a heat-treatment in H_2/N_2 mixed atmosphere, but the high reaction temperature tends to cause a larger and uneven particle size, which is adverse to the dispersion of Cs-HTBs and the optical property of their film. The conventional solid-state reaction is also considered to be dangerous due to the use of H_2 which is flammable and explosive. Furthermore, Cs-HTBs can be synthesized using the solvothermal method with WCl_6 and $CsOH•H_2O$ as starting materials. Although this method avoids the post heat-treatment in the dangerous atmosphere, the starting materials are not favorable for scalable work because of high cost, inconvenient storage and not enough environment-friendly. In addition, the synthesis of Cs-HTBs has been investigated by liquid-phase method using $Na_2WO_4•H_2O$ and Cs_2SO_4 as starting materials. Although the inexpensive and stable raw materials are suitable for industrial application, a pretreatment for $Na_2WO_4•H_2O$ to obtain the gel-like tungstate acid suspension and post heat-treatment are still required. The pretreatment in this method will increase cost, and the post heat-treatment can cause secondary growth of Cs-HTBs which is not favorable for its optical performance.

Furthermore, the spectrally selective coatings based on the nanoparticles are usually prepared via spinning and rolling method. However, spinning coating is a lab-scale method and rolling coating is not conductive to obtain an even coating surface. Simple and accessible deposition methods are important not only for academic study but also for industrial use.

1.3 Research aims and objectives

Concerns on reducing energy consumption and emission of greenhouse gas have led to continuous efforts to develop novel materials with spectral selectivity for windows. The energy-efficient windows with ideal spectrally selective coating can shield most of the near-infrared radiation and maintain a high visible transmittance. However, such techniques are less well studied. This thesis aims to develop a new type of spectrally selective coating with superior near-infrared shielding performance by in-situ polymerization spraying process based on the functional nanofillers of ATO and Cs-HTBs.

To achieve the above aims, the objectives are summarized as follows:

1) To understand the research status and optical properties of spectrally selective materials as well as the performance of employing them to glass surface, a comprehensive review of main types of spectrally selective materials is accomplished.

2) To solve the nanoparticle agglomeration after annealing treatment and examine the main factor affecting the Sb doping level, a facile dual-titration co-precipitation method was developed to reduce the agglomerated extent caused by the annealing processing. Besides, the influence of the pH titration endpoint on doping level and optical performance is systematically studied.

3) To realize the mass production of Cs-HTBs, a controllable one-pot synthetic method without post heat treatment was developed using ammonium metatungstate hydrate (AMT) as the W source and cesium carbonate (Cs_2CO_3) as the Cs source. For the synthesis of Cs-HTBs, the reducing mechanism of tartaric acid and tartaric acid with the help of chloroplatinic acid is investigated.

4) To further improve the optical performance of Cs-HTBs, a controllable one-pot method was used to successfully synthesize Li, F-codoped Cs_xWO_3 nanocrystals. The effects of charge carrier density and free carrier mobility on LSPR and small polaron transfer, as well as the detailed mechanism for improving near-infrared shielding performance, have been discussed.

5) To apply the spectrally selective coating to the retrofitting of the existing windows, a facile spraying deposition technique was presented, which is flexible and easily performed by manual operating.

6) To simultaneously achieve multifunction besides energy-saving, the spectrally selective coating was combined with g-C_3N_4 to realize photocatalytic activity and energy-saving at the

same time, which can promote the commercialization of the multifunctional glass.

Chapter 2

Literature review on spectrally selective materials

2.1 Introduction

Building energy consumption accounts for nearly 40% of total energy consumption in developed countries. HVAC (heating, ventilation, and air conditioning) systems account for nearly half of the energy used in construction. The transmittance of the ordinary glass for visible and near-infrared light is about 75 % to 90 %, indicating that the glazing lacks the spectrally selective property. Accordingly, it is necessary to develop spectrally selective materials, which can not only shield most of the near-infrared radiation, but also maintain a high visible transmittance. This chapter introduces typical categories of spectrally selective materials and describes their preparation method in terms of optical properties and deposition techniques as well as their application to buildings.

2.2 Classification and preparation methods

Spectrally selective materials (SSMs) are always assembled with glazing materials. SSMs are usually classified into three types, namely metal, metal oxides and metalloid. This section studies the SSMs from the viewpoint of synthetic methods and morphologies.

2.2.1 Metal-based SSMs

Over the last decades, several metals have been used in the field of solar filter through their solar reflection property. Solar radiation penetrating the indoor environment can be reflected to the external environment by using such SSMs, which reduces the cooling loads of the energy consumption in buildings. Silver (Ag) and gold (Au) are the widely used metals to achieve spectral selectivity and numerous researches have been conducted. For instance, chemical vapor deposition (CVD) technique was utilized to fabricate the gold coating on the surface of the glass panel [52]. The deposition process was conducted in a horizontal-bed reactor. The morphology of the as-prepared coating varied with different reaction temperature. A gold layer was formed and deposited at 500 °C (Figure 2.1a) while gold nanoparticles were formed and deposited at 450 °C (Figure 2.1b, c). Thermophoresis is thought to have a significant impact on particle size, implying that the gold atoms aggregated and formed nanoclusters in gas-phase reaction. In another research, thin silver layer was fabricated on the glazing surface through electron beam evaporation [53]. It is found that the as-prepared film was homogeneous with nanoparticles ranging from 4 to 9 nm (Figure 2.1d).

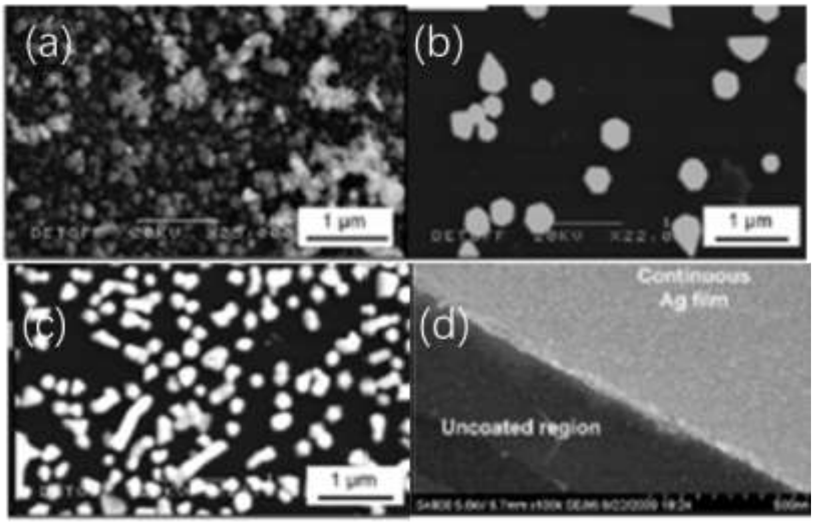

Figure 2.1 (a-c) SEM images of Au deposited on the surface of the substrate at different temperature, (d) SEM image of Ag layer with a Ge wetting layer.

Nevertheless, it is not stable to directly use Au and Ag in practical applications because of their ease to oxidize, especially used on the glass surface of windows exposed to the ambient environment. To overcome this defect, core-shell structure of the nanoparticles was achieved through surface modification. The silica shell structure was coated under room temperature by a continuous and scalable process in aqueous solution. The existence of the shell structure formed by silica can protect the metal core from the ambient exposure to realize durable performance. Thus, core-shell preparation method is conducive to promote the practical application for metal SSMs with durable high performance. Moreover, some studies concerning the reduction of particle agglomeration were carried out. It is reported that titanium oxide (TiO_2) was successfully prepared on the gold with different morphology, including nanoparticles, short nanorods and long nanorods (Figure 2.2). The nanoparticles and long nanorods demonstrated more stable structure compared with the short nanorods structure. On one side of the Au core, a thin TiO_2 shell layer was prepared, while the opposite side was coated with a thick shell. The as-prepared structure with anisotropic endued superior durability against dissolution and agglomeration, which facilitates its practical application in buildings.

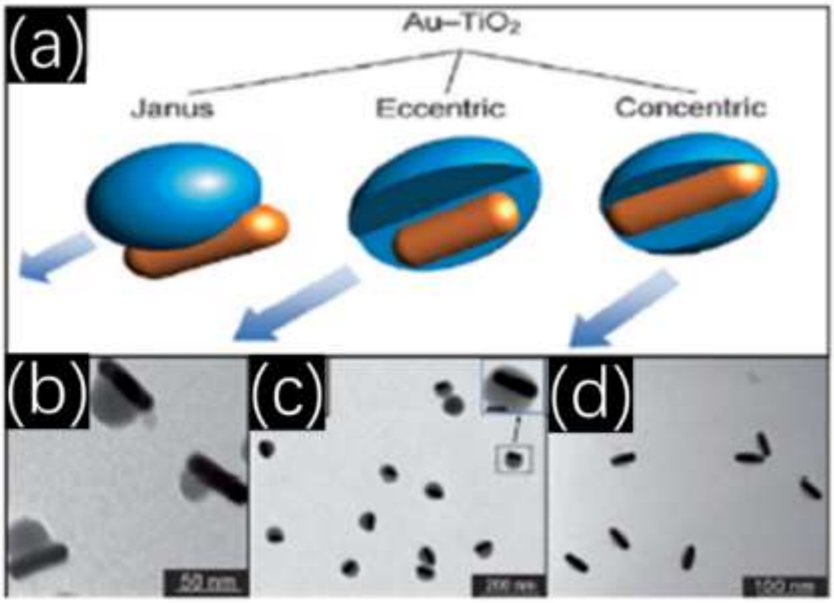

Figure 2.2 (a) Schematic diagram of Au@TiO_2 nanorods with different morphology, (b-d) TEM images of Au@TiO_2 with different morphology.

2.2.2 Metal oxide-based SSMs

Metal oxide of SSMs are steadier without the issues of oxidation and have been broadly studied, which can also be referred to as transparent conducive oxides (TCOs). The most widely used metal oxide of SSMs involves indium oxide, zinc oxide, tin oxide and tungsten trioxide, which shows superior optical properties through suitable impurity doping.

Until now, ITO is one of the most popular used for spectral selectivity of glazing materials. Generally, the molar ratio of Sn/In in ITO is 10 % and numerous studies have been conducted to improve the optical performance of ITO. For example, it was reported that ITO nanocrystals with a size of 10-20 nm were comprised into niobium (NbO_x) glazing and evenly distributed on the pane. Recently, another similar research reported that ITO nanocrystals showed superior near-infrared modulation under the stimulation of voltage. ITO nanocrystals were mainly synthesized by liquid phase reaction and the resultant nanocrystals were deposited on the glazing surface to form spectrally selective films by spin-coating. The ITO coating demonstrated homogeneous surface morphology with average nanocrystal size of 5 nm. In addition, a composite coating with excellent near-infrared shielding performance was prepared by combining ITO nanocrystals and polyurethane. The typical process steps are as follows. In the Teflon-lined autoclave, the indium and tin precursors were mixed with ethanol and heated at 220 °C for 8 hours. The resultant ITO nanocrystals were obtained via the centrifugation and showed flower-like morphology with uniform distribution. Besides the same precursors used, the addition of oleylamine prompted to from the highly transparent composite coating through thermal decomposition.

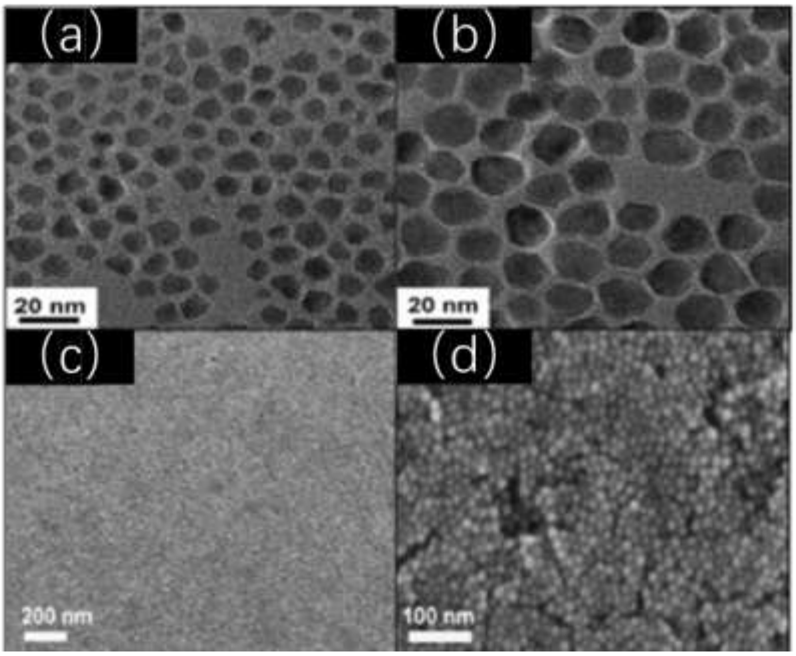

Figure 2.3 (a-b) TEM images of AZO nanocrystals, (c-d) SEM images of AZO thin film.

To date, doping strategy has been used to change the optical properties of zinc oxide (ZnO) in many studies, involving impurity of gallium (Ga) and aluminium (Al) [54]. For example, nanoscale gallium zinc oxide (GZO) particles were successfully prepared using zinc acetate and gallium salts as precursors in a precipitation method. The GZO dispersion was prepared by ultrasonic process. The average size of the GZO nanocrystals in the dispersion was 10-15 nm (Figure 2.3a, b). Besides, aluminium zinc oxide (AZO) has gotten a lot of attention as a result of its lower cost and less toxic in recent years. It was reported that controllable synthesis of AZO nanocrystals was successfully developed and the effect of doping level on optical performance was investigated. The resultant AZO nanocrystals showed spherical shape with diameters ranging from 15 to 25 nm. The AZO film was prepared by solution casting (Figure 2.3c, d). In another research, the homogeneous precipitation method was used to make AZO nanocrystals, which were then annealed at temperatures ranging from 200 to 700 °C. The epoxy resin was selected as film-forming agent and mixed with curing agent. The final composite coating was cured at 130 ℃ for 2 h.

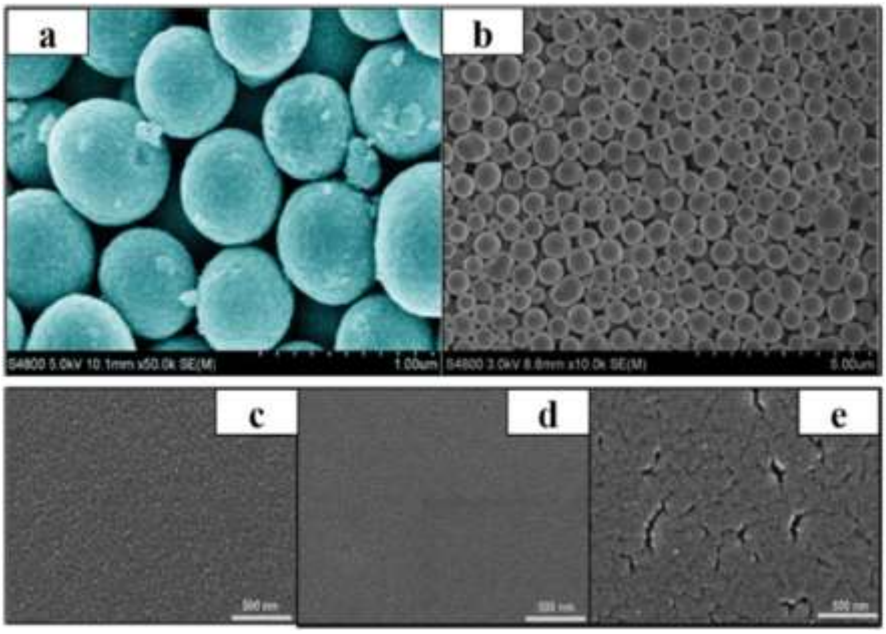

Figure 2.4 (a-b) SEM images of ATO prepared through high temperature annealing, (c-e) SEM images of ATO films prepared by the dispersions with different solid content.

Another popular metal oxide for preparing SSMs is antimony tin oxide (ATO) [23, 24, 27, 30, 32, 33, 55-60]. Generally, typical synthesis steps of SnO_2 are as follows. Tin chloride pentahydrate and a small amount of polyethylene glycol (PEG) were added into absolute ethanol, followed by the drop of ammonia until the pH of the solution reaching 9. Following that, the as-prepared products were centrifuged and rinsed three times with ethanol. Ammonia is found to have a significant impact on the morphology of the products. In this synthetic process, SnO_2 took on a sphere-like shape with a particle size of around 10 nm. ATO can be synthesized by introducing antimony in the crystal lattice of SnO_2. The molar ratio of Sb/Sn is around 10 % in ATO nanocrystals. It was reported that ATO hollow nanospheres were successfully prepared by solvothermal method with the existence of polyvinylpyrrolidone. Tin chloride pentahydrate and antimony chloride were added to methanol and heated for 6 hours at

180 °C. The final products were obtained by centrifuging the precipitate and annealing it at 500 °C for 2 hours. (Figure 2.4a,b). The as-prepared ATO nanospheres exhibited the diameter ranging from 200 to 800 nm. Besides, a sol-gel method was used to prepare ATO nanoparticles. The same Sn and Sb precursor were mixed in hydrochloric solution and the resultant solution were casted on the substrate surface by dip coating. After annealing the glazing sample, the ATO coating was fabricated and demonstrated homogeneous surface morphology without obvious defects compared with the coatings prepared by other methods (Figure 2.4c, d).

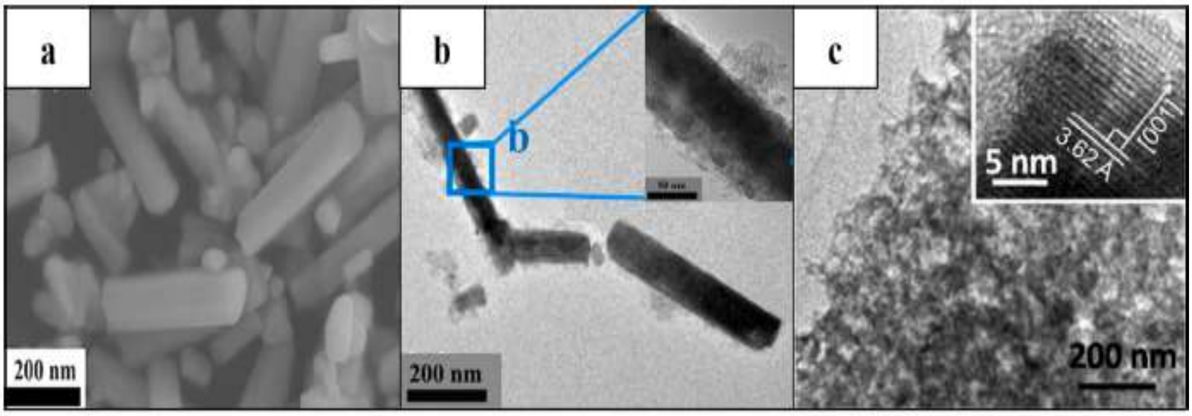

Figure 2.5 (a) SEM images,(b) TEM image and (c) HRTEM image of K_xWO_3 nanocrystals.

Tungsten bronze (M_xWO_3) Tungsten bronze refers to doped tungsten trioxide and is expressed as M_xWO_3 (M = Na, K, Rb and Cs). The near-infrared shielding performance can be enhanced with the increase of the impurity doping, which attributes to the increase of the electrons contributed by the alkali metal [37, 42, 43, 48, 51, 61-72]. For instance, cesium tungsten bronze with nanorod shape was synthesized by solvothermal reaction. Cesium hydroxide and tungsten hexachloride were mixed in the absolute ethanol and then transferred into Teflon-lined autoclave. The precursors in the autoclave were heated at 240 °C for 24 h. The resultant products were collected by the centrifugation and the size distribution of the nanoparticles was in the range of 60-100 nm. Moreover, rubidium tungsten bronze was prepared in another research. Cesium hydroxide was replaced by rubidium hydroxide in the solvothermal process. It is found that the as-prepared Rb_xWO_3 demonstrated rod-like morphology and the addition of acetic acid played a significant role on the particle size. Besides, tungsten bronze can be combined with other functional nanoparticles to obtain synergistic effect. It has been reported that Cs_xWO_3 were integrated with ZnO and deposited on the surface of the substrate to achieve dual function. Likewise, SiO_2 was combined with Cs_xWO_3 to enhance the optical stability with superior near-infrared shielding property. In this study, Cs_xWO_3 was prepared using cesium carbonate and tungsten trioxide and then mixed with tetraethoxysilane (TEOS) to fabricate composite coating. It is found that the core-shell structure of Cs_xWO_3/SiO_2 exhibited uniform particle size distribution less than 60 nm. Furthermore, the combination of K_xWO_3 and TiO_2 simultaneously realized spectral selectivity and photocatalysis. The as-synthesized K_xWO_3 nanocrystals showed rod-like shape with the size ranging from 200 nm to 400 nm. In addition, it can be seen that TiO_2 intimately contacted with K_xWO_3 nanocrystals surface (Figure 2.5).

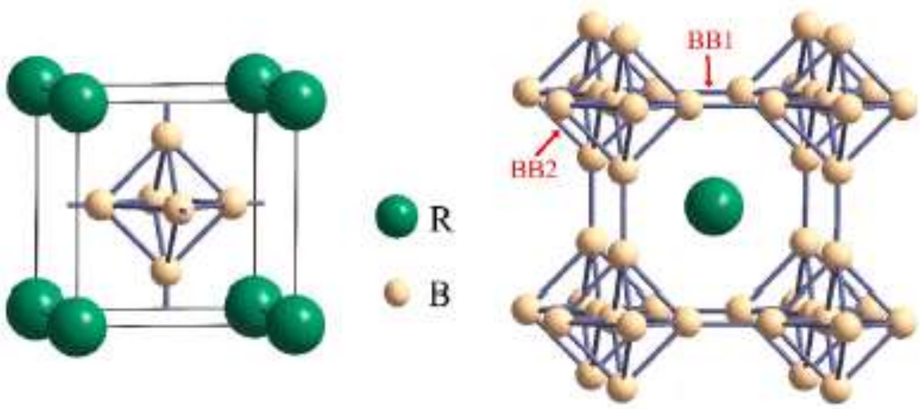

Figure 2.6 Schematic diagram of RB_6 crystal structure.

2.2.3 Metalloid-based SSMs

Rare-earth hexachloride (RB_6) has attracted great attention due to its unique optical performance (Figure 2.6). The majority of the rare-earth elements in the RB_6 compounds are trivalent (including La, Ce, Pr, Nd). SSMs such as lanthanum hexaboride (LaB_6) exhibit strong localized surface plasmon resonance (LSPR) [73-76]. With the presence of cetyltrimethylammonium bromide, LaB_6 nanoparticles were successfully dispersed in aqueous solution (CTAB). The LaB_6 composite coating was then created using the sol-gel method. The particle size of LaB_6 nanoparticles in the dispersion was found to range from 50 nm to 250 nm. Moreover, the composite coating combined with LaB_6 and ITO was fabricated by solution casting with the film former polyvinyl-butyral (PVB). It is obtained that the two kinds of particles were evenly dispersed in the PVB substrate and the average diameter of them were in the range of 80-120 nm and 20-30 nm respectively.

2.3 Electronic and optical properties of TCOs for consideration

This section presents the comprehensive theories and mechanism on the optical properties of TCOs [77].

2.3.1 Electronic properties

Electrical conductivity is a considerable property of TCOs and the understanding of electronic properties in materials is necessary. Electrical conductivity (σ) is expressed as:

$$\sigma = Ne\mu \tag{2.1}$$

Where N stands for carrier concentration, e for carrier charge, and is for carrier mobility. The fundamental charge of an electron is 1.6×10^{-19} C in general. It can be obtained from equation

(2.1) that the electric conductivity is determined by two factors, namely carrier mobility and free charge density. Mobility can be explained as the case where carriers can move through the materials. It is defined as:

$$\mu = \frac{e\tau}{m*} \tag{2.2}$$

Where τ is the average scattering time and $m*$ is the carrier effective mass. As shown in equation (2.2), It can be seen that by increasing the average scattering time, the mobility can be increased. Generally, a decrease of mobility can be achieved through decreasing the scattering time. The whole scattering degree is affected by ionized impurity scattering and acoustic phonon scattering. Besides, phase separation and porosity.

Free carriers are generated both intrinsically and extrinsically. Specifically, all the lattices are hold and all the electrons occupy the energy level of ground state, when there is no defect in the materials. Nevertheless, the introduction of defects (interstitials and vacancies) driven by entropy can generate free carriers at the temperature above 0 K. The following reaction formula describes the generated process for oxides:

$$O^{x}o \rightarrow 1/2O_{2}(g) + Vo + 2e' \tag{2.3}$$

Where Vo is the oxygen vacancies and e' denotes the free electrons. It can be obtained that the reductant environment with a reduced oxygen partial pressure can facilitate the increase of the material conductivity by generating more free electrons. In addition, free carriers can also be introduced by impurity doping with both interstitial and substitutional atoms.

Semiconductor materials are classified as p-type or n-type depending on whether the main contributor is holes or free electrons. Due to the existence of oxygen vacancies, n-type system is the dominant form. By contrast, p-type system materials undergo low conductivity.

A forbidden energy domain referred to as the band gap separates the valence band and conduction band. Generally speaking, the band gap of most metal oxides of SSMs with high visible transmittance is larger than 3 eV. For instance, zinc oxide is of a band gap of 3.4 eV.

2.3.2 Optical properties

The optical properties of metal oxides of SSMs intimately depend on their electronic properties. According to the Drude free electron model, the electric field of solar radiation can interact with the electrons of the materials . The transmittance, reflectance and absorption spectra of a typical TCO are well demonstrated. The spectra consist of three diverse regions. Specifically, high visible transmittance is necessarily required and the radiation with energy over the band gap can be adsorbed in the band transition. Therefore, a typical TCO should be of a suitable band gap over 3 eV. Besides, a decrease of transmittance in the wavelength higher than 800 nm can be observed. This phenomenon, leading to a strong absorption, is described as localized surface plasmon resonance (LSPR) [78-84]. The plasma frequency (λ_p) indicates the frequency of the solar radiation which equals to the frequency of the collective oscillation of the free electrons in the TCOs. The free electrons oscillating with electric field released by sunlight lead to the absorption. For the wavelength shorter than λ_p, the solar radiation can propagate through the TCO, leading to high visible transmittance. When the wavelength longer than λ_p, the wavelength tends to decay and leads to reflection tendency. The relationship between plasma wavelength and free carrier density can be described as $\lambda = 1/\sqrt{N}$. Thereby, a compromise exists between visible transmittance and free carrier density.

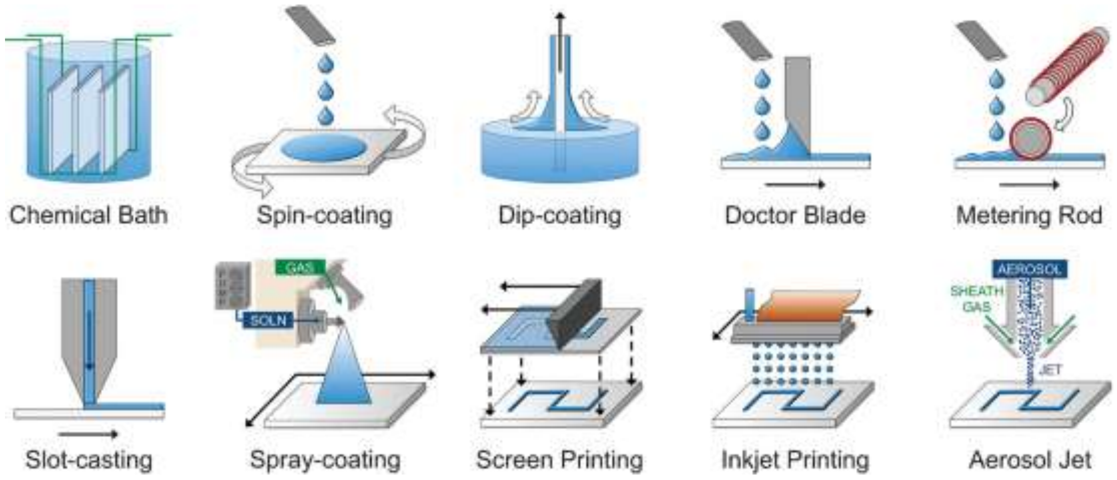

Figure 2.7 Schematic diagram of different deposition techniques [52].

2.4 Thin film deposition methods

Wet chemical routes allow for the deposition of thin films with affordable equipment cost [5, 20, 85-89]. An effective deposition technique can achieve uniform coverage which is important for practical application in buildings. In this section, several solution routes have been summarized (Figure 2.7). The solution deposition routes can be classified as two categories: direct growth of the thin film on the substrate and liquid coating that is based on metal-organic solution and nanoparticle suspensions. In addition, the solvent used in the solution system has a significant impact on the deposition routes. Because water is both environmentally friendly and cost-effective, the aqueous solution system is more popular. Nevertheless, some organic solvents are usually employed to enhance the solubility and adjust the solution properties for deposition process. Moreover, there is a tradeoff between the viscosity and volatility. Generally speaking, the solvent with high molecular weight tends to be of a high viscosity and is hard to be volatilized for removing by mild heat treatment. In turn, the solvent easily volatilized tends to be of a low molecular weight. The solvent is selected according to the deposition route used.

2.4.1 Direct growth

Direct growth technique involves chemical bath deposition and spray pyrolysis [24, 50, 90-94]. Chemical bath deposition depends on the controllable reaction and the reagent. When the substrate is immersed in the chemical bath, film growth occurs on the surface. Chemical bath deposition has the disadvantage of producing a large amount of waste solution. Chemical bath deposition mechanisms and chemistries for a variety of metal oxides are investigated further.

2.4.2 Liquid coating

The thin films of transparent conductive oxides are popularly by liquid coating routes. These routes rely on the characteristics of the solution formulas. Generally, the deposition process begins with a precursor and suitable chemical reagent containing the substances of interest to form the desired products. Liquid coating routes for the deposition of thin films use acetates, nitrates or chlorides as precursors as the costs of these chemicals are cheap and easily obtained from the suppliers. When the precursors are confirmed, the solution formula are determined. Typically, there are two kinds of formulas, including metal-organic solution (MOS) and nanoparticle dispersions with their own advantages and disadvantages.

Metal-organic solution (MOS) is the preferable method to prepare dense thin films. Typically, metal-organic salts can be dissolved in the solvent and blended with desired chemical stoichiometry. The compounds in the solution system resemble the starting precursors if no oligomerization occurs. The thermal processing can remove the useless organics and generate oxide phase. Dense films based on MOS formula can be chemically obtained by sol-gel method [86, 95-101]. In typical sol-gel steps, the precursors go through hydrolysis and condensation process in the MOS to yield a stable suspension with colloidal particles (sol state) and change towards solid network (gel state). The gelation reaction also known as aging process can link metal composition by condensation reaction involving the elimination of alcohol or water. When the metal-oxygen linkages are formed in the solution, the amount of organics can be reduced before the deposition process with the thermal treatment. Another film deposition technique based on MOS formula is Pechini method which was presented by Pechini in 1967. Metal ions provided by the starting precursors involving nitrates and carbonates are chelated in the solution with citric acid. With the existence of ethylene glycol, ester linkages can be created after heating treatment, because the carboxylate groups provided by citric acid allow the occurrence of chelation and poly-esterification reactions. The resultant polymer made of metal ions is spread in the matrix. Although the starting precursors used for Penichi method are cheaper than alkoxides, the larger content of organics can cause undesired carbon remains.

Three purposes of thermal treatment are as follows: decomposing the organics, inducing high crystallization or phase transformation. For MOS route, the formation of the thin film usually requires a thermal processing procedure to decompose the precursors in the solution. Here, the step of thermal decomposition is more accurately called thermolysis. Pyrolysis often refers to the high temperature decomposition process without oxygen. Specifically, thermal treatment can be carried out by a plate device with heating function or a tube furnace. Thermal treatment with adequate temperature can prompt the crystallization during the decomposition process. The film morphology of titanite materials and the effects of reaction conditions on crystallization have been reviewed in detail by Schwartz [102]. As described above, thermal treatment in a reduced oxygen partial pressure atmosphere (such as H_2 and N_2) can enhance the conductivity of transparent conducive oxides by increasing more free charge carriers. Even if the desired phase has been obtained by spray pyrolysis, it still needs a secondary annealing with reduced atmosphere to improve the electrical performance.

Nanoparticle dispersions can prevent overly thermal processing because the functional materials have already been synthesized. A detailed review of the fabrication of colloidal nanocrystals was presented for electronic applications. The synthetic routes without surfactants have been systematically reviewed by Pinna [103]. Nanoparticle dispersions with high solid contents usually suffer agglomeration problems and the nanoparticles can clog the nozzles for spraying fabrication. If a dense state is required instead of a network state, stabilizers and high temperature treatment are required.

Alternatively, a hybrid MOS-nanoparticle system can combine the merits of both deposition routes. The film stress and cracking can be minimized due to the existence of pre-synthesized nanoparticles. The binding components can be dissolved in the solution system without organics binders.

The aims of thermal treatment for nanoparticle suspension route are curing and sintering respectively. The curing temperature is explained as particles losing the organic capping shell and forming solid state medium. If dense thin film is further required, sintering process with a high temperature can induce a dense state rather than network structure.

2.4.3 Deposition techniques

Spin-coating is mainly utilized for lab scale processing because of its reproducibility and simplicity. In this process, the small glass sample is fixed to the chuck using a vacuum pump and excessive solution is dripped down to the sample surface [104, 105]. After that, the glass sample is rapidly rotated (usually to several 1000 RPM), which can guide the solution flow radially outward. A thin film is obtained after the solvent evaporation.

Dip-coating can entrain a thin layer on the substrate from a beaker with the solution. A comprehensive overview of the factors has been completed [106]. It is worth noting that dip-coating can lead coverage on both sides of the glazing sample. As a result, the two sides of the glass sample can be covered by identical thin films for specific requirements.

Doctor-blade and metering rod can also prepare the thin films by distributing and smoothing the solution. For the way of doctor-blade, the gap between the substrate and blade determines the thickness of the as-prepared films [107]. Besides, a metering rod with twining wire (also referred to as Mayer rod) is utilized to prepare thin films. During the process of metering rod, the solution left on the glass surface depends on the diameter of the wire on the metering rod.

Slot-casting can spread the solution on the substrate surface using a slotted head. During the casting process, the extrusion speed has to be lower than the line speed, which guarantees the film thickness thinner than the width of the slotted head [19, 108]. This technique can be employed for the solution with high viscosity and scaled to the continuous roll-to-roll production line.

Spray-coating technique has attracted great attention for non-contact and scalable deposition. This technique can be utilized as either a liquid coating deposition or the direct growth of the thin films when the substrate surface temperature is higher than the precursors' decomposition temperature [24, 56, 91, 92, 109-113]. The later deposition technique is defined as spray pyrolysis. Generally, the solution is atomized and directed to substrate surface with a carrier gas. Spray fabrication usually requires the solution with low viscosity (< 10 cP). The effects of spray parameters on film quality, as well as the use of spray pyrolysis for thin film deposition, were thoroughly examined.

For the application of optoelectronic device, patterned thin films are more favorable than amorphous films [114]. Traditionally, contact methods such as screen-printing with a specific stamp have been used to prepare the patterned thin films, which requires the external force and high viscosity solutions.

Recently, inkjet printing and aerosol jet have been attractive alternatives. These two techniques provide some advantages, involving the ability to prepare multilayer film structure without photolithography and fragile thin films without contact processing [5, 115]. Moreover, these techniques can achieve drop-on-demand delivery with maximum utilization rate of materials. Compared with screen-printing, these techniques are the type of drop-on-demand deposition technique which is cost effective and environmentally friendly. Picolitre amount of solution can also be delivered by inkjet printing and the line resolutions are less than 30 μm. However, the nozzle can be clogged by the nanoparticles contained in inks due to the requirement of picolitre resolution. The applications of inkjet printing technique have been reviewed in detail.

Aerosol jet technique has attracted great interest because of its large processing window. The high-resolution deposition can be achieved using aerodynamic focusing of aerosol-based printing [52]. This method can be used to handle a variety of viscosity and nanoparticle inks. The combination technique of slot-casting and aerosol jet printing has been used to fabricate organic light emitting diode with defined pixels.

2.5 Application in buildings

The main application of SSMs are used for preparing the spectrally selective coating for energy-efficient windows to achieve energy saving and reduction of green-house gas [6, 11, 116-122]. In this section, the performance of various SSMs applied in the glazing of windows are discussed in detail. Generally, the optical performance of SSMs is of high visible transmittance and superior near-infrared shielding rate. Simulated test has been conducted to evaluate the reduction of the indoor temperature by Liu, which can be regarded as the actual performance of spectral selectivity in real application [123].

Silver is the good candidate to prepare the spectrally selective coating by reflecting the near-infrared radiation. Physical vapor deposition (PVD) technique was utilized to fabricate the silver-based low-E coating [10, 13, 15-17]. The resultant low-E coating consisted of three-layer structure and exhibited a light blue appearance, which could effectively reflect the infrared radiation ranging from 500 nm to longer wavelength.

When compared to silver-based low-E coatings, spectrally selective metal oxide coatings are more stable when exposed in the ambient environment for building window applications. For instance, it has been presented that AZO composite film with great near-infrared reflectance was prepared by solution casting method [124-126]. In the near-infrared region, the as-prepared film demonstrated spectral selectivity with a transmittance of less than 60% at 1600 nm [16, 127]. In addition, AZO/PMMA composite coating on the ordinary glass was prepared by dip coating method. Such coating exhibited multilayer structure and strong near-infrared reflectivity. The simulated test indicated that the temperature inside the sealed box reduced by 7 ℃ for the sample with the composite coating. Likewise, another study reported that AZO nanoparticles were mixed with epoxy resin [128]. The results indicated that the AZO solid content of 0.08 wt% enhanced the near-infrared shielding property of around 10 %. Furthermore, a highly transparent AZO film was created using the radio frequency magnetron sputtering method, with a reflectance of 90% at a wavelength of 1650 nm.

Extensive research has been conducted on ITO applied in buildings [74, 83, 125, 129-131]. For example, to prepare ITO nanoparticles with a diameter of 5-10 nm, a simple synthesis method was used. After that, the near-infrared shielding coating was deposited on the surface of the ordinary glass, which could shield around 50 % near-infrared radiation and maintained the transmittance of at least 85 % in the visible region. Besides, the spectrally selective coating was fabricated by ultrasonic-assisted assembly technique. The resultant coating exhibited visible transmittance of over 80 % and near-infrared shielding rate of 75 % at 1600 nm.

Regarding the ATO nanocrystals, transparent heat-shielding coating was casted on the pretreated glass surface using waterborne polyurethane (WPU) as film former. The as-prepared coating exhibited better heat-shielding performance than ITO coating [22, 30, 32, 55, 132, 133]. Moreover, a simulated test was carried out to assess the spectral selectivity potential of the ATO coating. It is found that the indoor temperature of the ATO sample reduced about 4°C compared with the ITO sample. In addition, a study reported that the solar transmittance of the ATO coating reduced 20 % when the solid content of the ATO dispersion was 9 %. A model house test was also conducted to assess the coating's heat-shielding capabilities [22]. The results indicate that the measured temperature of ATO sample exhibited the reduction of 3.5°C compared with the glass sample without the coating.

It has been reported that the quartz glass coated by the slurry prepared by Cs_xWO_3 exhibited superior spectral selectivity in the wavelength from 800 nm to 1500 nm [63, 134-138]. The Cs_xWO_3 coating was directly prepared by painting slurry on the glass surface using an applicator. The glazing with the Cs_xWO_3 coating exhibited a temperature reduction of 9°C and 4°C respectively. Besides, $(NH_4)_xWO_3$ nanoparticles were successfully synthesized by liquid-phase method and dispersed in aqueous solution with the dispersant of polyvinylpyrrolidone (PVP). Moreover, Cs_xWO_3 nanocrystals can be combined with ZnO to prepare dual-function composite coating with superior heat-shielding property and photocatalysis. Such composite coating was fabricated by dispersing two nanofillers in ethanol solution and casted on the glass surface using an applicator. The resultant composite coating demonstrated great spectral selectivity in the wavelength from 800 nm to 1500 nm. The simulated test also indicated that the temperature corresponding to the composite coating sample reduced 3°C compared with temperature corresponding to the ITO sample. In order to achieve better optical stability, core-shell structure of Cs_xWO_3/SiO_2 nanoparticles were synthesized using TEOS as Si source. The as-prepared Cs_xWO_3/SiO_2 composite coating exhibited stable optical performance with the maximum near-infrared shielding rate of 72%, which provided a bright future for its real application in energy-efficient windows.

The techniques you mentioned usually refer to the smart windows. These techniques can dynamically and reversibly adjust the transmittance of visible light and near-infrared radiation. They can be classified as electro, thermo, photochromic windows. These techniques still suffer from the low transition efficiency and expensive cost. Thus, it still has a long road to apply them on the windows.

2.6 Summary

This section has presented the classification, synthetic methods, deposition techniques and application in buildings of SSMs. It is obvious that SSMs play a significant role on improving the optical properties of glazing materials.

Although SSMs have been proven to effectively improve the optical performance with superior near-infrared shielding rate, relatively few studies have developed a novel spectrally selective coating for existing windows. Metal oxide-based SSMs present better applicability than metal-based and metalloid-based SSMs. Currently, Low-E (low emissivity) glass is the most common type of energy-efficient glazing. Generally, the configuration of Low-E glass is of two glass panes and the Low-E coating with multilayer structure is deposited on the inner side. Low-E coating is usually fabricated by physical vapor deposition (PVD) technique such as magnetron sputtering, so the two-pane structure with air gap can prevent the Low-E coating from exposure to exterior circumstance. The cost could be relatively higher due to the complex deposition technique and the configuration of two-pane structure. Besides, the only way to retrofit single-pane glass of existing buildings by Low-E glass has to replace the whole windows, which can further increase the retrofit cost. Thus, in this research an in-situ deposition method was applied to retrofit the existing windows and the novel spectrally selective coating based on metal oxide-based SSMs were developed and comprehensively investigated in order to determine what factors influence SSMs' near-infrared shielding performance and how to improve it.

Chapter 3

Development of Sb-doped SnO_2 with low agglomerated extent by a facile dual-titration co-precipitation method

3.1 Introduction

In this chapter, a facile dual-titration co-precipitation method was developed to synthesize the Sb-doped SnO_2 nanoparticles with low agglomeration among particles. Traditional co-precipitation method is an effective way to synthesize a large amount of nanomaterials than hydrothermal method. However, there remains a challenge for the synthesis of Sb-doped SnO_2 by traditional co-precipitation method. The problem is the severe aggregation among nanoparticles after calcination, which is hard to evenly disperse the synthesized particles in the solution [35, 57, 139]. The agglomeration can also cause the decrease of transmittance in visible light region due to Rayleigh scattering. To solve this problem in the context of a practical application, a scalable dual-titration co-precipitation method is developed [34, 140-143]. ATO powders were successfully prepared with high near-infrared shielding performance, which can be applied in energy-efficient windows. Transmission electron microscopy revealed the morphology and crystalline structure (TEM).

3.2. Experiment and methodology

3.2.1 Materials

The purchased reagents without further purification were provided by Wengjiang Chemistry, Guangzhou: tin chloride pentahydrate ($SnCl_4·5H_2O$, AR), anhydrous ethanol (C_2H_5OH, AR), ammonium hydroxide solution ($NH_3·H_2O$ 25%-28%, AR), antimony chloride ($SbCl_3$, AR), and deionized water.

3.2.2 Preparation of ATO powders

3.2.2.1 Preparing compound solutions

ATO particles with a changing Sb-doped content were synthesized via the dual-titration co-precipitation method. For clarity, the antimony content was named as ATO-*x*, where *x* represented Sb / (Sb + Sn) (mol%). For a typical synthesized process, ATO-10 was prepared as an instance: 1.1 g $SbCl_3$ and 14 g of $SnCl_4·5H_2O$ were mixed in the suitable anhydrous ethanol. To investigate the optimal reaction parameters and ensure the appropriate doped amount of antimony element, ATO were synthesized with various Sb / (Sb + Sn) (mol%) of 4%, 7%, 10%, 13% and 16% respectively. The influence of various ethanol concentration (volume ratios of 0%, 25%, 50%, 75% and 100%) in the precursor solution on the crystal structure of the prepared particles was examined.

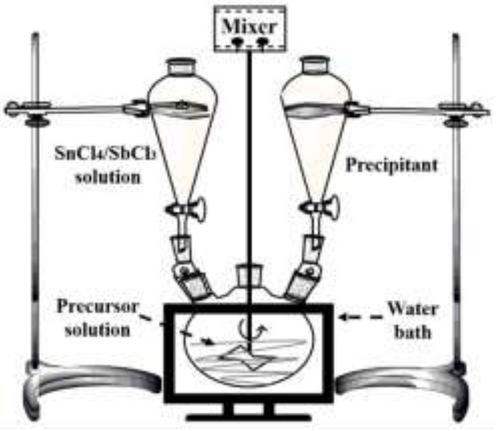

Figure 3.1 Schematic illustration of the dual-titration method in the preparation process.

3.2.2.2 Dual-titration method

In this work, two separating funnels were employed to load the Sn^{4+}/Sb^{3+} solution and $NH_3 \cdot H_2O$ precipitant respectively. The liquid in the two separatory funnels was simultaneously dropped into the flask below, while the blades of the mixer in the flask were stirred as shown in Figure 3.1. The precipitate was formed in the flask filled with precursor solution. The dual-titration process was controlled within 1 hour. After the titration process, the resultant precursor was put in a water bath device and heated at 60°C for 2 hours. The precursor continued to be centrifugated and rinsed three times with ethanol. The obtained ATO precursor was dried at 80°C for 12 hours. Then, the dried precipitate was polished into powders.

3.2.2.3 Annealing dried powders

The obtained powders were placed in crucibles and then sintered at 1000°C for 4 hours. After the calcination process, the obtained powders were collected for further characterization.

3.2.3 Characterization of ATO powders

The crystalline structure of the ATO particles were investigated on an X-ray diffraction (XRD) analysis (40kV, 30mA) equipped with graphite-monochromatized Cu Kα ($\lambda = 0.154056$ nm) and 2θ scanning angle ranging from 20° to 80°. The morphology and composition of the synthesized powders was observed by transmission electron microscopy (TEM JEM-2010F, 200kV) equipped with a Bruker Quantax 400 EDS (energy-dispersive X-ray spectrometer) system.

3.3. Results and discussion

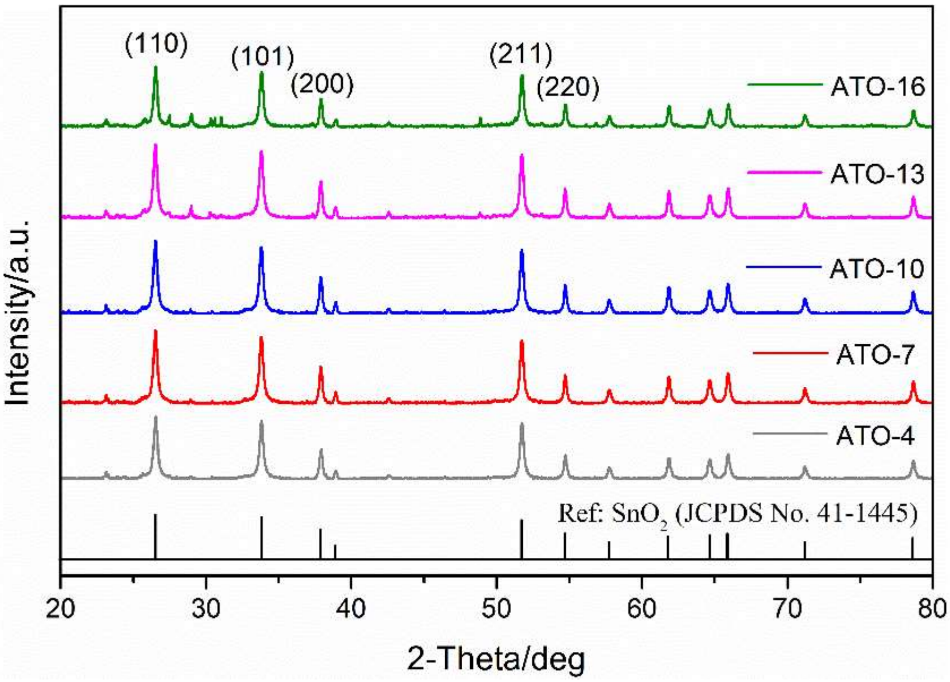

Figure 3.2 XRD patterns of ATO powders with various Sb-doped content.

Figure 3.2 illustrates the XRD patterns of synthesized ATO powders with different Sb-doped content after sintering at 1000 °C. The standard XRD pattern of Cassiterite SnO_2 (JCPDS 41-1445) was exhibited below the sample ATO-4. The XRD patterns of ATO-4, ATO-7 and ATO-10 exhibited the identical crystalline phase, implying that they were of a single-phase without any other crystalline phase. The existence of SnO_2 crystalline structure demonstrated that Sb ions replaced Sn ions in the crystal lattice of SnO_2. As for ATO-13 and ATO-16, some unknown characteristic peaks were observed between two peaks which corresponded to lattice planes (110) and (101), implying that other crystalline phases appeared. After Sb doping, the positions of diffraction peaks should shift to higher angles. Such higher shift is ascribed to the lattice distortion with the incorporation of Sb. Since the diameter of Sb^{5+} ions are slightly smaller than that of Sn^{4+} ions, the replacement of Sn^{4+} with Sb^{5+} causes the shrinkage in crystal cell size [33, 143]. The increase of smaller Sb dopant decreases the lattice constant of Sb-doped SnO_2, causing to higher diffraction angles.

Moreover, the crystallite size was roughly calculated via the Scherrer formula [28] shown in equation (3.1).

$$D = \frac{K\gamma}{\mathrm{B}\cos\theta} \tag{3.1}$$

Here, D represents the calculated crystallite size; K indicates the Scherrer constant 0.89; B denotes the full wave at half maximum also known as FWHM; γ refers to the wavelength of X-ray (0.154056nm) and θ is the half of the scanning angle. The average crystallite size was calculated based on FWHM of the strong characteristic peaks shown in Figure 3 and results are shown in Table 1.

Table 3.1 The calculated crystallite size using the Scherrer formula.

Sample	ATO-4	ATO-7	ATO-10	ATO-13	ATO-16
D/nm	43.2	43.5	27.8	42.6	42.1

In Table 3.1, the crystallite size changes from 27.8 to 43.5 nm. It can be attributed to the tangible that Sn^{4+} ions are larger than Sb^{5+} ions (radius of Sb^{5+}: 0.60 Å, radius of Sn^{4+}: 0.69 Å). Therefore, the Sb^{5+} ions can easily enter the lattice to substitute Sn^{4+} ions. Additionally, with increasing Sb-doped content, the grain sizes of (110), (101) and (211) crystal planes calculated by Scherrer's formula illustrate an increasing trend that subsequently decreases. This could be because Sb^{3+} ions (radius of Sb^{3+}: 0.76 Å) constituted a higher ratio of the total Sb ions at a low doping amount of Sb. After reaching a critical Sb doping concentration, the Sb^{5+} ions constituted a higher proportion of the total Sb ions, which reduced the lattice space. With a further increase in the doping amount of Sb, the Sb^{3+} ions once again dominated the ratio of Sb ions. Among the five samples, it can be inferred that ATO-10 contained a relatively high level of Sb^{5+} ions, which implied more free charge carriers. The crystallite size changes are actually decided by the Sb-doped concentration. The lattice parameters shrinkage is caused by the presence of large amounts of Sb^{5+} ions, whose diameter is smaller than that of Sn^{4+} and Sb^{3+} ions. The near-infrared shielding effect is induced by the localized surface plasmon resonance [51]. The increase in free carrier concentration can cause a blue shift absorbing more solar energy. Hence, the high concentration of Sb^{5+} is the fundamental reason for affecting the solar heat insulation performance.

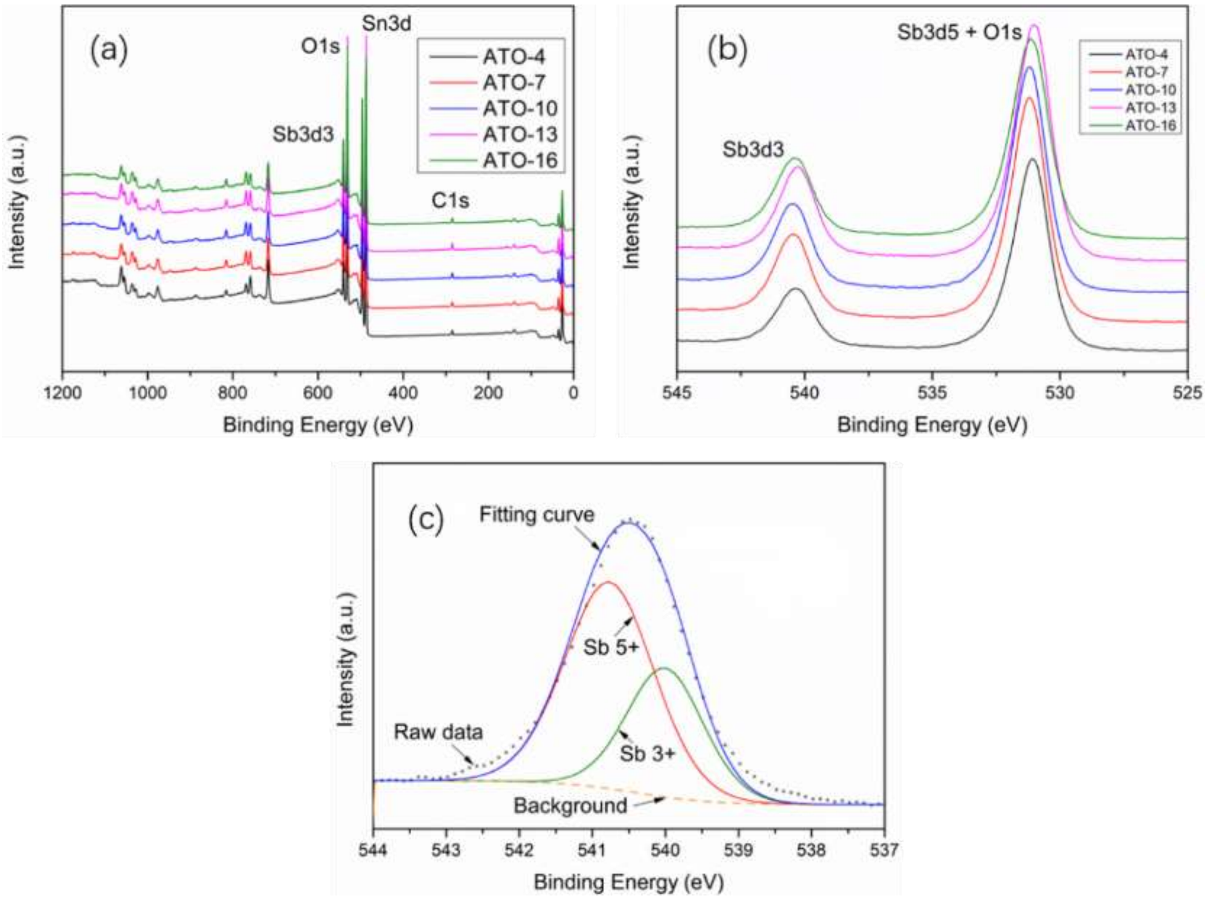

Figure 3.3 XPS spectra of ATO nanoparticles with different Sb doped content. (a) survey spectra, (b) high resolution spectra of Sb 3d, (c) XPS spectrum and fitting curves of Sb $3d_{3/2}$ for ATO-10 nanoparticles.

XPS analysis was performed on ATO nanoparticles with different Sb-doped content, as shown in Figure 3.3. The presence of Sn, Sb, and O elements in the ATO nanoparticles is clearly indicated by the survey XPS spectra (Figure 3.3a). Sn $3d_{5/2}$ and Sn $3d_{3/2}$ binding energies for ATO are 487 and 496 eV, respectively, and are generally attributed to the presence of Sn^{4+}. The high-resolution XPS spectra of Sb 3d are shown in Figure 3.3b.The binding energy of the Sb 3d is reported to be in the range of 525−545 eV. Antimony can be doped in two oxidation valence, Sb^{5+} and Sb^{3+}.The fitting curves (Figure 3.3c) illustrate that a high Sb^{5+}/Sb^{3+} ratio is in ATO-10, which is consistent with above discussion for crystalline structure.

To study the influence of the precursor solution on crystalline phase, the ATO-10 powders were prepared by a mixed solution with various ethanol concentration.

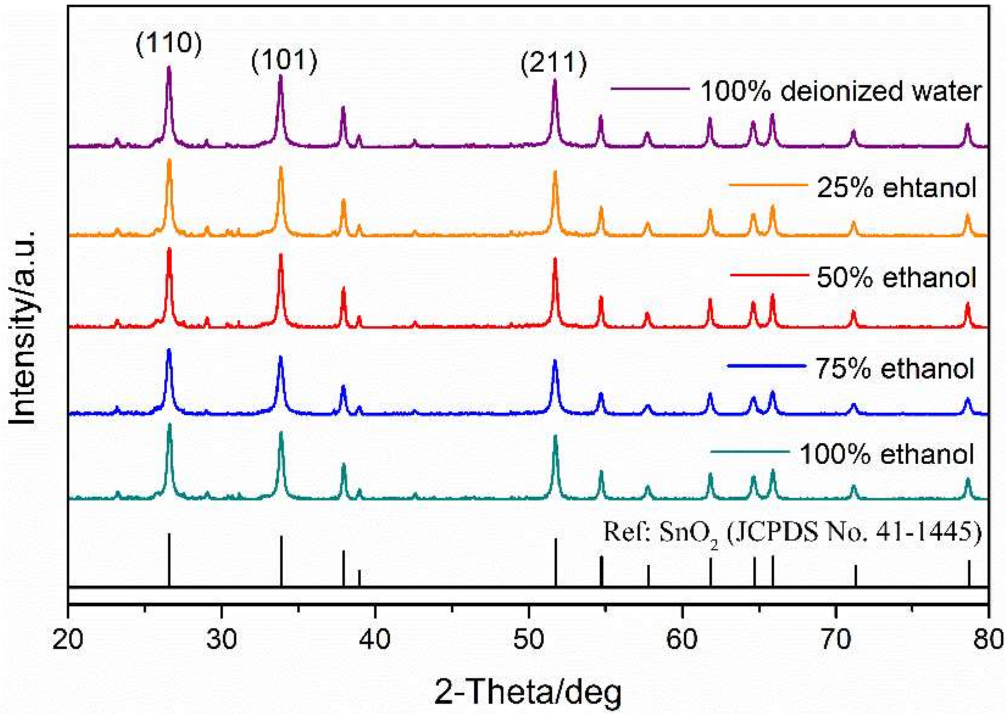

Figure 3.4 XRD patterns of ATO-10 powders synthesized by precursor solution composed by ethanol and deionized water with various volume ratios.

As shown in Figure 3.4, all the prepared samples illustrated the lattice planes of (110), (101) and (211), indicating the samples formed the same tetragonal rutile structure. With an increase in ethanol content, the XRD pattens of the synthesized samples showed the same crystalline structure as that of the standard reference sample, implying that water or ethanol can facilitate the formation of the SnO_2 crystalline structure without any distinction. Moreover, the utilization of ethanol can weaken the aggregation extent during the drying process, which can be attributed to the formed ethoxide groups surrounding the surface of the particles. Furthermore, the ATO powders prepared by a precursor solution composed of ethanol can lead to a lower level of aggregations than other samples owing to its lower solvent polarity.

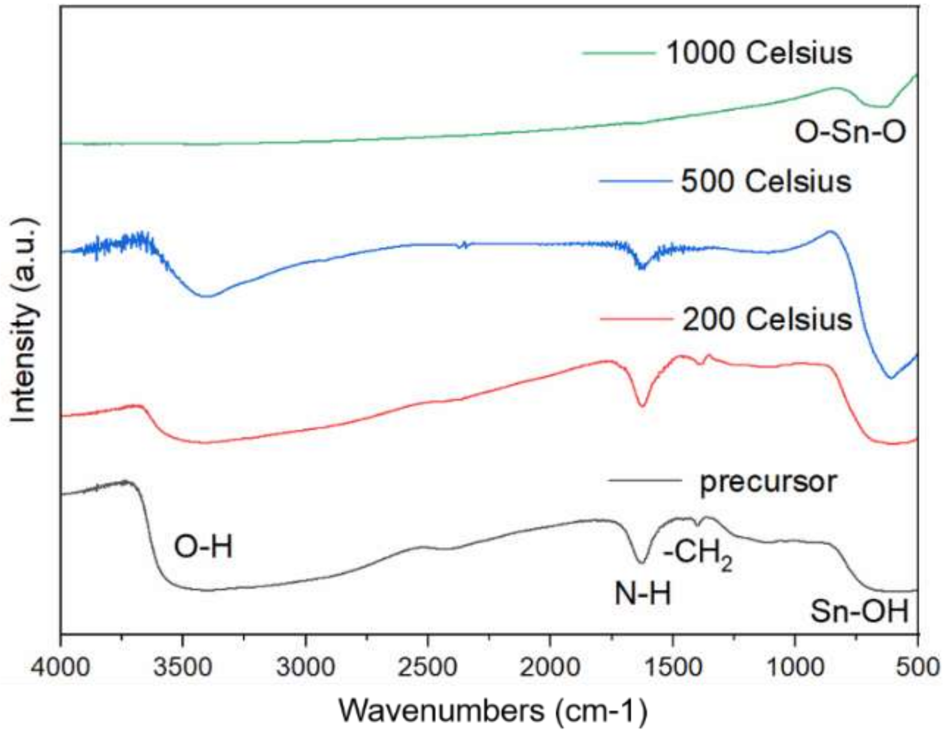

Figure 3.5 FT-IR spectra of the dried precursor and precursors calcined at 200°C, 500°C and 1000°C.

In order to investigate the reaction process at high temperature, FT-IR spectra of precursor precipitate and the precipitate respectively calcined at 200°C, 500°C and 1000°C were obtained. As shown in Figure 3.5, FT-IR spectra shows that the peak at 1400.38cm^{-1}, corresponding to the $-CH_2$ vibration, turned into weak. The N-H stretching bands and the O-H stretching vibration gradually decreased with the increase of calcined temperature, which may be attributed to the evaporation of ethanol, water and NH_3. For the sample calcined at 1000°C, it can be seen that the N-H, $-CH_2$ and O-H vibration completely vanished, indicating the decomposition of organics. The presence of O-Sn-O illustrates the tin hydroxide has transformed to the tin oxide crystalline structure.

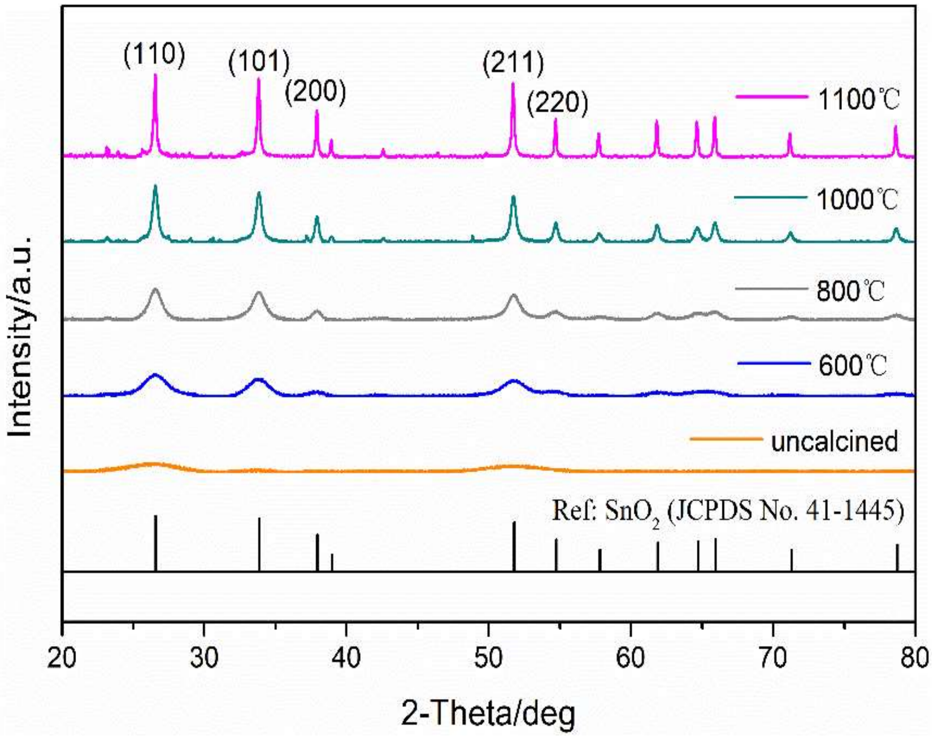

Figure 3.6 XRD patterns of ATO-10 annealed at 600°C, 800°C, 1000°C and 1100°C.

As shown in Figure 3.6, ATO-10 precursors were sintered at 600°C, 800°C,1000°C and 1100°C for 4 hours respectively. It can be seen that the XRD pattern of uncalcined ATO-10 maintained amorphous state. After calcination at 600°C, the characteristic peaks corresponding to crystalline planes (110), (101), (200), (211) and (220) appeared and no other phase was observed, implying that the crystalline structure began to form at 600°C. The crystallite size of samples calcined at 800°C and 1000°C calculated by Scherrer's formula were smaller than that of the sample calcined at 1100℃, because the high calcination temperature would cause severe aggregation. In addition, the characteristic peak intensity of the (110) crystalline plane of each calcined sample was higher than that of (101), which was also reported in a previous study [113].

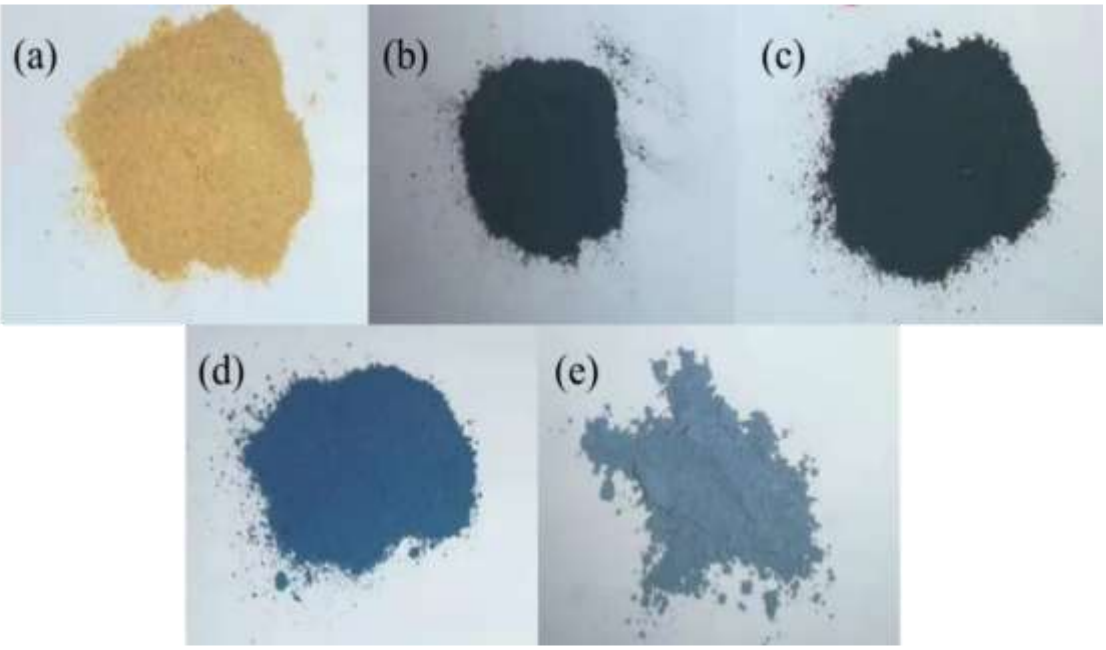

Figure 3.7 The images of ATO-10 precursors (a) before annealing, calcined at (b) 600℃, (c) 800℃, (d) 1000℃, and (d) 1100℃.

Figure 3.7 shows the images of ATO-10 precursors before and after annealing at various temperature. It can be seen that the powders color before calcination appeared grayish yellow. With the increase in the calcination temperature, the color of the synthesized powders changed from dark gray to blue. This transition can be ascribed to the increase in Sb^{5+} ions in the crystalline lattice with the increase in annealing temperature. As the concentration of Sb^{5+} ions increased, more free electrons were generated and entered the conductive band, which allowed the samples to absorb the visible light of the corresponding wavelength and appear blue. However, when the calcination temperature was 1100℃, the color of the powder was lighter than the sample calcined at 1000°C, owing to the decreased concentration of Sb^{5+} ions.

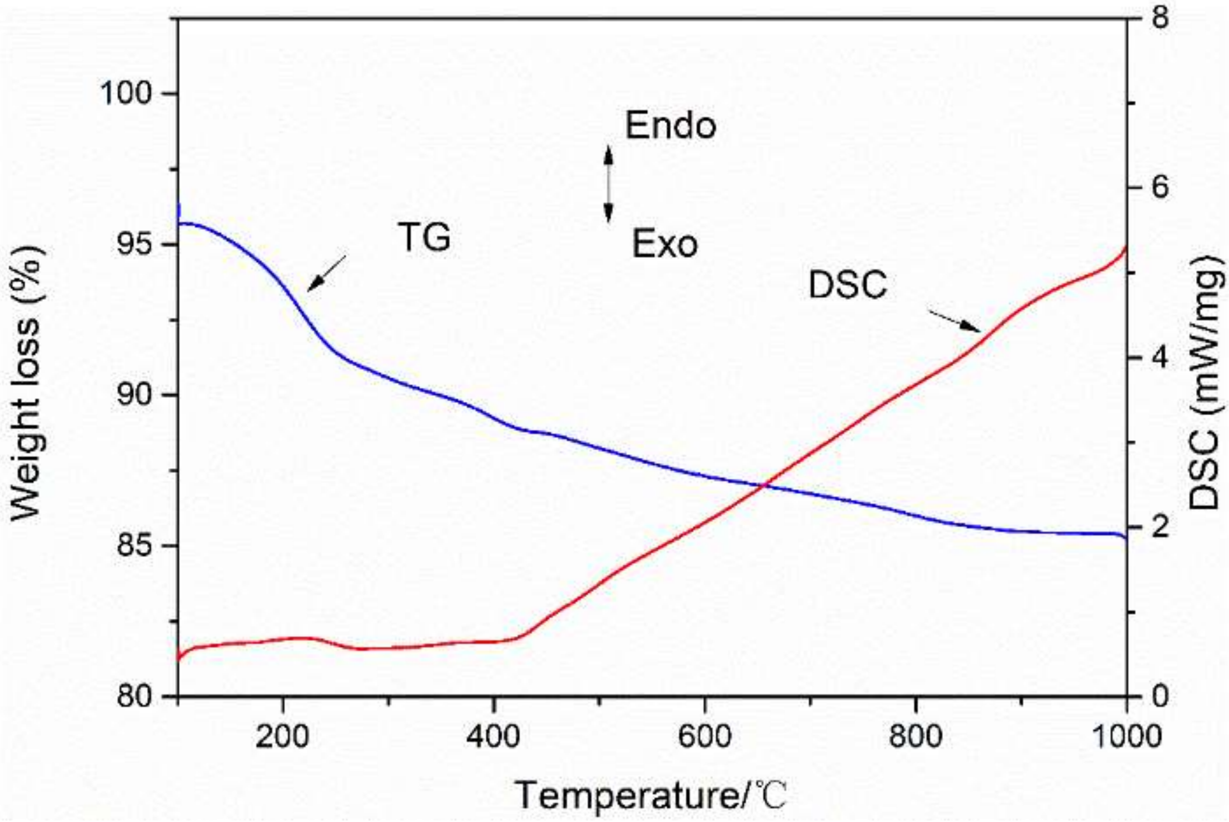

Figure 3.8. TG/DSC curves of ATO-10 precursor powders

The phase transformation of ATO-10 precursor was obtained by TG/DSC analysis. As shown in Figure 3.8, the precursor precipitate loses weight as the temperature rises from 100°C to 800°C. Then, the weight loss became slow after 800°C. During the whole TG process, the highest loss speed was around 200°C, which might be attributed to the evaporation of the crystal water. The DSC curve shows a gradual endothermic trend throughout the whole test processing. Unlike sharp peaks in other research works, the precursor prepared by co-precipitation method could be transformed into ATO nanocrystals by the condensation of hydroxide groups [57]. This reaction is an endothermic process, which is in accordance with the DSC results.

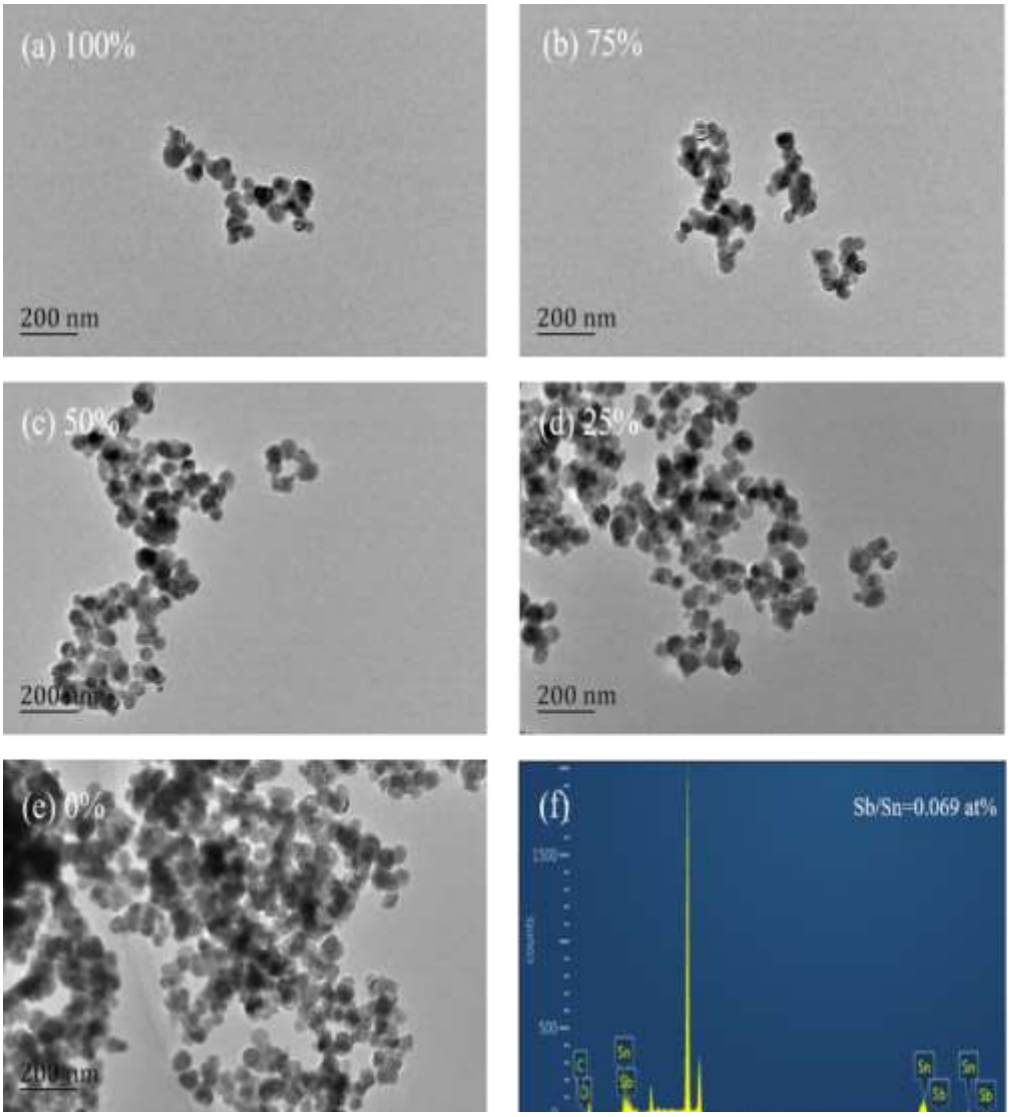

Figure 3.9 TEM images of the ATO-7 powders synthesized in precursor solution with ethanol content of (a) 100%, (b) 75%, (c) 50%, (d) 25% and (e) 0% after calcined at 1000℃; (f) EDS pattern of ATO-7 powders synthesized in precursor solution with 100% ethanol content after calcined at 1000℃.

The morphology and EDS pattern of as-synthesized ATO-7 powders using the precursor solutions composed of ethanol and deionized water with various volume ratios were investigated by TEM (Figure 3.9). It is noteworthy that the ATO-7 nanoparticles were of spherical nanoparticles with different degrees of aggregation, and the aggregated degree increased with the reduction in ethanol content. When 100% ethanol was employed, the degree of aggregation was slight as shown in Figure 3.9a. This demonstrated that a higher concentration of ethanol was conducive to the preparation of ATO-7 nanoparticles with low aggregation extent, and vice versa. As shown in Figure 3.9f, the element composition shown in the EDS pattern exhibited the presence of O, Sn and Sb in ATO-7 and the atomic ratio of Sb/Sn was 0.069.

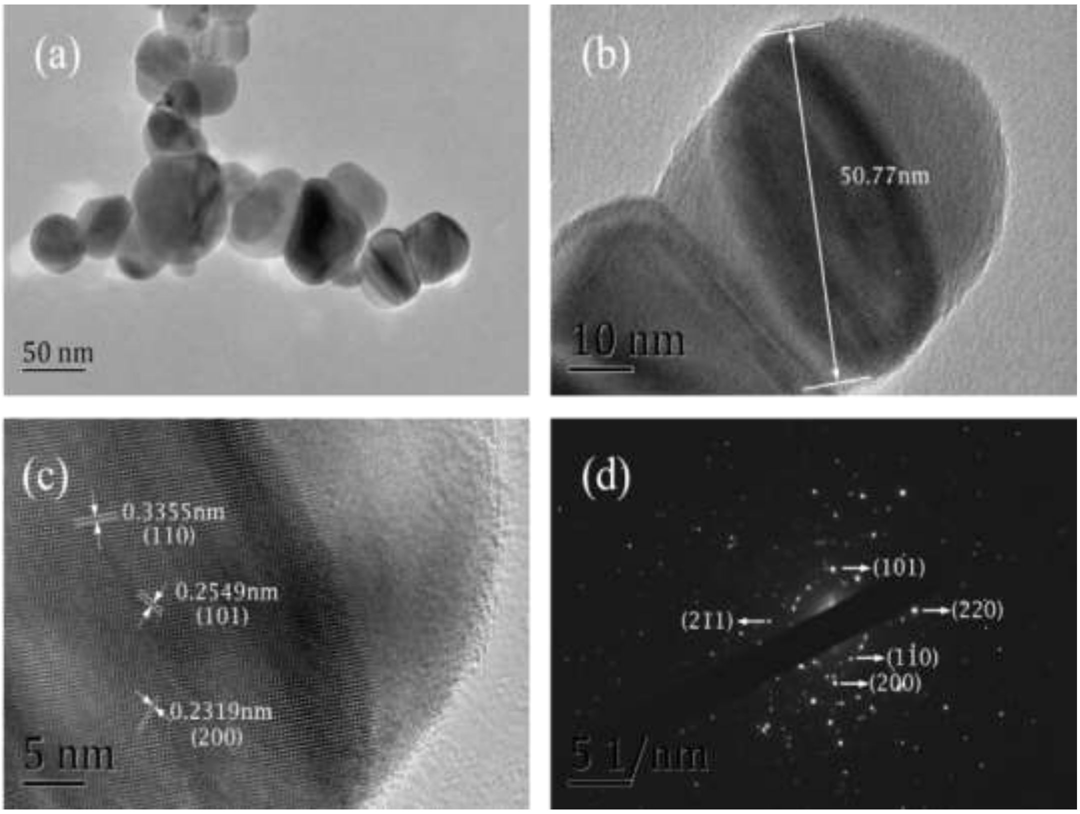

Figure 3.10. (a) TEM image, (b) and (c) HRTEM images of ATO-7 powders after annealing at 1000℃, (d) SAED profile.

To further study the morphology and crystalline structure of ATO-7 nanoparticles, HRTEM was employed to characterize the prepared samples. HRTEM images and SAED patterns of ATO-7 powders synthesized by an ethanol precursor without deionized water were shown in Figure 3.10a and b, indicating that ATO-7 powders were nanocrystals with primary particle sizes ranging from 45 to 55nm. In Figure 3.10 c, the lattice fringes of ATO-7 illustrated that the preferential growth directions were [110], [101] and [200]. The spacing calculated by the FFT function between adjacent lattices were 0.33455nm, 0.2549nm and 0.2319nm corresponding to (110), (101), (200), (211) and (220) planes separately.

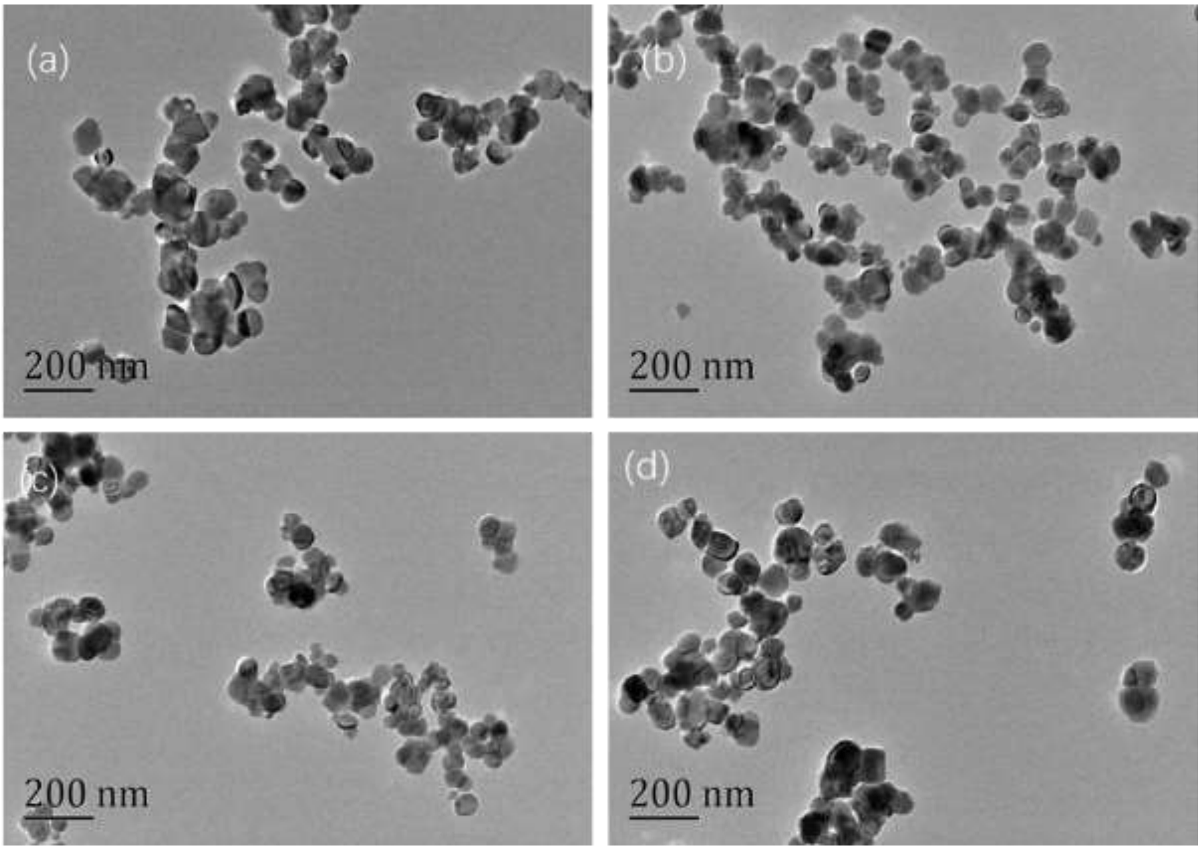

Figure 3.11 TEM images corresponding to (a) ATO-4, (b) ATO-7, (c) ATO-10 and (d) ATO-16.

The size distribution and mean crystalline size were conducted by counting enough nanoparticles in the TEM images (Figure 3.11) and using the Gaussian fitting function. The ATO nanoparticles with four different doped concentration were selected as the testing objects, the samples including ATO-4, ATO-7, ATO-10 and ATO-13.

As shown in Figure 3.12, the size distribution and mean size were obtained by counting 40 particles in TEM images. The ATO-10 demonstrates a smaller particle diameter than other samples.

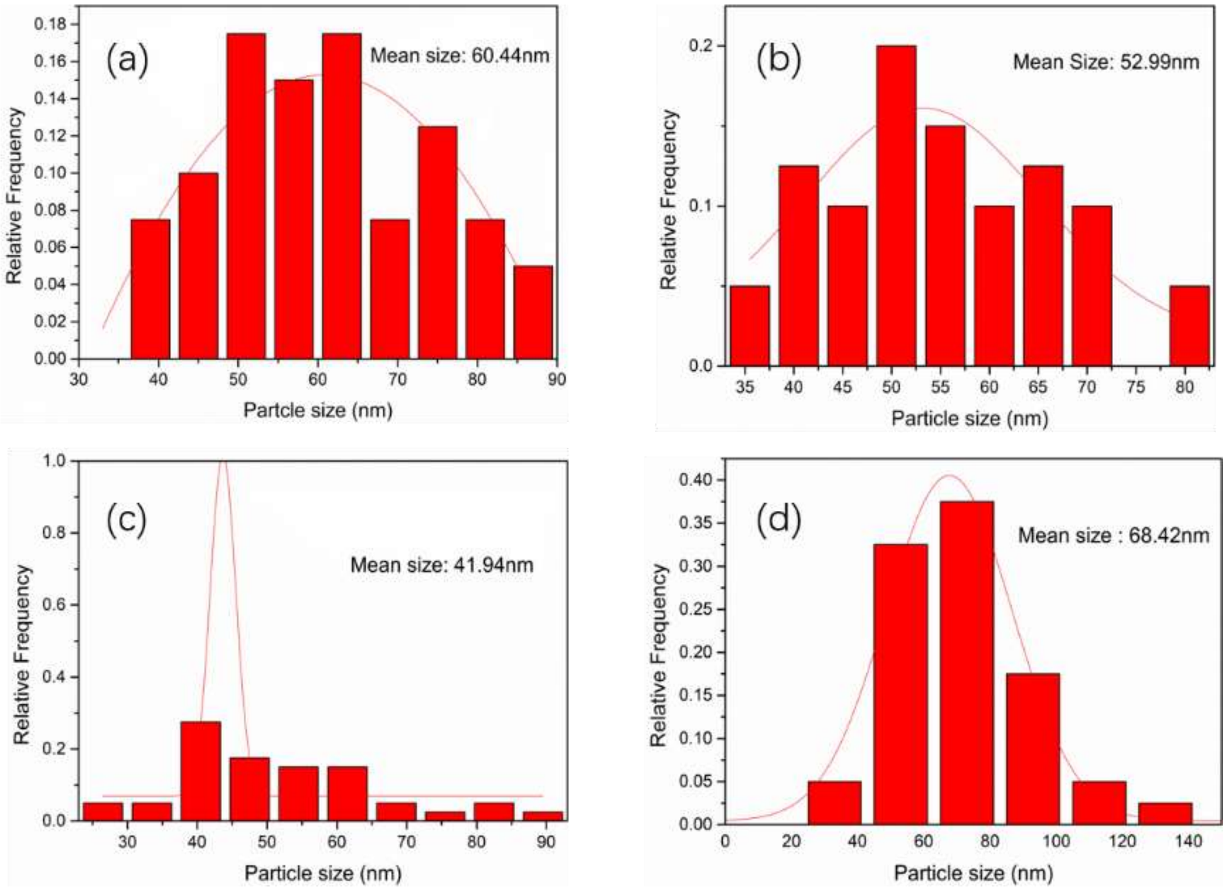

Figure 3.12. Size distribution of the ATO nanoparticles with different dopant concentration, (a) ATO-4, (b) ATO-7, (c) ATO-10 and (d) ATO-13.

3.4 Conclusions

ATO powders with low agglomeration have been synthesized using a novel dual-titration co-precipitation method. It has been proved that the dual-titration way is conducive to inhibit the agglomeration of primary particles. The optimal experimental reaction conditions to synthesize ATO nanoparticles with near-infrared shielding performance show that the molar ratio is 10%, The content of ethanol in precursor solution of 100%, and the annealing temperature is 1000℃. Besides, ATO primary nanoparticles were gained ranging from 45 to 55nm with a low aggregated degree.

Chapter 4

Investigation of pH value on doping level and optical performance of antimony-doped tin oxide nanocrystals as nanofillers of spectrally selective coating

4.1 Introduction

In this chapter, ATO nanocrystals were prepared by the dual-titration co-precipitation method using $NH_3 \cdot H_2O$ as the precipitant. The effects of pH value of the reaction system on the antimony doping level and the optical performance of ATO nanocrystals were investigated by means of X-ray diffraction (XRD), X-ray photoelectron spectroscopy (XPS), inductively coupled plasma-optical emission spectroscopy (ICP-OES), transmission electron microscopy (TEM).

4. 2 Experimental section

4.2.1 Materials

Tin chloride pentahydrate ($SnCl_4 \cdot 5H_2O$), antimony chloride ($SbCl_3$), ammonium hydroxide solution ($NH_3 \cdot H_2O$ 25%–28%), absolute ethanol, absolute ethanol (C_2H_5OH) and deionized water (H_2O).

4.2.2 Synthesis of ATO nanocrystals

The ATO nanocrystals were prepared by co-precipitation method using $SnCl_4 \cdot 5H_2O$ as Sn source and $SbCl_3$ as Sb source respectively. First, a certain amount of $SnCl_4 \cdot 5H_2O$ was added into the deionized water, then $SbCl_3$ was introduced into the aqueous solution of $SnCl_4 \cdot 5H_2O$ with a Sb/(Sb + Sn) molar ratio of 10%. Diluted $NH_3 \cdot H_2O$, the precipitant, was dropped into the precursor solution at a constant speed to form the hydroxide precipitation. During this process, the titration endpoint of pH value reached 4, 5, 6, 7, 8 corresponding to the ATO sample S1, S2, S3, S4, S5 respectively. The resultant solution was kept at 60 °C for 1 hour and then centrifugated three times with absolute ethanol. The obtained precipitation was dried at 80 °C for 2 hours and then polished into powders. The as-prepared powders were subsequently placed a tube furnace and sintered at 1000 °C for 4 hours to get the desired samples.

4.2.3 Characterization

The phase compositions of nanoparticles were examined by X-ray diffraction (XRD) with Cu Kα radiation. The morphologies and microstructures of the nanoparticles were obtained by transmission electron microscopy (TEM) with an energy dispersive spectrum (EDS) attachment. The binding energies of Sb 3d were obtained by X-ray photoelectron spectroscopy (XPS). The thermal behavior of the sample was determined by thermal gravimetric analyzer within a temperature range of 25 °C - 1000 °C with a heating rate of 10 °C per minute. Inductively Coupled Plasma-Optical Emission Spectroscopy (ICP-OES) was conducted on the iCAP 6500 Thermo spectrometer.

4.3 Results and discussion

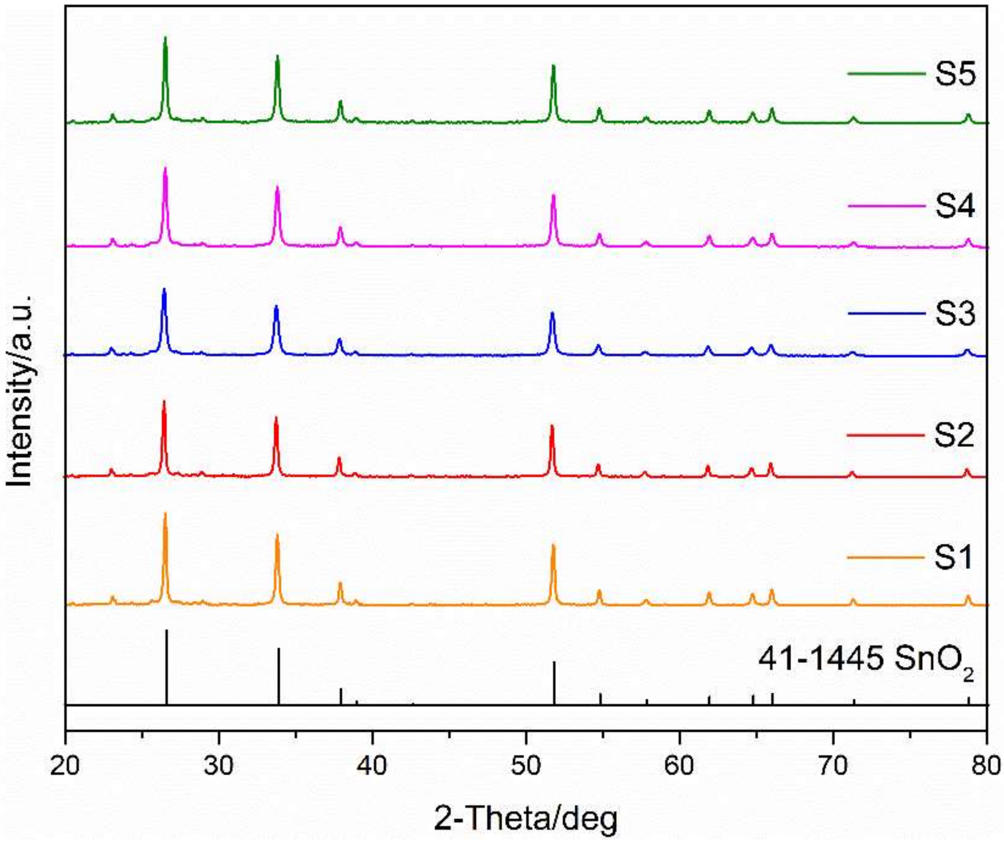

Figure 4.1 XRD patterns of the powders prepared by different pH value in the precursor solution.

To confirm the phase composition, XRD measurements were conducted to the nanocrystals prepared in the precursor solution different pH value. The XRD patterns of the as-synthesized nanocrystals with the pH value of 4, 5, 6, 7, 8 in the precursor solution corresponding to the sample S1, S2, S3, S4, S5 respectively are shown in Figure 4.1. It can be observed that all the patterns agreed well with the standard pattern of cassiterite SnO_2 (JCPDS 41-1445) without the presence of other phases (such as Sb_2O_3, Sb_2O_5), indicating that antimony has been totally doped into the crystal structure of the nanocrystals. Besides, the diffraction peaks of all the patterns were narrow and sharp, implying that all the nanocrystals were of good crystallinity. The average crystallite size calculated by Scherrer formula [144] ($D = 0.89\lambda/[B \cos \theta]$, where D, λ, B, θ was the crystallite size, the wavelength of X-ray, the full width at half maximum of (110), the half of the scanning angle respectively) was about 36.1, 37.8, 25.9, 28.7 and 31.9 nm for S1, S2, S3, S4 and S5, respectively.

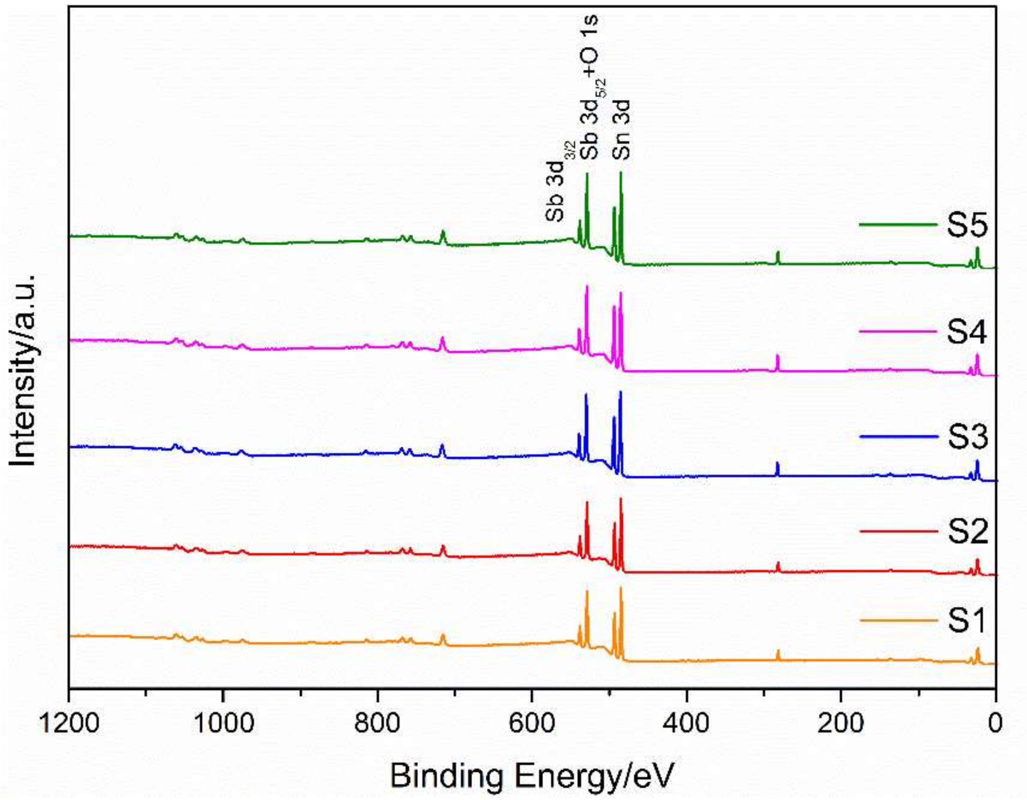

Figure 4.2 Survey spectra of the powders with different pH value in the precursor solution

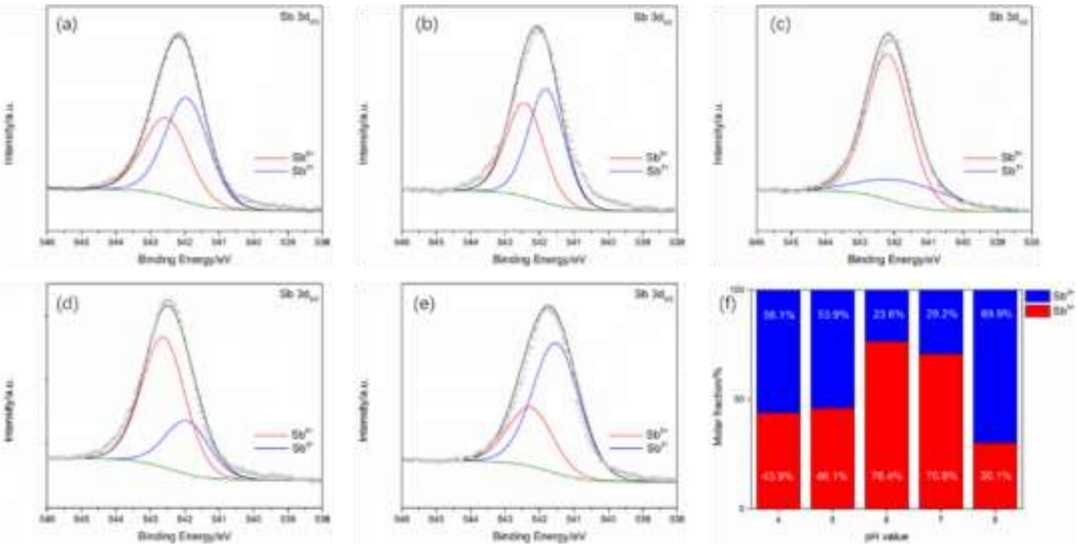

Figure 4.3 (a)-(e) Sb $3d_{3/2}$ core-level spectra of ATO nanocrystals synthesized with different pH value in the precursor solution; (f) The valence distribution of Sb in ATO nanocrystals with different pH value in the precursor solution.

Figure. 4.2 shows the survey spectra of as-prepared powders with different pH level in the synthetic process. It can be seen that the elements of Sn, Sb, and O existed in the nanocrystals, implying that Sb element has been successfully doped into the crystal structure. Figure 4.3a-e display the core-level XPS spectra of Sb $3d_{3/2}$ within the scope of 538-546 eV. It was reported that two valence state of Sb ions coexisted in the ATO nanocrystals. The Sb $3d_{3/2}$ curves shown were fitted into two peaks at 541.7 and 542.6 eV corresponding to Sb^{3+} and Sb^{5+} respectively [141, 143]. The optical properties of the as-synthesized ATO nanocrystals were significantly affected by its electrical capabilities [141]. Sb^{5+} ions serve as electron donors, forming a light donor level near the conduction band of tin oxide, but Sb^{3+} ions act as the electron acceptors. When the two valence states of Sb ions coexist, the compensating effect is inevitable. The n-doping dominated by Sb^{5+} ions contributes to a higher concentration of free electrons, which can lead to stronger localized surface plasmon resonance (LSPR) [145]. Thus, a high ratio of Sb^{5+} ions is conducive to improve the near-infrared shielding performance of the nanocrystals. The content of Sb^{5+} ions was highest when the pH value in the precursor solution was 6, accounting for 76.4 % of the total amount of Sb atoms, according to the valance distribution of Sb shown in Figure 4.3f.. When the pH value reached 7, the content of Sb^{5+} ions decreased to 70.8%. With the increase of pH value in the synthetic process, the ratio of Sb^{5+} ions showed an increasing trend and reached the maximum content when the pH value was 6. After that, the ratio of Sb^{5+} ions decreased to 30.1% when the pH value in the precursor solution was 8. The results indicate that pH value of 6 in the precursor solution contributes the most Sb^{5+} ions in ATO nanocrystals, which plays a significant impact on the optical performance.

Table 4.1 The Sb content in ATO nanocrystals measured by ICP-OES and the molar fraction of Sb^{5+} in the two valence states

pH value	Sb content (mol %)	Sb^{5+}content (mol %)
4	22.8	43.9
5	13.8	46.1
6	11.6	76.4
7	12.9	70.8
8	13.5	30.1

To further investigate the effect of pH value on the doping level, the Sb content $(\mathrm{Sb}\ /[\mathrm{Sb}+\mathrm{Sn}]\mathrm{mol}\ \%)$ of the samples was measured by ICP-OES and the ICP-OES measurement provided the Sb content in the whole s ample. The initial doping ratio of the Sb content was 10%. As shown in Table 4.1, the Sb content displayed a decreasing trend with the increase of the pH value. When the pH value reached 6, the Sb content attained minimum value of 11.6%, which was close to the initial doping value of 10%. In the meanwhile, the content of Sb^{5+} ions also reached the maximum value of 76.4%. Continuing to increase the pH value, the Sb content presented an increasing trend and reached 13.5 when the pH value was 8. A plausible explanation for the above results is the changing formation of the tin hydroxide. Tin hydroxide is a kind of amphoteric hydroxide which can react with alkaline substance to form salt and water. During the titration process, Sn^{4+} ions started to form the tin hydroxide. When the pH value attained 6, it can be inferred that nearly all Sn^{4+} ions formed the tin hydroxide. With the increase of $NH_3 \cdot H_2O$ in the precursor solution, the mass of tin hydroxide began to reduce, but the Sb content stated to increase.

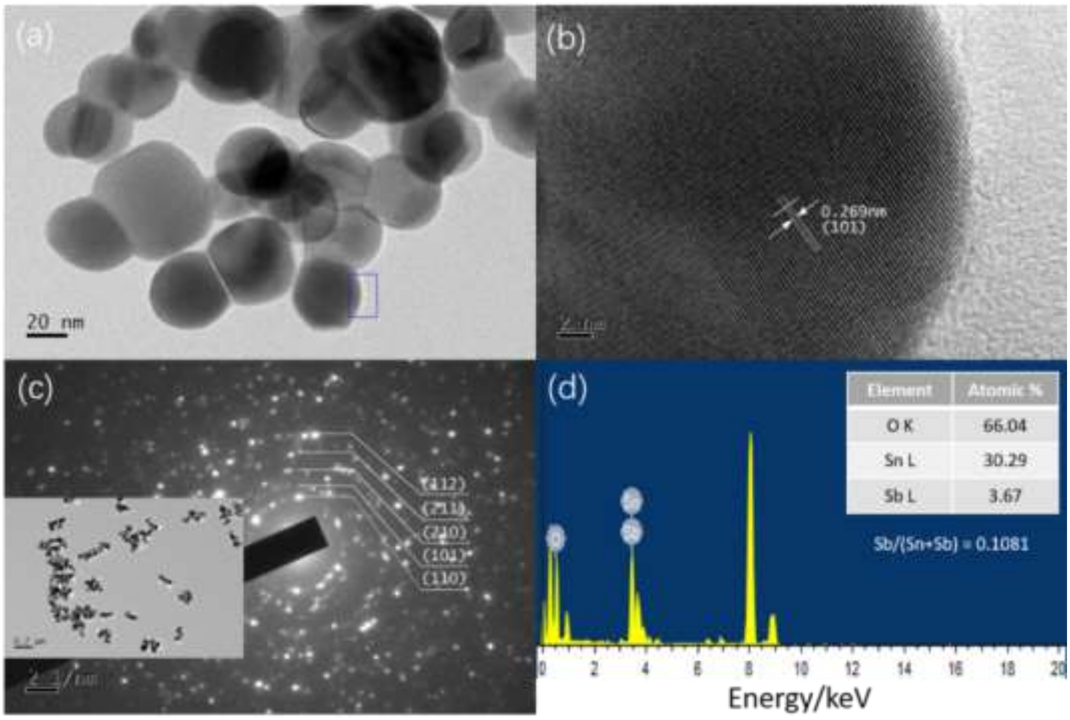

Element	Atomic %
O K	66.04
Sn L	30.29
Sb L	3.67

Figure 4.4(a) TEM image of ATO nanocrystals with the pH value of 6, (b) HR-TEM image of the selected area, (c) SAED pattern of the inset area and (d) EDS pattern of the sample with the pH value of 6.

The detailed structural information was determined using transmission electron microscopy (TEM). Figure 4.4 presents the TEM image, HR-TEM image, SAED pattern and EDS pattern of the as-synthesized ATO nanocrystals with the pH value of 6 in the titration process. In Figure 4.4a, most of the as-prepared nanoparticles show a circular shape. Figure 4.4b is the HR-TEM image of the selected area in Figure 4.4a and the lattice spacing is 0.269 nm, which is determined as plane of (101). The as-synthesized sample was further confirmed by the SAED pattern displayed in Figure 4.4c. The element composition is shown in Figure 4.4d, indicating the existence of Sn, Sb and O element. Besides, the measured Sb content is about 0.1081 which is quite close to the initial doping value of 10%, indicating that almost all Sb ions have been doped into the crystal structure of SnO_2.

4.4 Conclusions

The effect of the pH titration endpoint on the doping level for ATO nanocrystals was systematically studied. The phase composition, element composition, valence state of Sb ions, microstructure and thermal characteristics of ATO nanocrystals were comprehensively investigated. The results demonstrate that the doping level of ATO nanocrystals certainly relied on the pH value of the titration endpoint. When the titration endpoint's pH value was 6, the measured doping ratio of Sb was 10.81% which is close to the initial Sb doping level of 10%. In addition, the pH value of titration endpoint also plays an important impact on the content of Sb^{5+} ions. The content of Sb^{5+} ions also reached the maximum value of 76.4% when the pH value was 6.

Chapter 5

Development of one-pot synthesis of hexagonal Cs_xWO_3 nanocrystals with superior near-infrared shielding property for energy-efficient glazing

5.1 Introduction

In this chapter, controllable one-pot synthesis of Cs-HTBs without post heat-treatment was developed using ammonium metatungstate hydrate (AMT) as the W source and cesium carbonate (Cs_2CO_3) as Cs source. For the synthesis of Cs-HTBs, the reducing mechanisms of tartaric acid and tartaric acid with the help of chloroplatinic acid were investigated. The relationships between the different reducing agents used in the synthetic process and the crystalline composition of the as-prepared nanocrystals were discussed and the possible synthetic mechanism was subsequently proposed. This synthetic strategy has significant implications for lowering production costs and promoting the use of Cs-HTBs in energy-efficient glazing. In the previous studies, WCl_6 and CsOH were used as the raw materials to synthesize Cs_xWO_3. However, WCl_6 is easy to be oxidized and hydrolyzed. Cesium hydroxide is highly corrosive and prone to deliquesce. Therefore, its difficult storage features limit its industrial application. By contrast, ammonium metatungstate (AMT) and cesium carbonate used in this work are of high chemical stability, which are convenient to be stored in the factory. One-pot method was utilized to conduct the solvothermal reaction during the synthesis of Cs_xWO_3. The autoclave can be opened until it has been cooled to room temperature. In addition to Cs_xWO_3, there will be a small amount of by-products (Glyoxal). Although glyoxal has a low toxicity, people can avoid contact with it by wearing the protective mask and clothing. Besides, glyoxal is an important industrial raw material, which is used to crosslink a wide range of other polymers. Thus, the resultant by-products can be further collected by using some devices.

5.2 Experimental section

5.2.1 Materials

Ammonium metatungstate hydrate (AMT, $(NH_4)_6H_2W_{12}O_{40} \cdot aH_2O$), cesium carbonate ($Cs_2CO_3$), tartaric acid ($C_4H_6O_6$), chloroplatinic acid ($H_2PtCl_6$), deionized water ($H_2O$), anhydrous ethanol ($C_2H_5OH$), polyethylene glycol 200 (PEG 200) were purchased from Macklin. All the chemical reagents are of analytical grade and used without further treatment.

5.2.2 Synthesis of Cs_xWO_3 nanocrystals

The Cs_xWO_3 nanocrystals were made using a solvothermal method with AMT as the W source and Cs_2CO_3 as the Cs source. After adding a certain amount of AMT to the solvent, Cs_2CO_3 with a Cs/W molar ratio of 0.33 was added to the AMT solution. The mixed solution had a total volume of 30 ml. The as-prepared solution was then placed in a PTFE autoclave with a 50 mL interval volume, and the solvothermal reaction was carried out in a drying oven at 240 °C for 24 hours. The blue products were centrifuged and washed three times in ethanol before being vacuum dried at 60°C. The Cs_xWO_3 nanocrystals synthesized by absolute ethanol were named as CWO-1. The Cs_xWO_3 nanocrystals synthesized by anhydrous ethanol with tartaric acid of 1 mol/L in the precursor solution were named as CWO-2. The Cs_xWO_3 nanocrystals prepared by ethanol with tartaric acid of 1 mol/L and a certain amount of chloroplatinic acid were labelled as CWO-3. Corresponding products doped without Cs_2CO_3 in the precursors were obtained and labelled as WO-1, WO-2 and WO-3.

5.2.3 Characterization

The phase compositions of nanoparticles were examined by X-ray diffraction (XRD) with Cu Kα radiation. The morphologies and microstructures of the nanoparticles were obtained by transmission electron microscopy (TEM) with an energy dispersive spectrum (EDS) attachment. The chemical composition and binding energies of W 4f were obtained by X-ray photoelectron spectroscopy (XPS).

5.3. Results and discussion

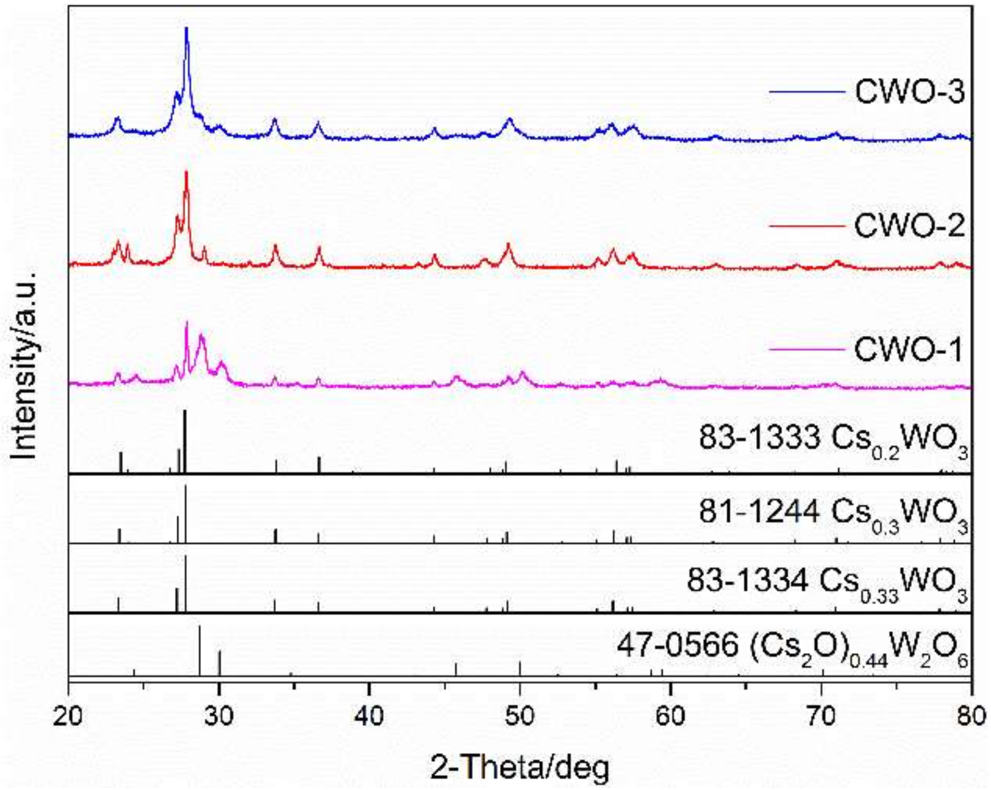

Figure 5.1 XRD patterns of as-synthesized CWO-1, CWO-2 and CWO-3.

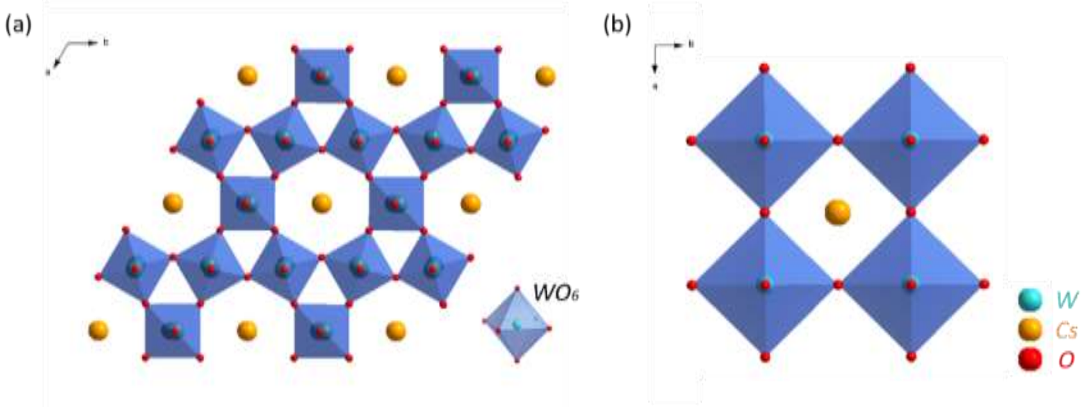

Figure 5.2 Structural framework of (a) Cs-HTBs and (b) Cs-CTBs projected on *a-b* planes.

Figure 5.1 presents the XRD patterns of the as-prepared Cs_xWO_3 (CWO-1, CWO-2 and CWO-3) nanocrystals with different reducing agents and a mixed (hexagonal and cubic) phase appears in CWO-1 and CWO-2. Figure 5.2 shows the structural frameworks of cesium doped hexagonal tungsten bronze nanocrystals (Cs-HTBs) and cesium doped cubic tungsten bronze nanocrystals (Cs-CTBs). Cs-HTBs shown in Figure 5.2a consist of corner-sharing WO_6 octahedral arrays with Cs^+ ions located in the hexagonal channels of the crystal framework. The upper limit of Cs/W molar ratio is 0.33 in hexagonal system when Cs^+ ions are fully doped. It has been proved that Cs-HTBs illustrate strong localized surface plasmon resonance (LSPR) phenomenon which is the crucial property of Cs-HTBs to shield the near-infrared radiation from the sunlight [53, 146, 147]. As for Cs-CTBs shown in Figure 5.2b, the Cs^+ ions can be seen in the cubic channels, and Cs-CTBs do not have the same strong LSPR as Cs-HTBs.

The XRD pattern of CWO-1 can be attributed to a mixed crystal phase of the cubic $(Cs_2O)_{0.44}W_2O_6$ (JCPDS 47-0566) and hexagonal $Cs_{0.2}WO_3$ (JCPDS 83-1333). CWO-1 were prepared in absolute ethanol without any other reducing additives. The results reveal that absolute ethanol cannot fully promote the synthesis of hexagonal phase nanocrystals and thus the doping of Cs^+ ions is restricted. As for CWO-2, a small diffraction peak belonging to cubic

$(Cs_2O)_{0.44}W_2O_6$ (JCPDS 47-0566) was observed and other diffraction peaks of CWO-2 agreed well with the hexagonal diffraction peaks of $Cs_{0.3}WO_3$ (JCPDS 81-1244). CWO-2 were synthesized in absolute ethanol with tartaric acid. The results indicate that more Cs^+ ions entered into the hexagonal tunnels of the crystal structure due to the stronger reducibility of absolute ethanol with tartaric acid, but cubic phase still existed in the as-synthesized nanocrystals.

Figure 5.3 shows the reducing process of tartaric acid for the synthesis of Cs-HTBs. The two carboxyl groups of tartaric acid tended to conduct decarboxylation under the stimulation of α-hydroxyl group and β-hydroxyl group. The generated free hydrogen atoms ([H]) with strong reducibility took the oxygen atoms of $[WO_6]$ octahedrons to change W^{6+} ions into W^{5+} ions, which promoted Cs^+ ions entering into the crystal structure. It can be seen that the XRD pattern of CWO-3 was well indexed to the pure hexagonal $Cs_{0.33}WO_3$ (JCPDS 83-1334), suggesting that the most Cs^+ ions are doped into the lattice structure. CWO-3 were obtained in absolute ethanol with the presence of the tartaric acid and the chloroplatinic acid. Figure 5.3b presents the process of the chloroplatinic acid enhancing the reducibility of the tartaric acid during the controllable one-pot synthesis, and the role of the chloroplatinic acid here was regarded as Pt-catalysis. The mechanism of Pt-catalysis can be described as follows. Firstly, Pt^{4+} ions derived from chloroplatinic acid obtained free electrons and was reduced to metallic platinum by tartaric acid. Subsequently, H^+ ions decomposed from tartaric acid got electrons from metallic platinum to turn into [H] with higher reducibility, while metallic platinum lost electrons and transformed Pt^{4+} ions again. Finally, the produced [H] with higher reducibility took the oxygen atoms of $[WO_6]$ octahedrons to generate H_2O and oxygen vacancies, while W^{6+} ions turned into W^{5+} ions by getting electrons originated from oxygen vacancies. Thus, the charge imbalance caused by

W^{5+} ions promoted Cs^{+} ions entering into lattice structure to form hexagonal phase. The reducibility of the reducing agents is thought to be important in the formation of the hexagonal phase, indicating that Pt-catalysis facilitates the reducing reaction and causes the doping of Cs^{+} ions to a higher degree. In addition, it is found that the diffraction peak intensity increased in the order of CWO-1, CWO-2 and CWO-3, indicating that the reducing agent with higher reducibility stimulate the growth of nanocrystals and cause a higher crystallinity.

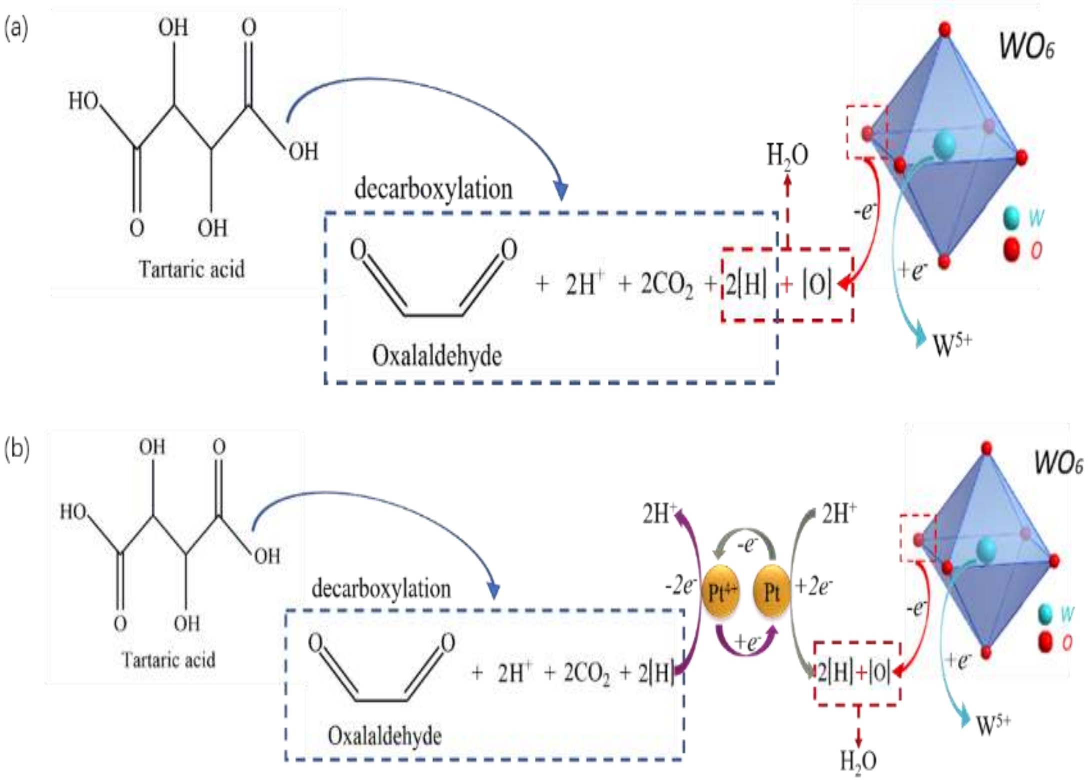

Figure 5.3 The reaction diagram of reducing process under different reducing agents: (a) tartaric acid and (b) tartaric acid with chloroplatinic acid.

As inspired by the reducing mechanism shown in Figure 5.3b, chemical reactions were described via the following equations. Firstly, AMT (Ammonium metatungstate hydrate) resolved into WO_3, NH_3 and H_2O with the increase of reaction temperature. Oxalaldehyde ($C_2H_2O_2$), carbon dioxide (CO_2) and hydrogen ions (H^{+}) were the by-products of tartaric acid after the reaction. H_2O was obtained by the combination of the [H] and oxygen atoms of [WO_6]. The expression of the product presented by $Cs_{0.33}WO_{2.835}$ was used to balance the reaction equation, and it is widely believed that Cs-HTBs were defined as $Cs_{0.33}WO_3$.

$$(NH_4)_6H_2W_{12}O_{40} \cdot aH_2O \rightarrow 6NH_3 + 12WO_3 + (a + 4)H_2O \tag{5.1}$$

$$WO_3 + 0.33Cs^+ + 0.165C_4H_6O_6 \rightarrow Cs_{0.33}WO_{2.835} + 0.165C_2H_2O_2 + 0.33H^+ + 0.33CO_2 + 0.165H_2O \tag{5.2}$$

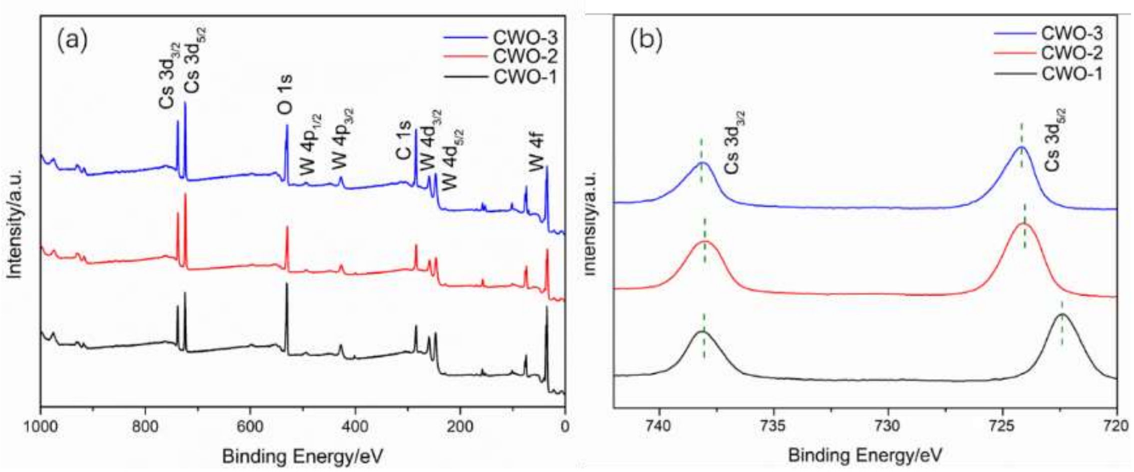

Figure 5.4 (a) XPS survey spectra and (b) Cs 3d core-level spectra of CWO-1, CWO-2 and CWO-3

The chemical composition and W valence state were investigated by XPS analysis. Figure 5.4a presents the survey spectra of CWO-1, CWO-2 and CWO-3. All the spectra confirm the presence of Cs, W and O elements, and no other elements could be observed except for C element. As shown in Figure 5.4b, the difference of Cs 3d characteristic peak position suggests that the Cs^+ ions chemical environment in CWO-1, CWO-2 and CWO-3 changes with the different reducing agent. Cs^+ ions were surrounded by O atoms with a certain degree of electronegativity in the hexagonal structure. As more Cs^+ ions enter the hexagonal tunnel, the Cs 3d characteristic peak position moves in the direction of higher binding energy. As a result, there were more Cs$^+$ ions in CWO-3's hexagonal tunnels.

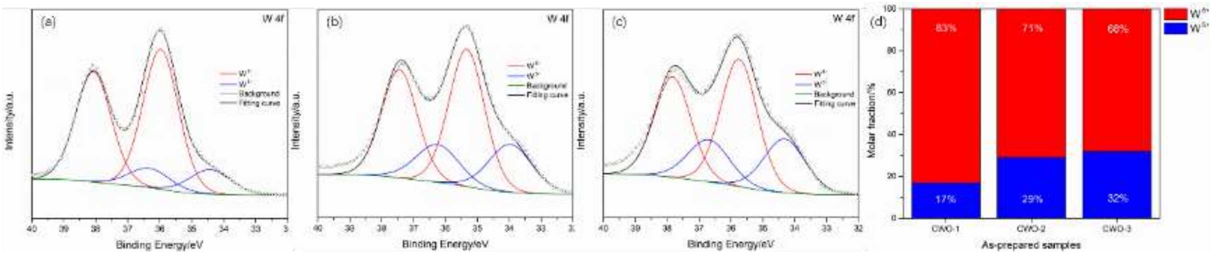

Figure 5.5 The W4f core-level spectra of (a) CWO-1, (b) CWO-2 and (c) CWO-3; (d) The valence distribution of W element in CWO-1, CWO-2 and CWO-3.

Figure 5.5a-c display the W 4f core-level spectra of CWO-1, CWO-2 and CWO-3 synthesized using different reducing agents. The spin-orbital peaks located at 34.2 eV/ 36.7 eV and 35.8 eV/37.9 eV can be attributed to the W^{5+} and W^{6+} respectively [39, 47, 148]. As shown in Figure 5d, the content of W^{5+} in CWO-3 is the largest, accounting for 32% of total W atoms. This indicates that the increase of W^{5+} generation is caused by more Cs$^+$ ions insertion, which plays a positive influence on the NIR shielding performance based on localized surface plasmon resonance (LSPR) [37].

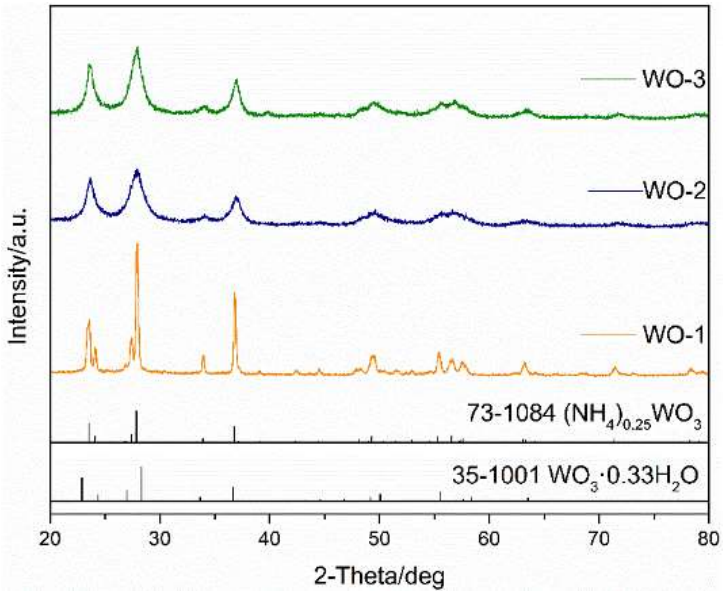

Figure 5.6 XRD patterns of WO-1, WO-2 and WO-3.

The XRD patterns of WO-1, WO-2, and WO-3, which correspond to CWO-1, CWO-2, and

CWO-3 without Cs doping, are shown in Figure 5.6. It can be seen that the XRD pattern of WO-1 agreed well with the hexagonal $(NH_4)_{0.25}WO_3$ (JCPDS 73-1084), indicating that NH_4^+ ions can be effectively doped into the crystal structure in the absence of Cs sources. As for WO-2 and WO-3, the two XRD patterns presented a mixed phase composition. The appearance of $WO_3 \cdot 0.33H_2O$ (JCPDS 35-1001) indicates that the addition of tartaric acid is not conducive for NH_4^+ ions entering into the crystal structure [146, 149, 150]. In other words, tartaric acid can promote Cs^+ ions getting into the crystal structure even in the presence of NH_4^+ ions. In addition, it is found that the characteristic peak intensity of WO-3 slightly increased compared with that of WO-2, suggesting that Pt-catalysis can facilitate the growth of nanocrystals.

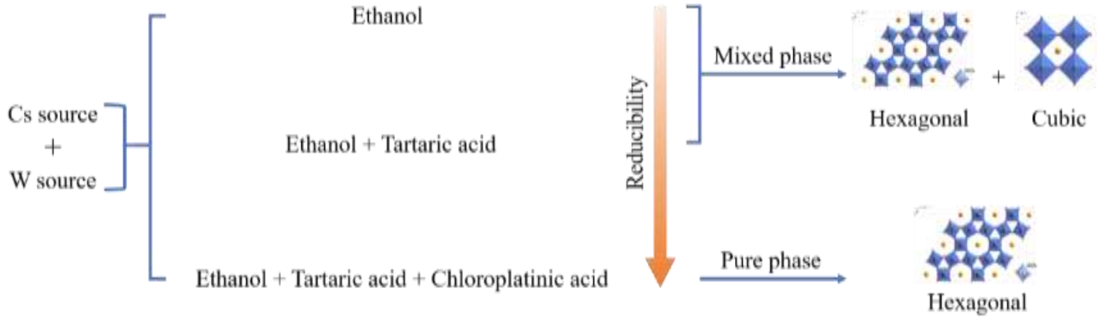

Figure 5.7 Schematic diagram of the growth mechanism of as-synthesized nanocrystals with different phase composition.

According to the discussion above, a brief diagram of synthetic routes was shown in Figure 5.7. It is found that the presence of Cs and W source was the prerequisite to prepare desired phase samples. Moreover, the phase composition was determined by the reducibility of reducing agents. It can be seen that a mixed composition of hexagonal and cubic phase was obtained in ethanol or ethanol with tartaric acid, indicating that the reducibility of the two conditions is not enough to prepare nanocrystals with a pure hexagonal phase. When chloroplatinic acid was added, the Cs-HTBs were successfully synthesized due to improved reducibility assisted by Pt-catalysis.

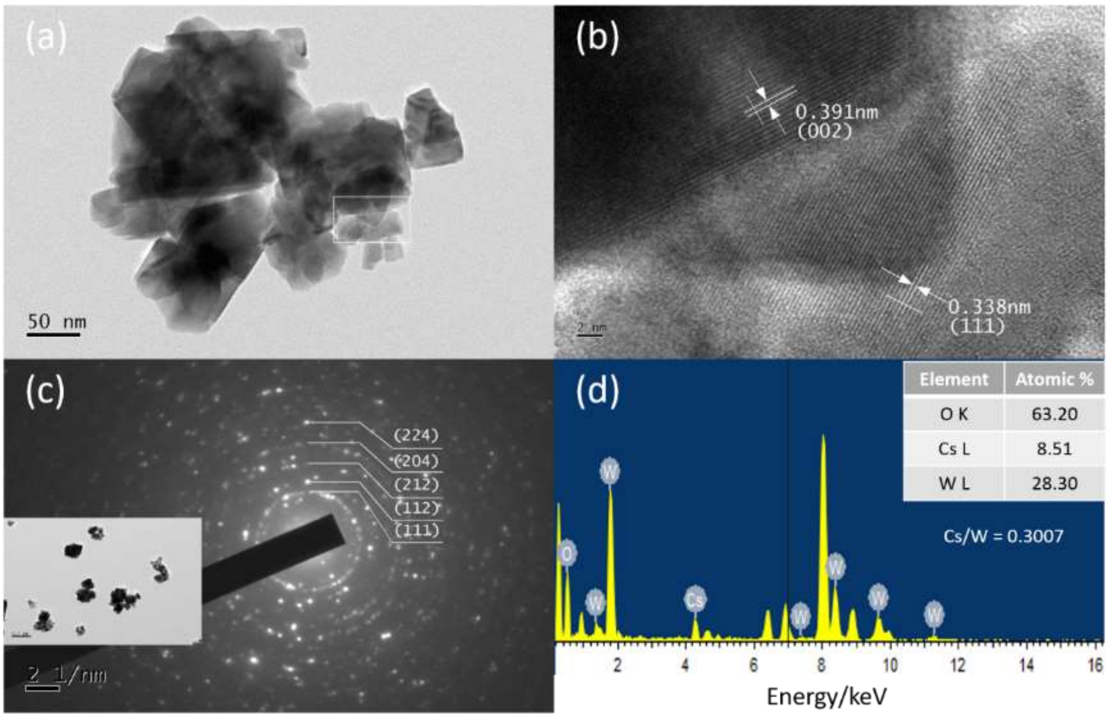

Element	Atomic %
O K	63.20
Cs L	8.51
W L	28.30

Figure 5.8 (a) TEM image, (b) HRTEM image of selected area, (c) SAED pattern with diffraction area inset and (d) EDS pattern of CWO-3.

More detailed structural information was determined using transmission electron microscopy (TEM). Figure 5.8 presents the TEM image, HR-TEM image, SAED pattern and EDS pattern of CWO-3. As shown in Figure 5.8a, most of prepared nanoparticles show rectangle-like shape with a certain extent of agglomeration. Figure 5.8b is the HR-TEM image of selected area in Figure 5.8a and the lattice spacing is 0.391 nm and 0.338 nm, which is determined as plane of (002) and (111) respectively. CWO-3 with hexagonal crystal structure was further confirmed by the SAED pattern displayed in Figure 5.8c. The element composition is shown in Figure 5.8d, indicating the existence of Cs, W and O element. Besides, the calculated Cs/W molar ratio was 0.3007, which is quite close to the upper limit of 0.33 for Cs-HTBs.

5.4 Conclusions

Hexagonal Cs_xWO_3 nanocrystals were successfully prepared by controllable solvothermal method using stable and relatively cheap raw materials. Tartaric acid with chloroplatinic acid as the reducing agent had the highest reducibility and could produce the most W^{5+} ions in the final product. It has been established that chloroplatinic acid has a significant impact on tartaric acid reducibility. This work is of great significance for synthesizing low-cost hexagonal Cs_xWO_3 nanocrystals without post heat-treatment and promoting the development of energy-efficient windows.

Chapter 6

Development of tunable near-infrared localized surface plasmon resonance and small polaron transfer of Cs_xWO_3 nanocrystals through various doping strategies

6.1 Introduction

At present, the synthesis of Cs_xWO_3 mainly focuses on doping the alkali ions into the hexagonal tunnels, and the theoretically topmost limit of x is 1/3. However, the trigonal cavities created by correlated corner-sharing WO_6 octahedra and occupied by small ions are neglected in the hexagonal structure. The empty trigonal tunnels in Cs_xWO_3 furnish the opportunity for the introduction of more free electrons. The theoretical ratio of empty trigonal tunnels and hexagonal tunnels is 2/1, so it is of great potential for Cs_xWO_3 to exhibit stronger LSPR when some suitable ions are incorporated into the empty trigonal tunnels [37, 151]. In addition, fluorine has been widely introduced into the lattice to enhance the optical property in transparent conducive oxides (TCOs). Generally, the doped fluorine substitutes the oxygen sites to form F-doped CdO [94, 101, 152], F-doped In_2O_3 [153] and F-doped SnO_2 [97, 154]. In theory, fluorine doping is of the following advantages. Firstly, the radius of F is a little smaller than that of O and F demonstrates higher electronegative than O, so the substitutional process of O by F can easily arise [153-155]. Moreover, it has been reported that the some doped ions in the lattice acted as a scattering center which limited the highest concentration of free carrier density, but F atoms appear as electron donors as it has one more valence electron than an O atom. Furthermore, compared with cationic substitution doping, the scattering level and decrease of carrier mobility of free electrons can be minimized by anionic F doping. To date, the synthesis of Li, F-codoped Cs_xWO_3 have never been investigated systematically. Besides, deep insights among charge carrier density, free carrier mobility and LSPR still lack. Thus, it remains essential to promote novel WO_3-based materials with spectral selectivity for energy-efficient windows application to satisfy the high standards of energy conservation and emission reduction of greenhouse gas.

Li-doped, F-doped, and Li, F-codoped Cs_xWO_3 nanocrystals have been successfully synthesized for the application of energy-efficient windows in this chapter using a controllable one-pot method, which expands the spectral tunability of LSPR and small polaron transfer. The effects of Li and F on the phase composition, valence state distribution of W, optical properties and microstructure of the as-prepared products have been investigated. Besides, the detailed mechanism for enhancing the near-infrared shielding performance and the effects of charge carrier density and free carrier mobility on LSPR and small polaron transfer have been discussed. The introduction of LiF breaks through the limited tunability of LSPR and small polaron transfer in Cs_xWO_3 nanocrystals. In addition, this method provides a promising way to regulate the free carrier density and enhance the near-infrared shielding performance in some related nanocrystal systems.

6.2. Experimental study

6.2.1 Materials

Ammonium metatungstate hydrate (AMT, $(NH_4)_6H_2W_{12}O_{40} \cdot aH_2O$), cesium carbonate

(Cs_2CO_3), tartaric acid (TA, $C_4H_6O_6$), deionized water (H_2O), anhydrous ethanol (C_2H_5OH), lithium chloride (LiCl), lithium fluoride (LiF) and cesium fluoride (CsF) were purchased from Macklin.

6.2.2 Synthesis of Li-doped Cs_xWO_3 nanocrystals

The Li-doped Cs_xWO_3 nanocrystals were prepared by controllable one-pot method using AMT as W source, Cs_2CO_3 as Cs origin and LiCl as Li origin respectively. After putting a certain amount of AMT into ethanol with 1 mol/L tartaric acid, Cs_2CO_3 and LiCl were added to the AMT solution with a Cs/W molar ratio of 0.33. The mixed solution had a total volume of 70 ml. The as-prepared solution was then placed in a PTFE autoclave with a 50 mL interval volume, and the solvothermal reaction was carried out in a drying oven at 240 °C. The Li-doped Cs_xWO_3 nanocrystals synthesized with the Li/W molar ratio of 0.2, 0.4, 0.6, 0.8 were labeled as 0.2-LiCWO, 0.4-LiCWO, 0.6-LiCWO and 0.8-LiCWO respectively. The nanocrystals prepared without Li doping were marked as CWO.

6.2.3 Synthesis of F-doped Cs_xWO_3 nanocrystals

The F-doped Cs_xWO_3 nanocrystals were prepared by controllable one-pot method using AMT as W source, CsF as Cs and F origin respectively. First, a small amount of AMT was dissolved in ethanol with 1 mol/L tartaric acid, and then CsF were added to the AMT solution with a Cs/W molar ratio of 0.2, 0.4, 0.6, and 0.8. The mixed solution had a total volume of 70 ml. The solution was then placed in a PTFE autoclave with a 50 mL interval volume and the solvothermal reaction was carried out in a drying oven at 240 °C. The F-doped Cs_xWO_3 nanocrystals synthesized with the F/W molar ratio of 0.2, 0.4, 0.6, 0.8 were labeled as 0.2-

FCWO, 0.4-FCWO, 0.6-FCWO and 0.8-FCWO respectively. The nanocrystals prepared with Cs/W molar ratio of 0.33 but without F doping were marked as CWO using Cs_2CO_3 as Cs source.

6.2.4 Synthesis of Li, F-codoped Cs_xWO_3 nanocrystals

The Li-doped Cs_xWO_3 nanocrystals were prepared by controllable one-pot method using AMT as W source, Cs_2CO_3 as Cs origin and LiF as Li, F origin respectively. After putting a certain amount of AMT into ethanol with 1mol/L tartaric acid, Cs_2CO_3 and LiF were added to the AMT solution with a Cs/W molar ratio of 0.33. The mixed solution had a total volume of 70 ml. After that, the as-prepared solution was placed in a PTFE autoclave with a 50 mL interval volume, and the solvothermal reaction was carried out in a drying oven at 240 °C for 30 min. The Li, F-codoped Cs_xWO_3 nanocrystals synthesized with the LiF/W molar ratio of 0.2, 0.4, 0.6, 0.8 were labeled as 0.2-LiFCWO, 0.4-LiFCWO, 0.6-LiFCWO and 0.8-LiFCWO respectively. The nanocrystals prepared without Li doping were marked as CWO.

6.2.5 Characterization

X-ray diffraction (XRD) with Cu K radiation was used to determine the phase components of as-prepared nanocrystals. Transmission electron microscopy (TEM) with an energy dispersive spectrum (EDS) attachment was used to examine the nanocrystals' microstructure. X-ray photoelectron spectroscopy was used to investigate the chemical components and binding energies of W 4f (XPS).The Hall effect measurements were carried out on LakeShore HL5500 and performed on pellets (10 mm diameter) made by pushing the obtained powders under a pressure of 40 MPa.

6. 3 Results and discussion

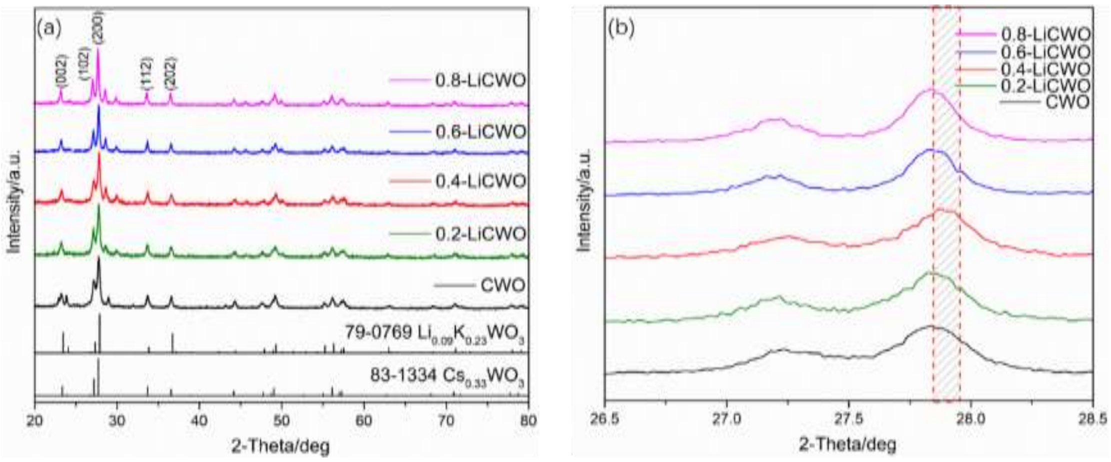

Figure 6.1 (a) XRD pattens, (b) high-resolution patterns corresponding to crystal plane (102) and (200) of CWO, 0.2-LiCWO, 0.4-LiCWO, 0.6-LiCWO and 0.8-LiCWO.

Figure 6.1 shows the XRD patterns of CWO, 0.2-LiCWO, 0.4-LiCWO, 0.6-LiCWO and 0.8-LiCWO and their high-resolution patterns corresponding to crystal plane (102) and (200). According to Figure 6.1a, when the molar ration of Li/W increased to 0.4, a pure hexagonal Cs_xWO_3 phase has been formed without impurities peaks. When the molar ration of Li/W is higher than 0.4, the peak intensity ratio of (112) plane relative to (202) presents a decreasing trend. As for the standard pattern of $Li_{0.09}K_{0.23}WO_3$ (JCPDS 79-0769), the peak intensity of crystal plane (202) is higher than that of crystal plane (112).The results indicate that insignificant amount of impurity phase appeared besides dominant hexagonal $Cs_{0.33}WO_3$ phase. The separation degree of (102) and (200) diffraction peaks increased as the Li/W molar ratio increased, so the peak intensity ratio of crystal planes (200) and (102) was higher than the standard level of $Cs_{0.33}WO_3$ phase, revealing the preferential growth of the nanocrystals along the *a*-axes. As shown in Fig 6.1b, the (200) plane diffraction peak of 0.4-LiCWO slightly shifted to higher angle, suggesting that the (200) plane spacing becomes smaller. According to the

Bragg equation, this is as follows:

$$2d \sin\theta = n\lambda \tag{6.1}$$

where d stands for crystal interplanar spacing, θ represents incident angle, λ denotes incident light wavelength, and n stands for reflection order. Because $n\lambda$ is a constant, increasing it implies a decrease in crystal interplanar spacing.

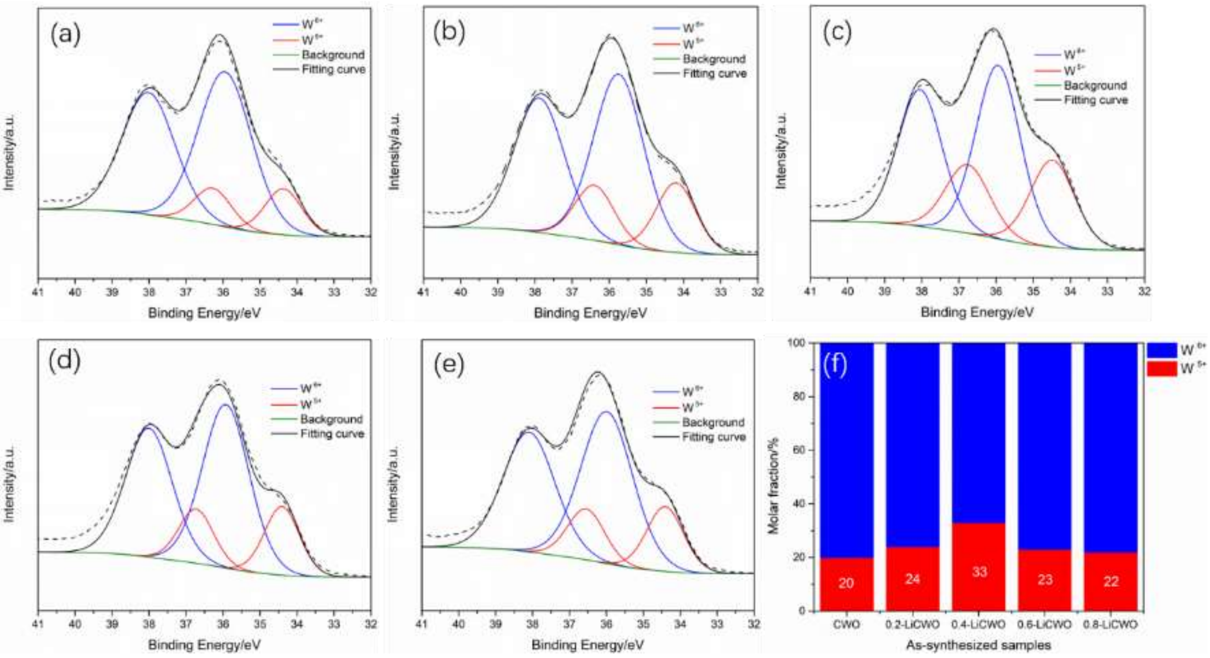

Figure 6.2 The W4f core-level spectra of (a) CWO, (b) 0.2-LiCWO, (c) 0.4-LiCWO, (d) 0.6-LiCWO, (e) 0.8-LiCWO; (d) The valence distribution of W element in CWO, 0.2-LiCWO, 0.4-LiCWO, 0.6-LiCWO and 0.8-LiCWO.

The W 4f core-level spectra of CWO, 0.2-LiCWO, 0.4-LiCWO, 0.6-LiCWO, and 0.8-LiCWO are shown in Figure 6.2a-e. W 4f 5/2 and W 4f 7/2 are two spin-orbital peaks that can be fitted to the W 4f curve. W^{5+} and W^{6+} are responsible for the spin-orbital peaks at 34.2 eV/ 36.7 eV and 35.8 eV/37.9 eV, respectively. As shown in Figure 6.2f, the content of W^{5+} in 0.4-LiCWO is the largest, accounting for 33 % of total W atoms. The results indicate that the increase of W^{5+} generation is caused by more Li^{+} ions insertion in trigonal tunnels, which plays an active influence on enhancing the NIR shielding performance based on LSPR [37]. Nevertheless, when the Li/W molar ratio was higher than 0.4, the content of W^{+5} decreased to 23 % and 22 % corresponding to 0.6-LiCWO and 0.8-LiCWO, respectively. It was discovered that alkali metal ions with the appropriate content had a positive effect on improving optical performance.

Table 6.1 The molar ratio of Cs/W and Li/W in nanocrystal samples measured by ICP-OES

Sample	Cs/W content (mol %)	Li/W content (mol %)
CWO	30.7	0
0.2-LiCWO	31.2	11.2
0.4-LiCWO	31.6	20.7
0.6-LiCWO	26.4	24.3
0.8-LiCWO	24.3	26.8

To investigate the impact of Li doping on the chemical composition of the samples as-prepared, the molar ratios of Cs/W and Li/W (mol %) in the samples were measured by ICP-OES which can provide the content of Cs and Li in the whole samples. The doping ratio of Li/W was 0.2, 0.4, 0.6 and 0.8 respectively. As listed in Table 6.1, the actual Cs/W molar ratio first showed an increasing trend as Li doping increased. When the doping ratio of Li/W reached 0.4, the actual Cs/W content attained maximum value of 31.6 %, which was close to theoretical Cs/W value of 33 %. Meanwhile, the actual Li/W content increased to 20.7 %. Proceeding to increase the Li doping level, the Cs/W content demonstrated a decreasing trend and reached 24.3 % when the doping ratio of Li/W was 0.8. The actual Li/W content in the as-prepared sample presented a small increasing extent with the increase of Li doping from 0.4 molar ratio.

A reasonable explanation for the above results is that Li^+ ions enter into the hexagonal tunnels from hexagonal tunnels with the increase of Li doping level. Specifically, Li^+ ions enter into and occupy the trigonal tunnels when the Li doping level is low. As for 0.4-LiCWO, it can be seen that actual Li/W content is 20.7 % with the measured Cs/W content of 31.6 % which is close to the theoretical value of 33 %. As the precursor's Li^+ ion concentration rises, the smaller Li^+ ions tend to enter into the hexagonal tunnel that should be occupied by Cs^+ ions during the solvothermal reaction process. Although the actual Li/W content presented an increasing trend and attained 26.8 % for 0.8-LiCWO, the actual Cs/W molar ratio showed a decreasing tendency from 0.4-LiCWO and reached 24.3 % for 0.8-LiCWO. It can be obtained that Cs^+ ions have begun to leave the hexagonal tunnels in the crystal structure from 0.4-LiCWO, which is not conducive to the crystalline stability and its optical performance.

The Beer-Lambert Law can be described as following eq (6.2):

$$A = \frac{N\sigma L}{\log(10)} \tag{6.2}$$

Where A represents the measured absorbance of the dilute nanocrystal dispersion and is expressed in log (10) scale, N indicates the number density of the nanocrystals (M, mol/L), and L (mm) stands for path length through the cuvette. Thus, the absorption coefficient σ (M^{-1} mm^{-1}) of the nanocrystals can be calculated by the above equation using the measured absorbance of the dispersion with known molar concentration and the path length.

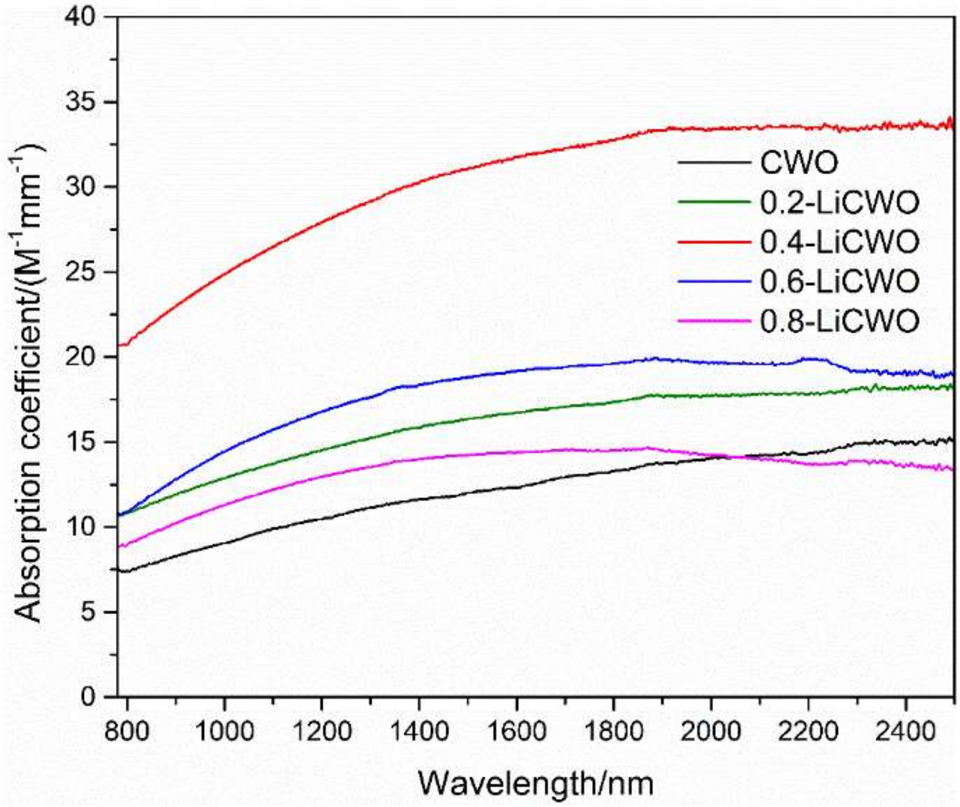

Figure 6.3 The absorption coefficient spectra of CWO, 0.2-LiCWO, 0.4-LiCWO, 0.6-LiCWO and 0.8-LiCWO.

To examine the effect of various Li doping concentration on the absorption coefficient of the as-prepared nanocrystals, the absorbance of the dilute dispersion containing the as-prepared nanocrystals was measured. Figure 6.3 presents the calculated absorption coefficient spectra of all as-synthesized nanocrystals across a set of Li doping concentration. A significant increase in the absorption coefficient can be observed as the dopant concentration increases. As shown in Figure 6.3, the absorption coefficient spectrum of 0.4-LiCWO presents the best absorption potential of all the samples. However, for the samples with the Li/W molar ratio of higher than 0.4, the absorption coefficient illustrated a decreasing trend. The results indicate that there must be changes in the optical parameters of the nanocrystals, which is discussed in detail in the following content.

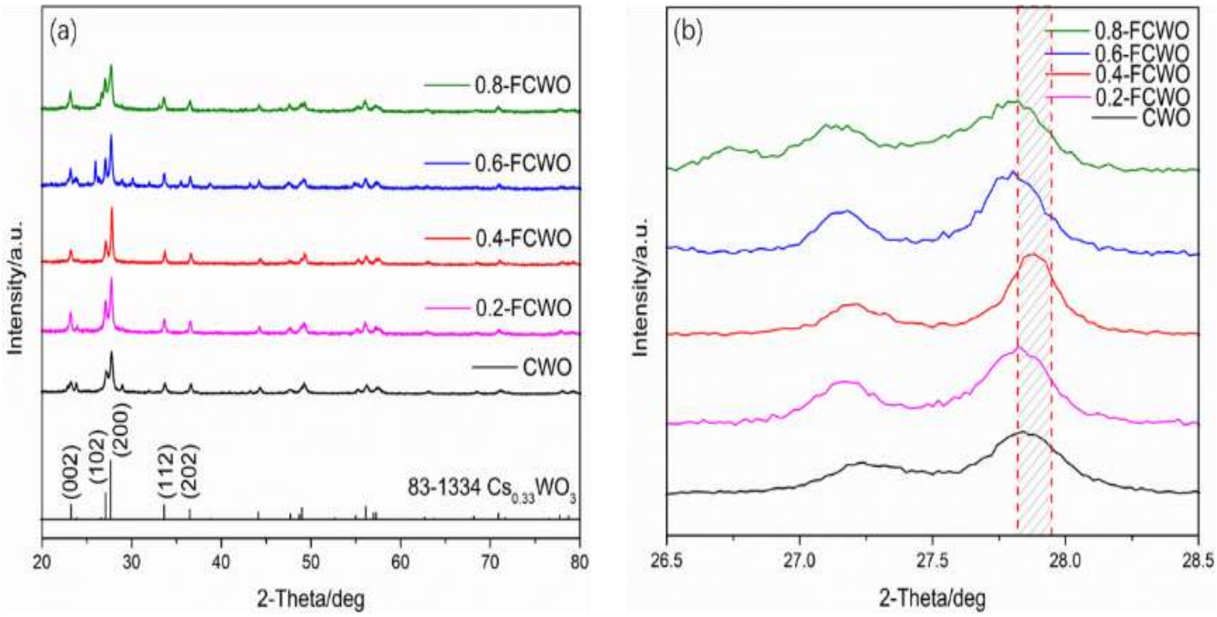

Figure 6.4 (a) XRD pattens, (b) high-resolution patterns corresponding to crystal plane (102) and (200) of CWO, 0.2-FCWO, 0.4-FCWO, 0.6-FCWO and 0.8-FCWO.

Figure 6.4 illustrates the XRD patterns of CWO, 0.2-FCWO, 0.4-FCWO, 0.6-FCWO and 0.8-FCWO and their high-resolution patterns corresponding to crystal plane (102) and (200). As shown in Figure 6.4a, when the molar ratio of F/W reached 0.2 and 0.4, a pure hexagonal Cs_xWO_3 phase was obtained without impurity peaks. The crystallinity of 0.4-FCWO nanocrystals is higher than that of 0.2-FCWO, indicating that increasing the F/W molar ratio promotes the crystallization of as-synthesized nanocrystals to some extent. As for 0.6-FCWO and 0.8-FCWO, impurity peaks appeared, indicating that other phase component has been formed in the nanocrystals besides dominant hexagonal $Cs_{0.33}WO_3$ phase. With increasing F/W molar ratio, the peak intensity ratio of crystal plane (002) relative to crystal plane (102) shows an increasing trend, indicating that nanocrystals preferentially grow along the *c*-axes. The (200) plane diffraction peak of 0.4-FCWO shifted to a higher angle, as shown in Figure 6.4b, implying that the (200) plane spacing shrinks.

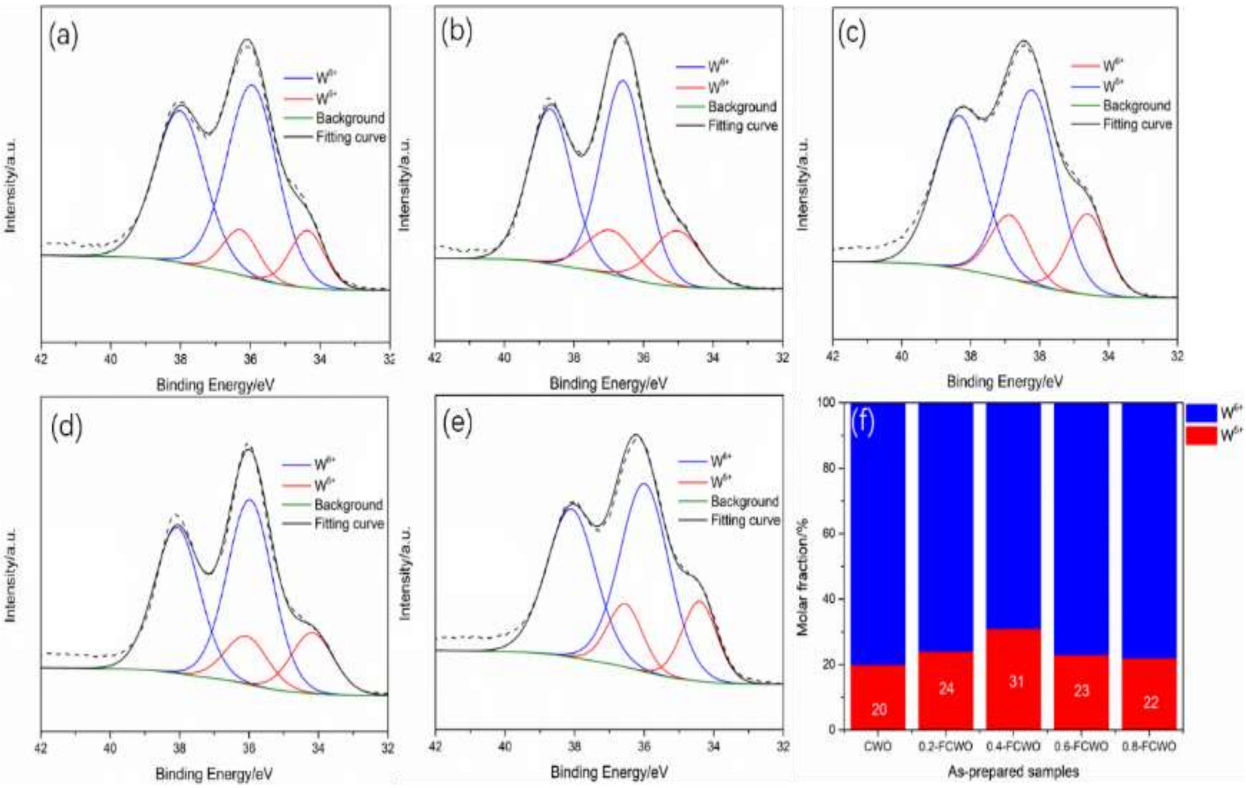

Figure 6.5 The W4f core-level spectra of (a) CWO, (b) 0.2-FCWO, (c) 0.4-FCWO, (d) 0.6-FCWO, (e) 0.8-FCWO; (d) The valence distribution of W element in CWO, 0.2-FCWO, 0.4-FCWO, 0.6-FCWO and 0.8-FCWO.

The W 4f core-level spectra of CWO, 0.2-FCWO, 0.4-FCWO, 0.6-FCWO, and 0.8-FCWO are shown in Figure 6.5a-e. W 4f 5/2 and W 4f 7/2 are two spin-orbital peaks that can be fitted to the W 4f curve. W^{5+} and W^{6+} are responsible for the spin-orbital peaks at 34.2 eV/ 36.7 eV and 35.8 eV/37.9 eV, respectively. As shown in Figure 6.5f, the content of W^{5+} in 0.4-FCWO is the largest, accounting for 31 % of total W atoms. This indicates that the increase of W^{5+} generation is caused by more Cs and F ions insertion, which plays a significant impact on improving the NIR shielding performance based on LSPR [37]. However, when F/W molar was higher than 0.4, the content of W^{5+} decreased to 23 % and 22 % for 0.6-FCWO and 0.8-FCWO, respectively.

Table 6.2 The molar ratio of Cs/W and F/W in nanocrystal samples measured by XPS

Sample	Cs/W molar ratio	F/W molar ratio
CWO	0.31	0
0.2-FCWO	0.18	0.14
0.4-FCWO	0.30	0.21
0.6-FCWO	0.27	0.23
0.8-FCWO	0.25	0.24

The molar ratios of Cs/W and F/W in the samples were measured using XPS to further investigate the effect of F doping on the chemical composition of the as-prepared samples. F/W doping ratios were 0.2, 0.4, 0.6, and 0.8. As shown in Table 6.2, the Cs/W molar ratio of the doped samples first increased as the amount of F doping increased. When the doping ratio of F/W reached 0.4, the actual Cs/W content attained maximum value of 0.30, which was close to theoretical Cs/W value of 0.33. Meanwhile, the measured F/W content increased to 0.21. Proceeding to increase the F doping level, the Cs/W content demonstrated a decreasing trend and reached 0.26 when the doping ratio of F/W was 0.8. The F/W content in the as-prepared sample presented a small increasing extent with the increase of Li doping from 0.4 molar ratio.

The F/W content of 0.4-FCWO is 0.21, and the measured Cs/W content is 0.30, which is close to the theoretical value of 0.33. With the increase of F ions in the precursor, the small F ions tend to substitute the sites which are occupied by oxygen during the solvothermal reaction process. Although the F/W content presented an increasing trend and attained 0.24 for 0.8-FCWO, the Cs/W molar ratio showed a decreasing tendency from 0.4-FCWO and reached 0.26 for 0.8-FCWO, which is not conducive to the crystalline stability and its optical performance.

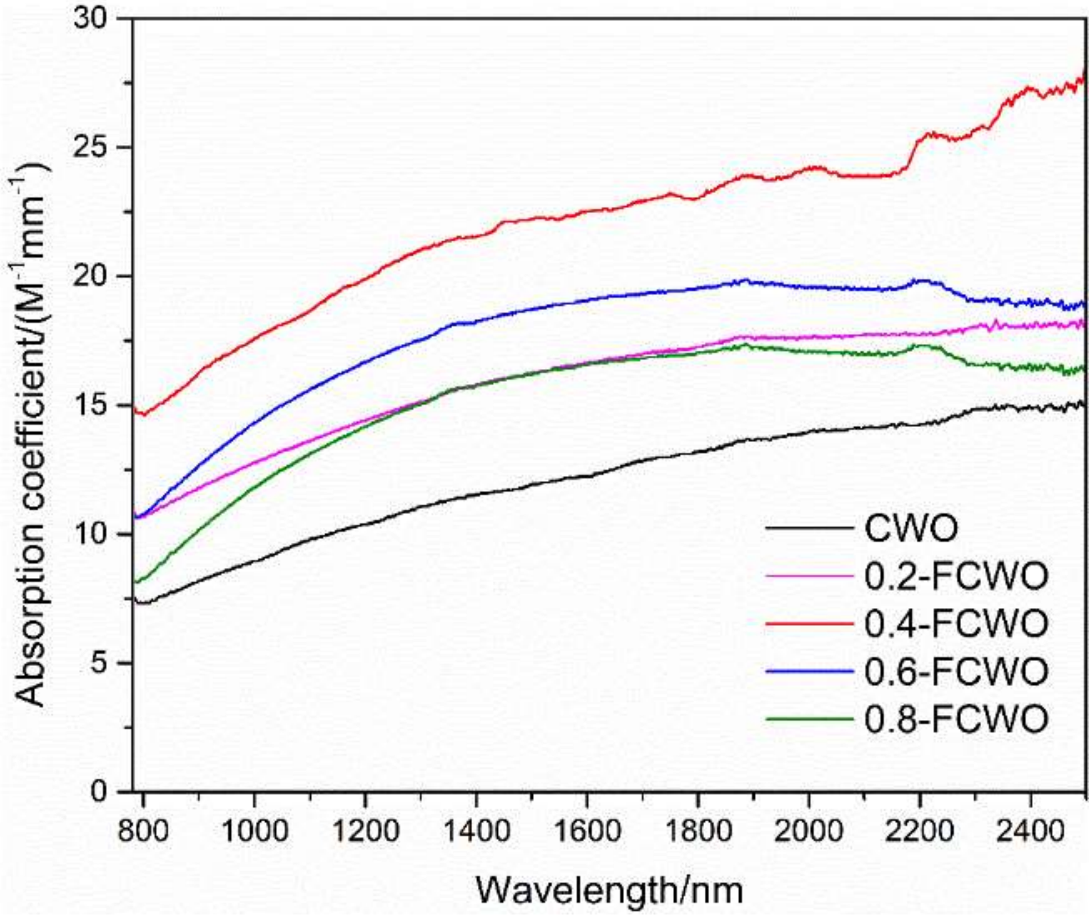

Figure 6.6 The absorption coefficient spectra of CWO, 0.2-FCWO, 0.4-FCWO, 0.6-FCWO and 0.8-FCWO.

To examine the effect of various F doping concentration on the absorption coefficient of the as-prepared nanocrystals, the absorbance of the dilute dispersion containing the as-prepared nanocrystals was measured. Figure 6.6 presents the calculated absorption coefficient spectra of all as-synthesized nanocrystals across a set of F doping concentration. A significant increase in the absorption coefficient can be observed as the dopant concentration increases. As shown in Figure 6.6, the absorption coefficient spectrum of 0.4-FCWO presents the best absorption potential of all the samples. However, for the samples with the F/W molar ratio of higher than 0.4, the absorption coefficient illustrated a slightly decreasing trend.

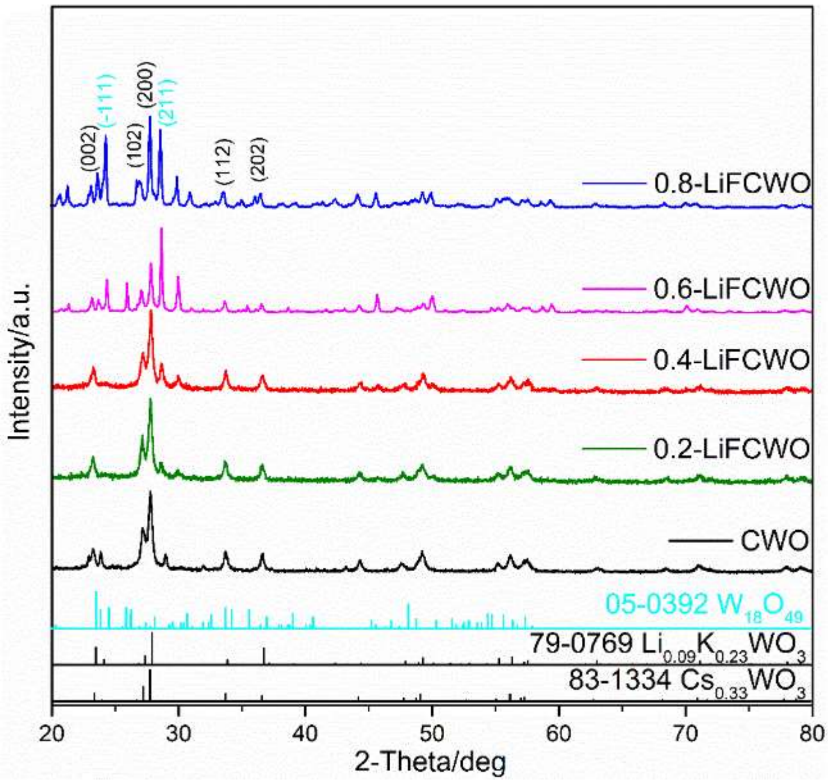

Figure 6.7 XRD patterns of CWO, 0.2-LiFCWO, 0.4-LiFCWO, 0.6-LiFCWO and 0.8-LiFCWO.

As shown in Figure 6.7, when the molar ration of LiF/W was increased to 0.4, a pure hexagonal cesium tungsten bronze has been formed without impurities. When the molar ration of LiF/W is equal to 0.6, insignificant amount of hexagonal phase $Li_{0.09}K_{0.23}WO_3$ (JCPDS NO. 79-0769) and monoclinic phase $W_{18}O_{49}$ (JCPDS NO. 05-0392) was appeared besides dominant hexagonal $Cs_{0.33}WO_3$ phase (JCPDS NO. 83-1334). The separation degree of the (200) and (102) diffraction peaks increased as the LiF proportion increased, which indicated that the product changed from $Cs_{0.33}WO_3$ (JCPDS NO. 83–1334) to $Li_{0.09}K_{0.23}WO_3$ phase (JCPDS NO. 79-0769). The results demonstrate that more Li^+ ions were doped into the crystal lattice of CWO. As for 0.6-LiFCWO and 0.8-LiFCWO, (-111) and (211) crystal planes of $W_{18}O_{49}$ (JCPDS NO. 05-0392) can be observed, which can be attributed to the highly substitutional fluorine doping in the crystal structure. The results suggest that impurity phases have appeared in 0.6-LiFCWO and 0.8-LiFCWO. Furthermore, the (200) peak's relative intensity to the (002) peak is higher than the standard level, revealing the preferential growth is along the *a*-axes for 0.4-LiFCWO. In addition, with the increase of LiF/W ratio, the (200) plane diffraction peak of 0.4-LiCWO slightly shifted to higher angle, suggesting that the (200) plane spacing becomes smaller.

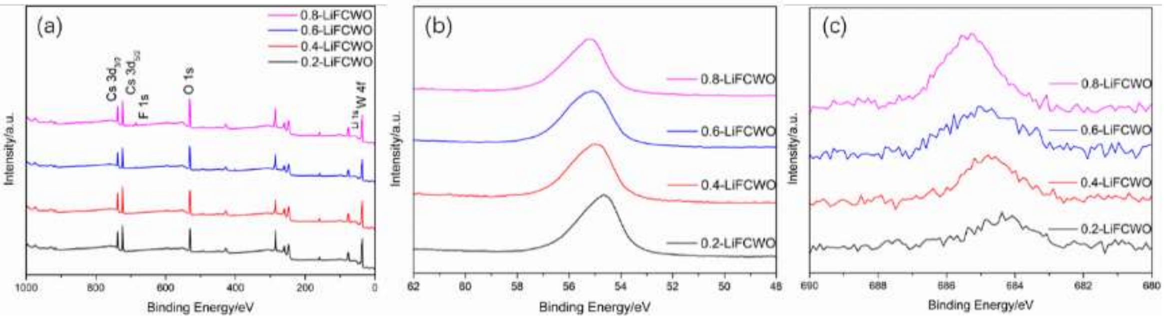

Figure 6.8 (a) XPS survey spectra, (b) Li 1s core-level spectra and (c) F is core-level spectra of 0.2-LiFCWO, 0.4-LiFCWO, 0.6-LiFCWO and 0.8-LiFCWO.

The chemical composition and W valence state were determined by XPS. Figure 6.8a shows the survey spectra of 0.2-LiFCWO, 0.4-LiFCWO, 0.6-LiFCWO and 0.8-LiFCWO. The change in peak position of Li 1s can be seen in Figure 6.8b, which indicates the chemical environment difference of Li^+ ions in the crystal lattice. Figure 6.8c presents the difference of F 1s characteristic peak position, which suggests that the F ions chemical environment in 0.2-LiFCWO, 0.4-LiFCWO, 0.6-LiFCWO and 0.8-LiFCWO changes with the different LiF/W molar ratio. Li and F ions are surrounded by O atoms with a certain degree of electronegativity in the hexagonal structure. More Li and F ions enter into the trigonal tunnel and thus their characteristic peak moves to the higher binding energy direction.

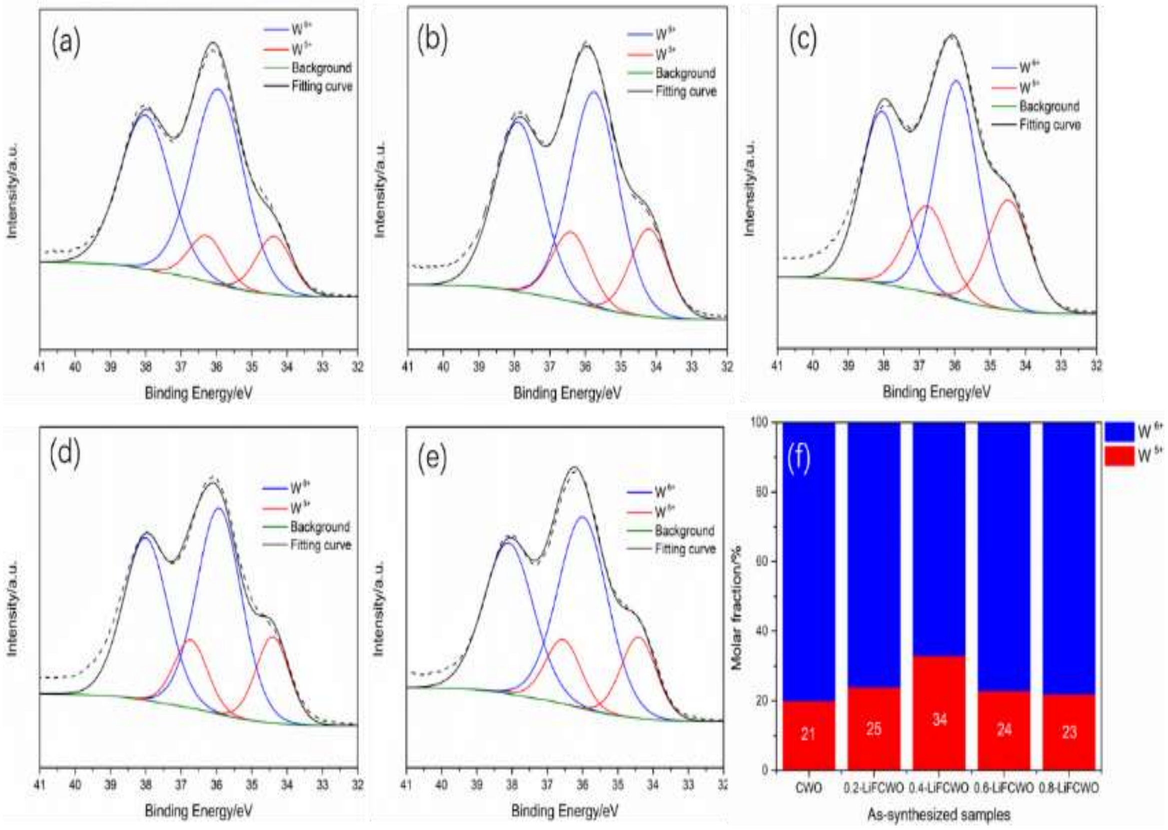

Figure 6.9 The W4f core-level spectra of (a) CWO, (b) 0.2-LiFCWO, (c) 0.4-LiFCWO, (d) 0.6-LiFCWO, (e) 0.8-LiFCWO; (d) The valence distribution of W element in CWO, 0.2-LiFCWO, 0.4-LiFCWO, 0.6-LiFCWO and 0.8-LiFCWO.

The core-level spectra of 0.2-LiFCWO, 0.4-LiFCWO, 0.6-LiFCWO, and 0.8-LiFCWO are shown in Figure 6.9a-e. Two spin-orbital peaks, W 4f 5/2 and W 4f 7/2, can be fitted to the W 4f curve. W^{5+} and W6^{+} are responsible for the spin-orbital peaks at 34.2 eV/ 36.7 eV and 35.8 eV/37.9 eV. As shown in Figure 6.9f, the content of W^{5+} in 0.4-LiFCWO is the largest, accounting for 34 % of total W atoms. This presents that the increase of W^{5+} is caused by more Li and F ions insertion in the crystal structure, which plays an active influence on the NIR shielding performance based on LSPR [37]. When the molar ratio of LiF/W was higher than 0.4, the content of W^{5+} presented an obvious decrease.

Table 6.3 The measured molar ratio of Cs/W, Li/W and F/W in nanocrystal samples measured by XPS

Sample	Cs/W molar ratio	Li/W molar ratio	F/W molar ratio
CWO	0.31	0	0
0.2-LiFCWO	0.30	0.11	0.13
0.4-LiFCWO	0.31	0.22	0.20
0.6-LiFCWO	0.26	0.24	0.22
0.8-LiFCWO	0.23	0.26	0.23

To investigate the impact of Li, F-codoping on the chemical composition of the samples as-prepared, the molar ratios of Cs/W, Li/W and F/W in the samples were measured by XPS measurement. The doping ratio of LiF/W was 0.2, 0.4, 0.6 and 0.8 respectively. As listed in Table 6.3, the measured Cs/W molar ratio firstly presented a slightly increasing tend with the increase of Li, F-codoping. When the doping ratio of reached 0.4, the measured Cs/W content attained maximum value of 0.31, which was close to theoretical Cs/W value of 0.33. Meanwhile, the measured Li/W content increased to 0.22 and the measured F/W content increased to 0.20. Proceeding to increase the Li,F-codoping level, the Cs/W content demonstrated a decreasing trend and reached 0.23 when the doping ratio of LiF/W was 0.8. With increasing Li doping from a codoping ratio of 0.4, the measured Li/W content in the as-prepared sample increased to a small extent. A reasonable explanation for the above results is that Li^+ ions enter into the hexagonal tunnels from hexagonal tunnels with the increase of Li doping level. Specifically, Li^+ ions enter into and occupy the trigonal tunnels when the Li doping level is low. As for 0.4-LiFCWO, it can be seen that measured Li/W content is 0.22 with the measured Cs/W content of 0.31. With the increase of Li^+ ions in the precursor, the smaller Li^+ ions tend to enter into the hexagonal tunnel that should be occupied by Cs^+ ions during the solvothermal reaction process. Although the measured Li/W and F/W content presented an increasing trend and attained 0.26 and 0.23 for 0.8-LiFCWO, the measured Cs/W molar ratio showed a decreasing tendency from 0.4-LiFCWO and reached 0.23 for 0.8-LiFCWO. It can be explained that Cs^+ ions have begun to leave the hexagonal tunnels in the crystal structure from 0.4-LiFCWO, which is not conducive to the crystalline stability and its optical performance.

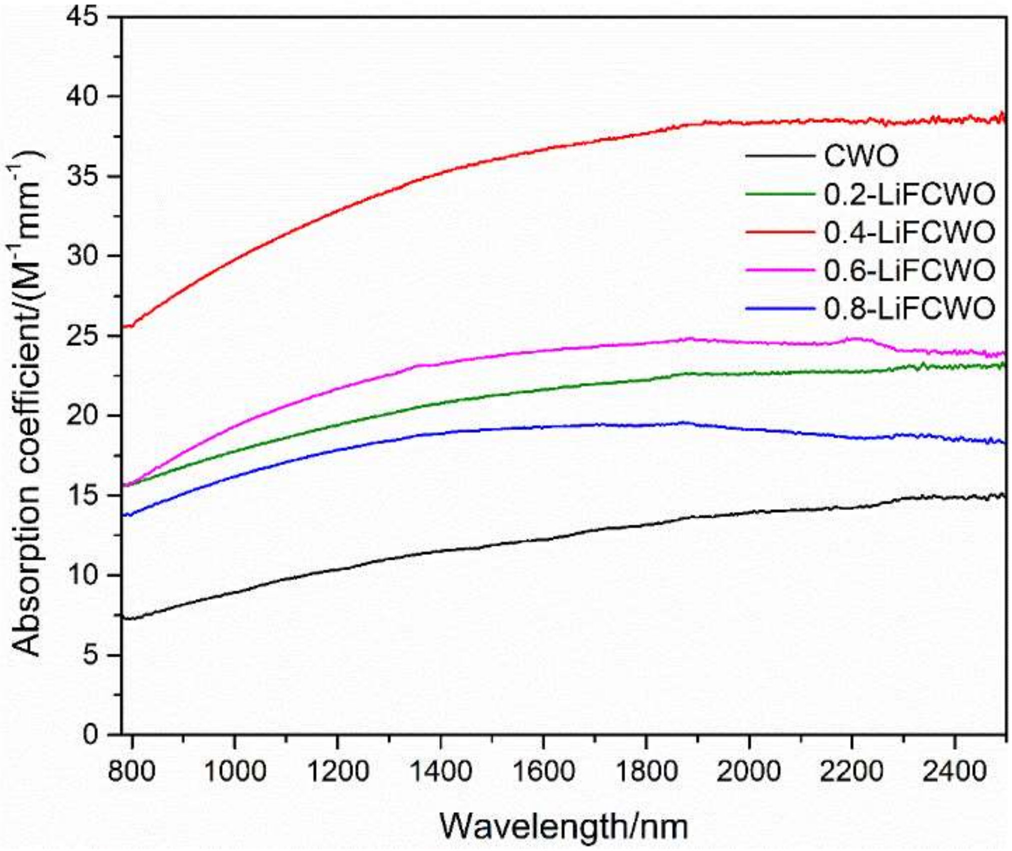

Figure 6.10 The absorption coefficient spectra of CWO, 0.2-LiFCWO, 0.4-LiFCWO, 0.6-LiFCWO and 0.8-LiFCWO.

To examine the effect of various Li, F-codoping concentration on the absorption coefficient of the as-prepared nanocrystals, the absorbance of the dilute dispersion containing the as-prepared nanocrystals was measured. Figure 6.10 presents the calculated absorption coefficient spectra of all as-synthesized nanocrystals across a set of Li, F-codoping concentration. A significant increase in the absorption coefficient can be observed as the dopant concentration increases. As shown in Figure 6.10, the absorption coefficient spectrum of 0.4-LiFCWO presents the best absorption potential of all the samples. However, for the samples with the LiF/W molar ratio of higher than 0.4, the absorption coefficient illustrated a decreasing trend. The results indicate that there must be changes in the optical parameters of the nanocrystals, which is discussed in detail in the following content.

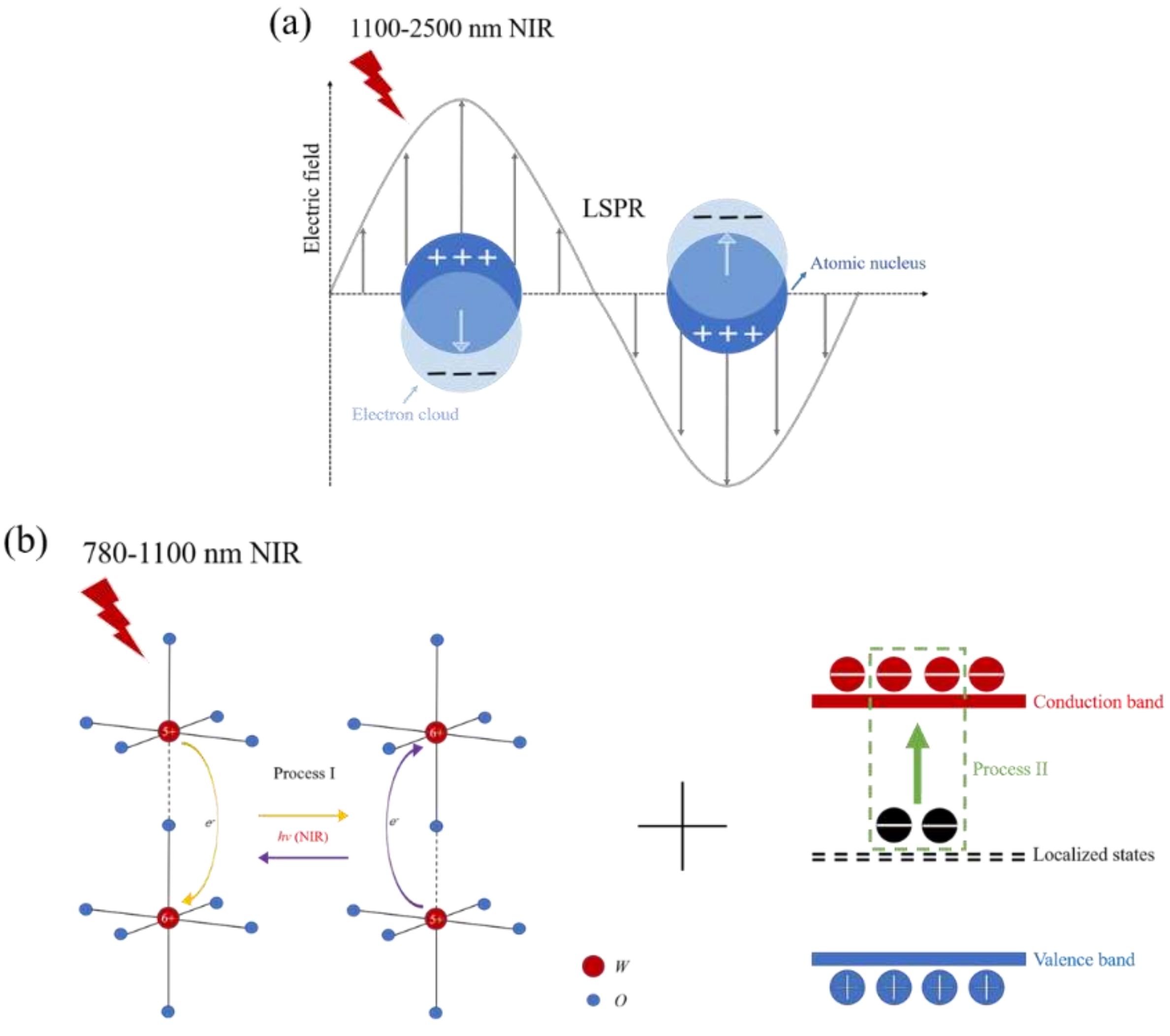

Figure 6.11 The schematic diagram of (a) LSPR under 1100-2500 nm NIR and (b) small polaron transfer under 780-1100 nm NIR.

According to the above results, the spectrally selective mechanism of Li, F-codoped Cs_xWO_3 nanocrystals is presented in Figure 6.11. The near-infrared (NIR) absorption of Cs-HTB nanoparticles is ascribed to LSPR and the small polaron transfer. LSPR of Cs-HTB nanoparticles mostly absorbs NIR radiation ranging from 1100nm to 2500nm [43]. The LSPR is triggered when the incoming radiation is close to the oscillation frequency of the free electrons in the conduction band. As shown in Figure 6.11a, a simplified model is presented based on Drude-Lorentz assumptions [77] [81, 156-162]. The free electrons contributed by the doped ions oscillate in phase with the corresponding electric field component of the sunlight, which results in the spectral selectivity. Moreover, small polaron transfer mainly absorbs the 780-1100nm NIR radiation and consists of two processes shown in Figure 6.11b [42]. When surplus electrons polarize their ambient lattice, polarons are formed and defined as the composite of lattice distortion and accompanying free electrons. The polarons absorb NIR light by hopping between two adjacent nonequivalent W ions. The polaron transition process is as follows:

$$\text{Process I: } h\nu + W^{5+}(a) + W^{6+}(b) \rightarrow W^{6+}(a) + W^{5+}(b) + E_{phonon} \tag{6.3}$$

where E_{phonon} represents single phonon energy

The electrons transferred between two adjacent nonequivalent W ions are regarded as originating from the doped alkali ions [37]. Besides, there are some electrons in localized states lower than the conduction band of nanoparticles. As shown in Process II, the electrons in localized states would transfer from localized state to conduction band led by absorbing suitable NIR energy. Thus, the majority near-infrared radiation of the sunlight can be effectively shielded by the spectrally selective coating prepared by Li, F-codoped Cs_xWO_3 nanocrystals through the above mechanism.

The Quality factor (Q-factor), a performance index derived from the LSPR response, can be used to assess the potential efficiency of creating intense localized electric fields. It is defined as the ratio of the LSPR peak energy to its full width at half-maximum (FWHM). It is found that the LSPR peak energy is mainly decided by LSPR frequency of the nanocrystals, whilst the FWHM signifies the degree of electron scattering. When impurities are doped into the crystal lattice, however, a compromise is reached because the dopants not only create free electrons (increasing the LSPR peak energy) but also act as electron scattering centers (increasing FWHM). As a result, it's critical to strike a balance between the two effects and raise the Q-factor. A high Q-factor indicates greater near-field improvement, extended plasmon lifespan and lower electronic damping. The LSPR frequency ω_{LSPR} can be depicted by eq (6.4)

$$\omega_{\mathrm{LSPR}} = \sqrt{\frac{\omega \mathrm{p}^2}{(\varepsilon\infty+2\varepsilon\mathrm{m})} - \Gamma^2} \tag{6.4}$$

where ε_∞ indicates the high-frequency dielectric constant of the material, ε_{m} suggests the dielectric constant of the medium surrounding the nanocrystals and Γ represents the damping constant. As ε_∞ is a distinctive feature that cannot vary with the increase of doping and ε_{m} is determined by the surrounding media. It can be obtained that the variables with a significant impact on the LSPR frequency are the damping constant Γ and the bulk plasma frequency ω_{P} which is described as eq (6.5)

$$\omega \mathrm{p}^2 = \frac{ne^2}{\varepsilon 0 m^*} \tag{6.5}$$

where n represents the free carrier density, e indicates the electronic charge, ε_0 presents the permittivity and m^* is the effective mass of the electron. As e and ε_0 are constants for a certain kind of nanocrystals, the spectral selectivity of LSPR depends on n and Γ. In extrinsically doped nanocrystals, the electrostatic interactions between the dopant ions and the electrons can significantly affect scattering level, but Drude model does not premeditate the effect of dopant ions scattering, which provides inevitable scattering in doped nanocrystals. Consequently, an extended Drude model was presented where the damping constant Γ is displaced using a frequency-dependent $\Gamma(\omega)$ by the following empirical eq (6.6) to describe the scattering degree.

$$\Gamma(\omega) = \Gamma_{\mathrm{L}} - \frac{\Gamma\mathrm{L} - \Gamma\mathrm{H}}{\pi}\left[\tan^{-1}\left(\frac{\omega - \Gamma\mathrm{X}}{\Gamma\mathrm{W}}\right) + \frac{\pi}{2}\right] \tag{6.6}$$

where Γ_{L} and Γ_{H} represent the low-frequency and high-frequency damping constants respectively, Γ_{X} indicates the crossover frequency ranging from the low to high frequency domain. Γ_{W} denotes the width of the crossover region. Thus, it is found that Γ_{L} qualitatively indicates the scattering extent of dopants ions. To achieve the reductant scattering extent, Γ_{L} should be minimized as much as possible. Under the influence of a DC electric field, the electrostatic potential at low frequencies Γ_{L} was reported to be equivalent to the carriers motion property [163]. It is noted that carrier mobility under DC electric field is no frequency-dependence. Consequently, $\Gamma_{(0)}$ can be utilized to describe the scattering extent of dopant ions using eq (6.7)

$$\mu_{\mathrm{opt}} = \frac{e}{m^{*}\Gamma(0)} \tag{6.7}$$

It can be seen that carrier mobility μ_{opt} plays a significant effect on FWHM and further determine LSPR response. In addition, the electrons transferred between two adjacent nonequivalent W ions are provided by dopant ions, so free carrier density also exerts influence on small polaron transfer. As a result, the impact of free carrier density and carrier mobility on optical performance needs to be investigated further.

Table 6.4 The free carrier density and carrier mobility of as-prepared Li, F-codoped Cs_xWO_3 samples.

Sample	Free carrier density (cm^{-3})	Carrier mobility ($cm^2\ V^{-1}\ s^{-1}$)
CWO	5.83×10^{14}	16.62
0.2-LiFCWO	8.77×10^{14}	15.23
0.4-LiFCWO	11.94×10^{14}	14.54
0.6-LiFCWO	11.21×10^{14}	11.81
0.8-LiFCWO	10.63×10^{14}	10.14

To compare the electrical properties, the hall-effect measurements were conducted to further explain the optical performance of doped nanocrystals. LiF has a significant impact on free carrier density and carrier mobility, as shown in Table 6.4. When the concentration of LiF increased, the carrier mobility of the corresponding sample illustrated a decreasing trend. Notably, when the LiF/W molar ratio was larger than 0.4 in the precursor, the carrier mobility of the corresponding nanocrystals demonstrated a more sharper decreasing tendency than the that of the samples with LiF/W molar ratio below 0.4. The main scattering mechanism can be attributed to impurity doping. The higher LiF/W molar ratio in the precursor can cause the stronger scattering introduced by the dopant ions. On the other hand, the free carrier density firstly showed an increasing trend with the increase of LiF and reached 11.94×10^{14} cm^{-3} for 0.4-LiFCWO. After that, the free carrier density of 0.6-LiFCWO and 0.8-LiFCWO slightly decreased to 11.21×10^{14} cm^{-3} and 10.63×10^{14} cm^{-3} respectively. Specifically, in the wavelength range of 780 nm to 2500 nm, 0.4-LiFCWO had the best absorption coefficient. which can be attributed to its high free carrier density shown in Table 2. High free carrier density can improve both of LSPR and small polaron transfer. Although the carrier mobility of 0.4-LiFCWO was lower than that of CWO, the absorption coefficient of 0.4-LiFCWO still demonstrated best optical performance. This is because the carrier mobility of 0.4-LiFCWO has not decreased too much and is close to the undoped sample. Besides, it can be obtained that the free carrier density has a dominant impact to determine the absorption coefficient than the carrier mobility.

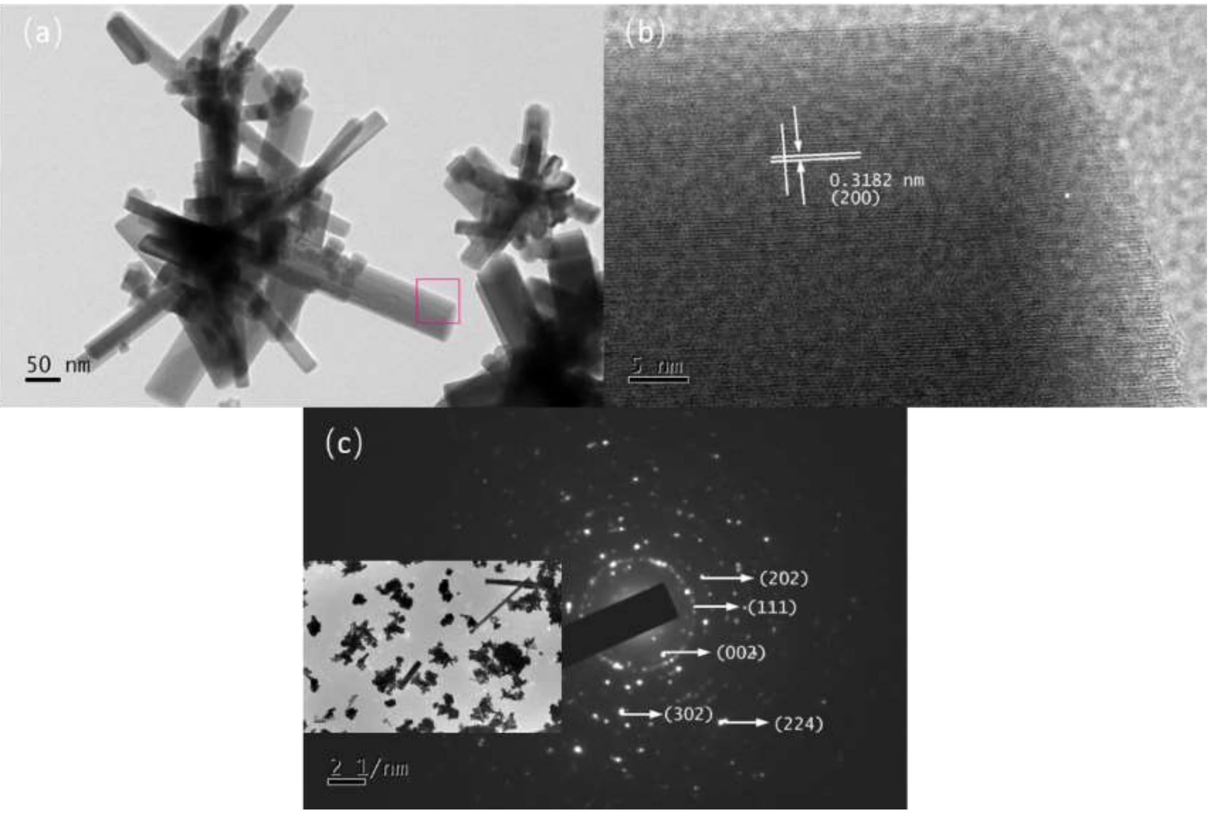

Figure 6.12 (a) TEM image, (b) HR-TEM image, (c) SAED pattern of 0.4-LiFCWO.

The TEM image, HR-TEM image, and SAED pattern of 0.4-LiFCWO were all determined using transmission electron microscopy. As illustrated in Figure 6.12a, the nanocrystals show rectangle-like shape with a certain extent of agglomeration. The lattice spacing of 0.3182 nm, which corresponds to the plane of Figure 6.12b, is shown (200). The SAED pattern in Figure 6.12c confirmed the hexagonal structure of 0.4LiCWO.

Several factors affect the electrical properties of different transparent conductive oxides. They are impurity doping, the distribution of the doped element, size and shape of the nanocrystals, respectively. The LSPR effect of cadmium oxide (CdO) was effectively enhanced by F, In co-doping [152, 164]. Indium fluorine (InF_3) was added into the precursor solution during the synthetic process. The free carrier density of the doped nanocrystals is higher than that of the nanocrystals without the doped elements. Moreover, it has been reported that the distribution of dopant can effectively influence the LSPR effect of Sn-doped indium oxide (ITO) [84]. The nanocrystals with core/shell structure were prepared by high temperature injection solvothermal method. Because of the dopant-free region at the surface, which reduces surface and impurity scattering while increasing activation, ITO/In2O3 core/shell nanocrystals have the lowest damping. Furthermore, the dependence of LSPR effect of ITO nanocrystals on nanocrystal size was also investigated [163]. ITO nanocrystals with a particle size of 6 nm to 20 nm are precisely synthesized. The LSPR peak energy for ITO NCs is found to blue shift as the diameter of the NC increases. However, the absorption coefficient increases with increasing nanocrystal size before saturating for sizes greater than 14 nm in diameter, implying the presence of size-dependent optical performance and a change limitation in ITO nanocrystals. Finally, two types of shapes of Cs_xWO_3 nanocrystals, rod-like shape and truncated cubes, have been synthesized by using different ratio of oleylamine to oleic acid [71]. The rod-like nanocrystals demonstrated stronger absorption peak than the nanocrystals with truncated cube shape, which can be attributed to the LSPR effect and small polaron transfer. The detailed mechanisms on how the shape influences the optical performance have not been further investigated. Therefore, the improvement of optical properties of Cs_xWO_3 nanocrystals lies in how to enhance their LSPR effect and small polaron transfer. In terms of the LSPR effect, free carrier density and carrier mobility are two main factors. In this work, Li,F codoped Cs_xWO_3 nanocrystals show a rod-like shape after the addition of LiF. It can be obtained that the addition of LiF can induce the morphology transformation during the synthetic process. It is expected that both of the morphology change and LiF codoping improve the optical performance. In addition, the addition of LiF may play a dominant role to determine the free carrier density. In order to investigate the effect of shape on optical performance, the nanocrystals should be prepared with the same doping level and element composition. To achieve the goals of scalable production and industrial application, a facile and cost-effective synthetic method should be developed. Thus, the addition the LiF provides a suitable way to improve their optical properties.

6.4 Conclusions

In this chapter, Li, F-codoped Cs_xWO_3 nanocrystals have been successfully synthesized to enhance the spectral tunability of LSPR and small polaron transfer by a controllable one-pot method. The phase components, element compositions, valence state of W ions and microstructure of the as-prepared nanocrystals were systematically examined. Furthermore, the Beer-Lambert Law was used to calculate the absorption coefficient spectra of the samples, and the Hall effect was used to determine the free carrier density and carrier mobility. This study is the first case in the literature interpreting the prospective connection between free carrier density/carrier mobility and optical performance in Li, F-codoped Cs_xWO_3 nanocrystals, indicating that aliovalent doping is a viable method for improving spectral tunability. The results indicate that the free carrier density plays a dominant impact to determine the absorption coefficient than the carrier mobility. When the LiF/W molar ratio is 0.4, the corresponding nanocrystals demonstrated best absorption property in the wavelength of near-infrared radiation. This doping strategy provides promising potential to improve the spectral tunability for the practical application of energy-efficient windows.

Chapter 7

Investigation on oxygen defect-induced small polaron transfer for controlling the near-infrared absorption coefficient of cesium tungsten bronze nanocrystals

7.1 Introduction

Small polaron transfer, in addition to LSPR, plays an important role in improving the optical performance of Cs_xWO_3 nanocrystals. Cs_xWO_3 nanocrystals with more oxygen defects were successfully synthesized using a one-pot method in this chapter, which increases the spectral tunability of small polaron transfer. The effects of oleylamine on the phase composition, valence state distribution of W, optical properties and microstructure of the as-prepared products have been investigated. The detailed mechanism for improving the near-infrared shielding performance has been discussed. Besides, the absorption coefficient spectra of the samples were calculated by the Beer-Lambert Law.

7.2 Experimental study

7.2.1 Materials

The reagents are of analytical grade and utilized as received without further treatment. Ammonium metatungstate hydrate (AMT, $(NH_4)_6H_2W_{12}O_{40} \cdot aH_2O$), cesium carbonate ($Cs_2CO_3$), tartaric acid (TA, $C_4H_6O_6$), deionized water (H_2O), anhydrous ethanol (C_2H_5OH), oleylamine (OLA) and polyvinyl alcohol (PVA) were purchased from Macklin.

7.2.2 Synthesis of Cs_xWO_3 nanocrystals with oxygen defects and fabrication of composite film

The Cs_xWO_3 nanocrystals with oxygen defects were prepared by controllable one-pot method using AMT as W source and Cs_2CO_3 as Cs origin respectively. First, a certain amount of AMT was dissolved in ethanol with 1mol/L tartaric acid, and then 10 ml of Cs_2CO_3 and OLA were added to the AMT solution with a Cs/W molar ratio of 0.33. The mixed solution had a total volume of 70 ml. The solution was then placed in a PTFE autoclave with a 50 mL interval volume and the solvothermal reaction was carried out in a drying oven at 240 °C. The Cs_xWO_3 nanocrystals synthesized with OLA were labeled as CWO-OLA. The nanocrystals prepared without oleylamine were marked as CWO. The dispersion of the CWO-OLA was obtained by a facile blending process. PVA powder was applied as the film-formation additive. Typical fabrication procedures of the spectrally selective coating were carried out in the following way. Initially, 4 g PVA powder was melt in deionized water under 85 ℃ water bath to form a homogeneous PVA solution. Afterwards, the as-synthesized nanocrystals of a certain amount were blended with the above PVA solution by strong stirring for 4 h. The obtained dispersion was then deposited on the glass surface to form the spectrally selective coating.

7.2.3 Characterization

X-ray diffraction (XRD) with Cu K radiation was used to determine the phase components of the CWO-OLA nanocrystals. Transmission electron microscopy (TEM) with an energy dispersive spectrum (EDS) attachment was used to examine the nanocrystals' microstructure. X-ray photoelectron spectroscopy was used to investigate the chemical components and binding energies of W 4f (XPS). A spectrophotometer (UH 4150) with a 0.5 mm pathlength cuvette was used to measure the absorbance spectra of the as-synthesized nanocrystals. The unpaired electrons originated form oxygen defects were detected by electron spin resonance (ESR) spectrometer. Raman spectra of the as-prepared nanocrystals were measured under 532 nm laser of 10 mW with 1 cm^{-1} spectral resolution.

7.3 Results and discussion

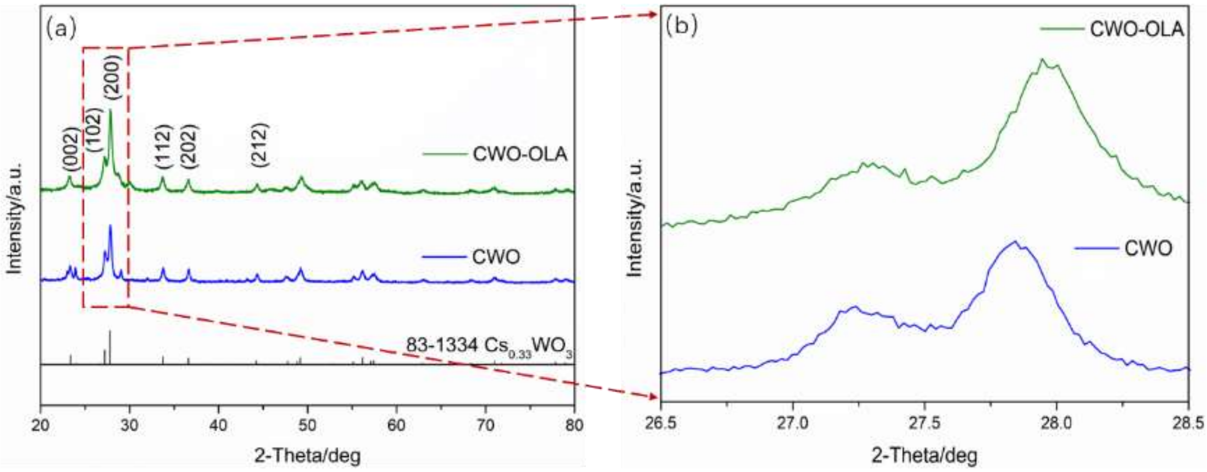

Figure 7.1 (a) XRD patterns, (b) high-resolution patterns corresponding to crystal plane (102) and (200) of CWO and CWP-OLA.

Figure 7.1 presents the XRD patterns of CWO and CWO-OLA and their high-resolution patterns corresponding to crystal plane (102) and (200). Both as-synthesized samples showed pure hexagonal cesium tungsten bronze phase (JCPDS NO. 83-1334) without impurity peaks, as shown in Figure 7.1a, indicating that the addition of oleylamine does not prevent the synthesis of nanocrystals with hexagonal crystal system. In Figure 7.1b, the peak intensity ratio of (200) plane relative to (102) plane for CWO-OLA are higher than the standard level for the reported pattern, revealing that the preferential growth of the CWO-OLA may be along the *a*-axe. Besides, the diffraction peak of (002) plane for CWO-OLA slightly shifted to a higher angle compared with CWO, which means that induces lattice distortions. According to the Bragg equation, this can be explained as follows:

$$2d\sin\theta = n\lambda \tag{7.1}$$

where d stands for crystal interplanar spacing, θ represents incident angle, λ denotes incident light wavelength, and n stands for reflection order. Because $n\lambda$ is a constant, increasing it implies a decrease in crystal interplanar spacing.

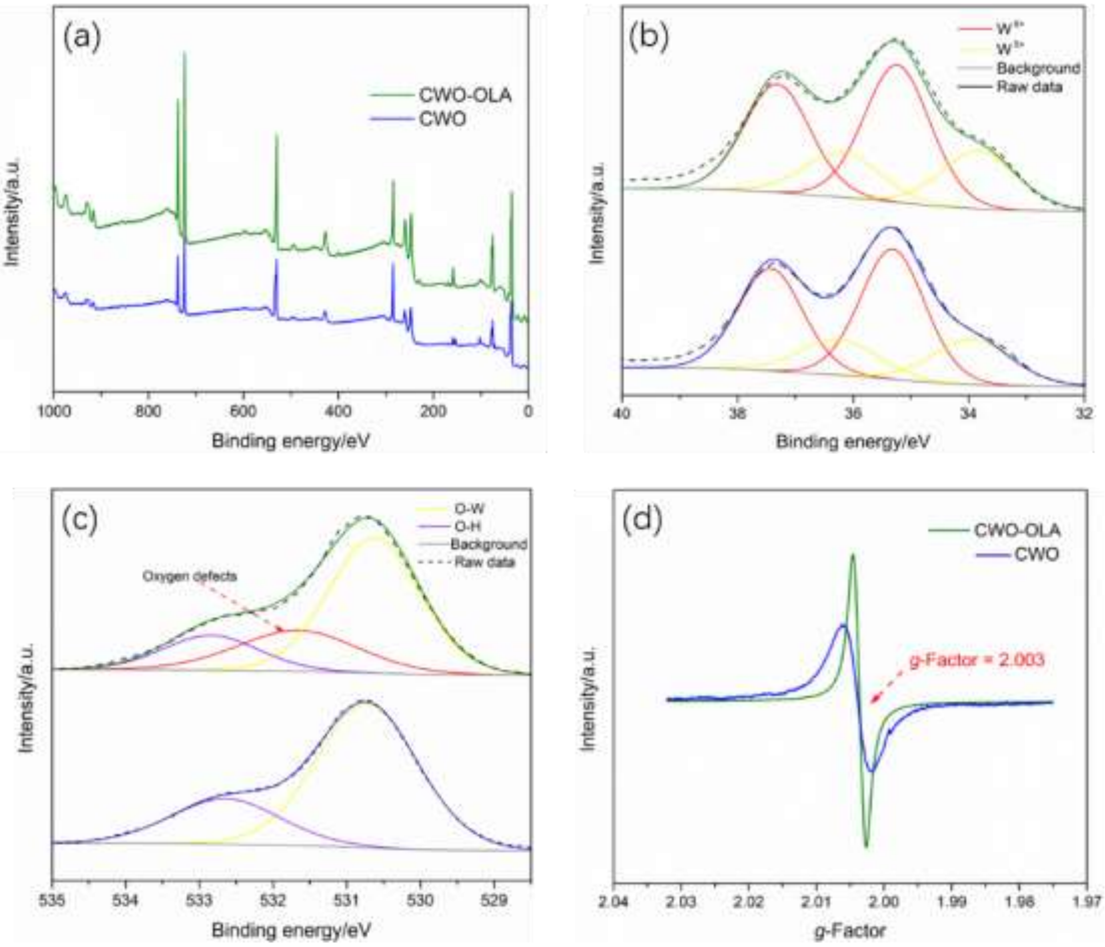

Figure 7.2 (a) XPS survey spectra, (b) W 4f core-level spectra, (c) O 1s core-level spectra, (d) ESR spectra of CWO and CWO-OLA.

XPS was used to determine the chemical composition and W valence state. The survey spectra of CWO and CWO-OLA are shown in Figure 7.2a. All the spectra confirm the presence of Cs, W and O elements. The W 4f core-level spectra of CWO and CWO-OLA are shown in

Figure 7.2b. W 4f 5/2 and W 4f 7/2 are two spin-orbital peaks that can be fitted to the W 4f curve. W^{5+} and W^{6+} are responsible for the spin-orbital peaks at 34.2 eV/ 36.7 eV and 35.8 eV/37.9 eV, respectively. It can be seen that CWO-OLA exhibits a higher ratio of W^{5+}/W than that of CWO, which can be ascribed to the electrons contributed by oxygen defects. The increase of W^{5+} generation is caused by addition of oleylamine in the synthetic process, which plays an active influence on the NIR shielding performance based on LSPR [37]. As shown in Figure 7.2c, three peaks can be seen from the fitting curve of O 1s for CWO-OLA compared with CWO. The three peaks are located at 533.1 eV, 531.6 eV and 530.5 eV respectively, and the fitting peak of 631.6 eV is induced by oxygen defects which is consistent with the reported values of oxygen defects. The fitting peak of 533.1 eV and 530.5 eV is corresponding to O-H and O-W chemical bond respectively. To further verify the presence of oxygen defects, ESR test was conducted to detect the unpaired electron from oxygen vacancy. It has been reported that the unpaired electrons derived from oxygen defects presented a signal at $g = 2.003$. As shown in Figure 7.2d, CWO-OLA demonstrated a symmetric signal at around $g = 2.003$ and stronger relative peak intensity compared with CWO, which indicates that many oxygen defects exists in the nanocrystals.

Table 7.1 The molar ratio of Cs/W and O/W in nanocrystal samples measured by XPS

Sample	Cs/W molar ratio	O/W molar ratio
CWO	0.31	2.95
CWO-OLA	0.32	2.86

The molar ratios of Cs/W and O/W in the samples were measured using the XPS technique to further investigate the effect of oleylamine on the chemical composition of the as-prepared samples. As listed in Table 1, both of the measured Cs/W molar ratio attained, which was close to theoretical Cs/W value of 0.33. Meanwhile, the measured O/W content of CWO and CWO-OLA was 2.95 and 2.86 respectively, which also confirms the existence of oxygen defects.

The Beer-Lambert Law can be described as following eq (7.2):

$$A = \frac{N\sigma L}{\log(10)} \tag{7.2}$$

Where A represents the measured absorbance of the dilute nanocrystal dispersion and is expressed in log (10) scale, N indicates the number density of the nanocrystals (M, mol/L), and L (mm) stands for path length through the cuvette. Thus, the absorption coefficient σ (M^{-1} mm^{-1}) of the nanocrystals can be calculated by the above equation using the measured absorbance of the dispersion with known molar concentration and the path length [66, 78, 84, 150, 152, 165-168].

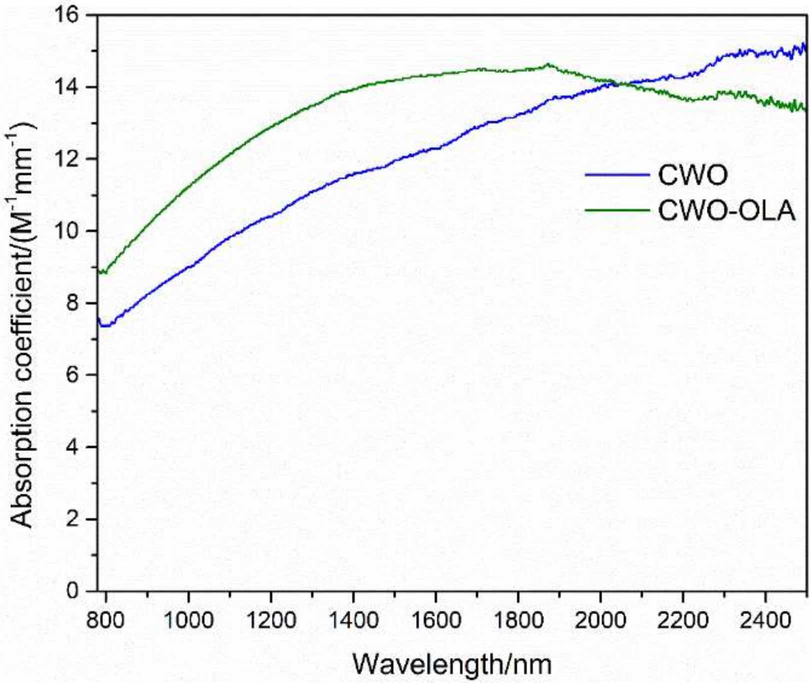

Figure 7.3 The absorption coefficient spectra of CWO and CWO-OLA.

To examine the effect of oleylamine on the absorption coefficient of the as-prepared nanocrystals, the absorbance of the dilute dispersion containing the as-prepared nanocrystals was measured. Figure 7.3 presents the calculated absorption coefficient spectra of the as-synthesized CWO and CWO-OLA nanocrystals. Compared with CWO, a significant increase of the absorption coefficient can be observed for CWO-OLA in the wavelength range from 800 nm to 1800 nm. The results indicate that the addition of oleylamine in the synthetic process can enhance the absorption performance of nanocrystals, which is discussed in detail in the following content.

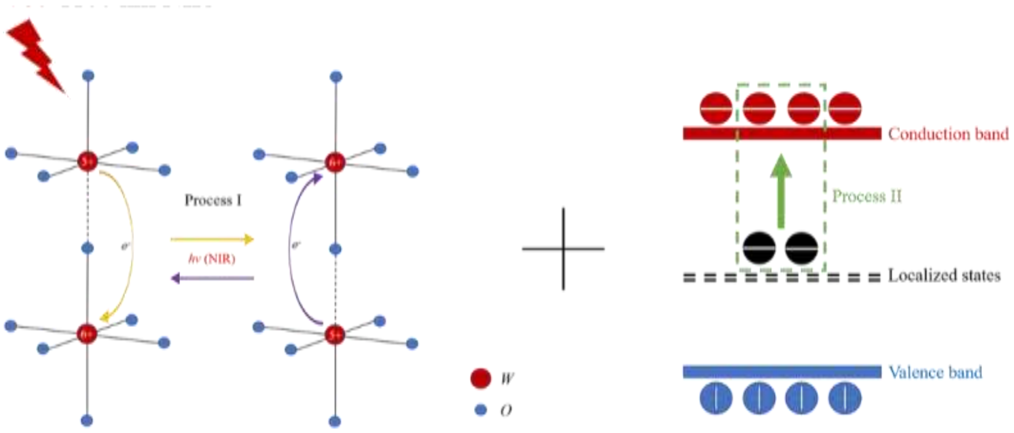

Figure 7.4 The schematic diagram of small polaron transfer under 780-1100 nm NIR.

According to the above results, the spectrally selective mechanism of Cs_xWO_3 nanocrystals is presented in Figure 7.4. Small polaron transfer mainly absorbs the 780-1100nm NIR radiation and consists of two processes [42]. When surplus electrons polarize their ambient lattice, polarons are formed and defined as the composite of lattice distortion and accompanying free electrons. The polarons absorb NIR light by hopping between two adjacent nonequivalent W ions. The polaron transition process is as follows:

$$\text{Process I: } h\nu + W^{5+}(a) + W^{6+}(b) \rightarrow W^{6+}(a) + W^{5+}(b) + E_{phonon} \tag{7.3}$$

where E_{phonon} represents single phonon energy.

In addition, there are some electrons in localized states lower than the conduction band of nanoparticles. As shown in Process II, the electrons in localized states would transfer from localized state to conduction band led by absorbing suitable NIR energy. It has been reported that electrons derived from oxygen defects cause a smaller dimensional change than electrons derived from Cs doping, indicating that electrons derived from oxygen defects should be localized in the W–5d orbital [66]. The destabilization of the pseudo Jahn-Teller distortion is regarded as a structural change (PJT distortion). W–5*d*/O–2*p* hybridization may experience an additional orbital overlap as a result of PJT stabilization. To put it another way, W–5*d*'s excess electrons should strongly hybridize with O–2*p* to form a short W^{5+}=O bond. Thus, the localized electrons contributed by oxygen defects are considered to locate in the lower part of the conduction band and can absorb near-infrared radiation to the upper level through small polaron transfer.

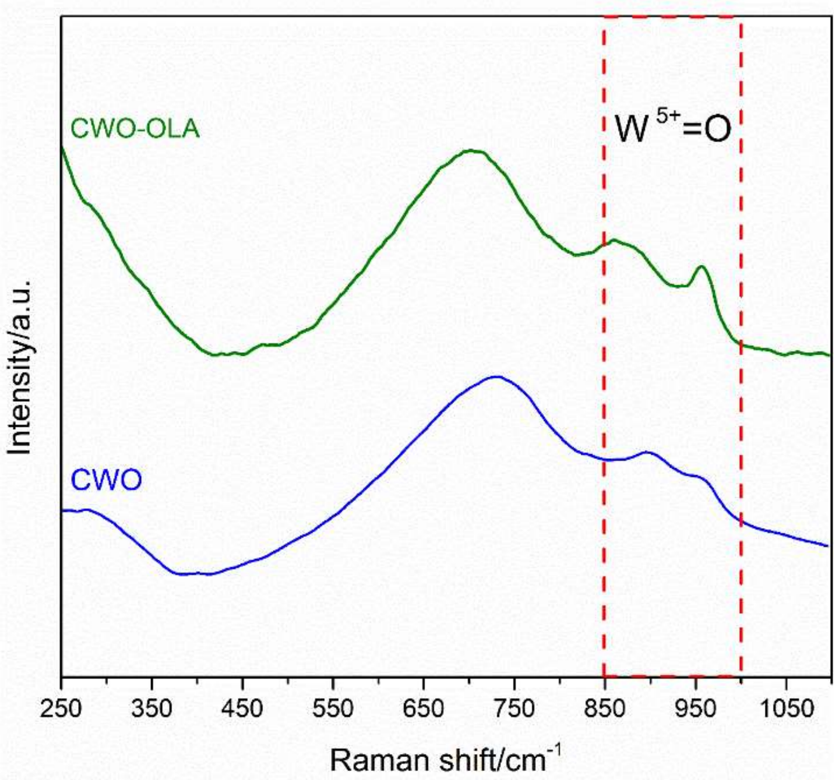

Figure 7.5 Raman spectra of CWO and CWO-OLA

To further verify the existence of oxygen defects, Figure 7.5 presents Raman spectra of CWO and CWO-OLA. According to the previous studies, the characteristic peaks were mainly distributed in three regions [66, 169]. The bending mode and the stretching mode of O-W-O bends were attributed to the peaks at intervals of 150-360 cm-^{1} and 500-850 cm^{-1}, respectively. Peaks in the range of 850-1000 cm^{-1} were attributed to the W^{+5}=O bands stretching mode. The presence of oxygen defects in CWO-OLA can be confirmed by the presence of obvious peaks in the range of 850-1000 cm^{-1}. As illustrated in Figure 7.5, the peak intensity ratio of W^{+5}=O peak relative to O-W-O stretching peak in CWO-OLA is higher than that in CWO. The results indicate that a higher content of W^{+5}=O bands are in CWO-OLA, which can contribute more electrons for small polaron transfer to enhance the absorption coefficient of nanocrystals.

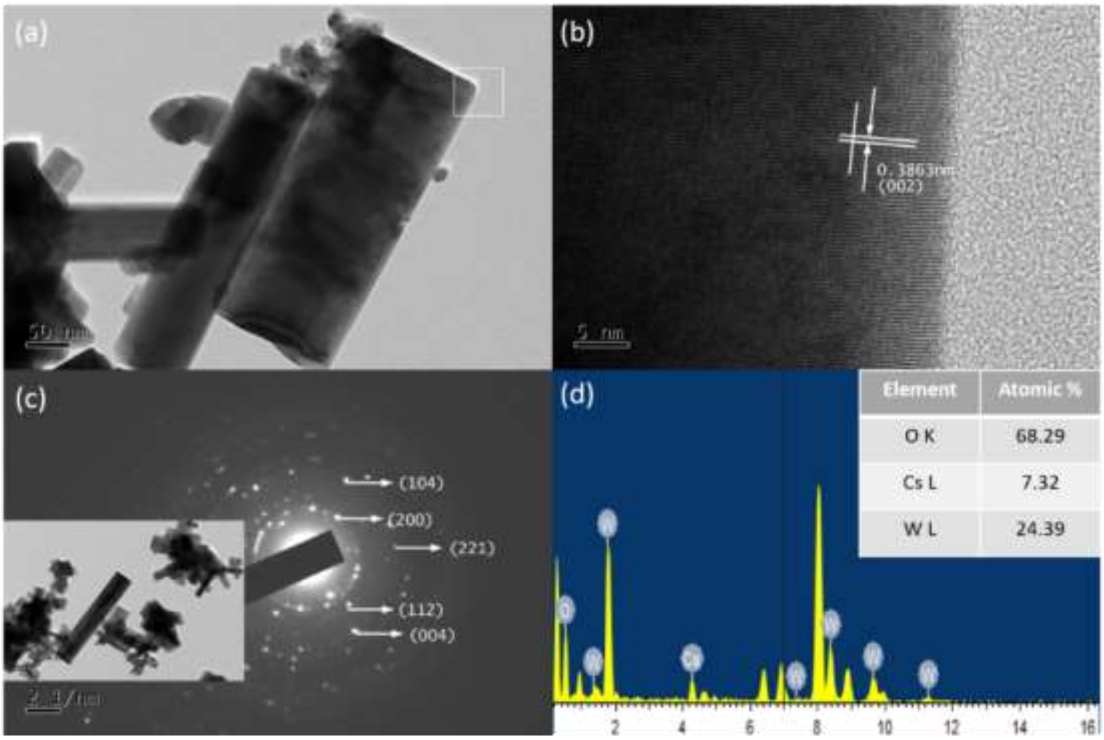

Figure 7.6 (a) TEM image, (b) HR-TEM image, (c) SAED pattern and (d) EDS spectrum of CWO-OLA

The TEM image, HR-TEM image, SAED pattern, and EDS pattern of CWO-OLA were all determined using transmission electron microscopy. As illustrated in Figure 7.6a, the nanocrystals show rod-like shape with a certain extent of agglomeration. The lattice spacing of

0.3863 nm corresponds to the plane of Figure 7.6b (002). The SAED pattern in Figure 7.6c confirmed the hexagonal structure of CWO-OLA. Figure 7.6d presents element composition and indicates the presence of Cs, W and O element. The calculated Cs/W molar ratio is 0.3001, which is quite close to the upper limit of 0.33 for Cs-HTBs. Besides, the calculated O/W molar ratio is 2.79, which is also close to the value measured by XPS.

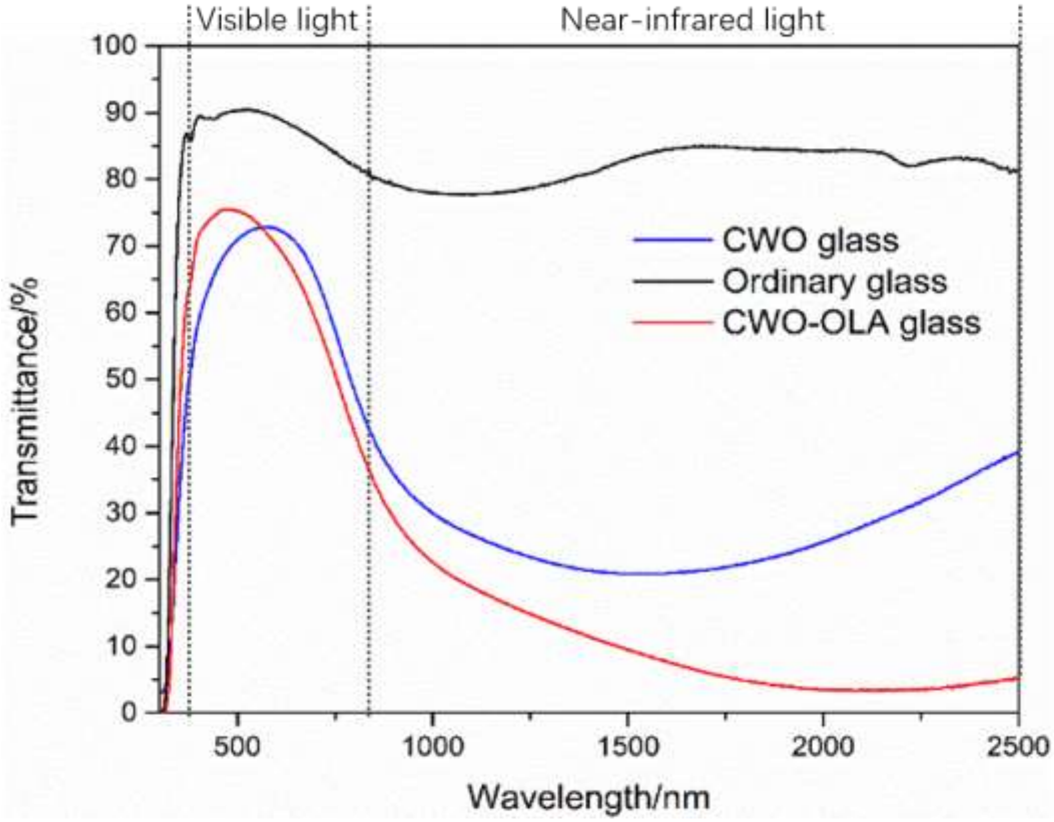

Figure 7.7 The transmittance spectra of CWO glass CWO-OLA glass and ordinary glass.

To fabricate the CWO-OLA/PVA composite film, the as-synthesized CWO-OLA were mixed with PVA solution. Figure 7.7 shows the spectra of ordinary glass without any coatings, the glass sample fabricated by the CWO-OLA/PVA dispersion and the glass coated by CWO/PVA dispersion. To evaluate the spectral selectivity of the glazing sample, four parameters were proposed, involving T_{Vis}, T_{NIR}, T_{lum}, and T_{sol} [95, 144, 170]. The corresponding values can be calculated by the following equations:

$$T_{\mathrm{vis}} = \frac{\int_{380}^{780} T\,(\lambda) d(\lambda)}{(780-380)\times 100} \times 100\% \tag{7.4}$$

$$T_{\mathrm{NIR}} = \frac{\int_{780}^{2500} T(\lambda) d(\lambda)}{(2500-780)\times 100} \times 100\% \tag{7.5}$$

$$T_{lum} = \frac{\int_{380}^{780} \varphi lum(\lambda) T(\lambda) d(\lambda)}{\int_{380}^{780} \varphi lum(\lambda) d(\lambda)} \times 100\% \tag{7.6}$$

$$T_{sol} = \frac{\int_{300}^{2500} \varphi sol(\lambda) T(\lambda) d(\lambda)}{\int_{300}^{2500} \varphi sol(\lambda) d(\lambda)} \times 100\% \tag{7.7}$$

Where $T(\lambda)$ denotes the measured transmittance spectra within a given range, φ_{lum} denotes the standard luminous efficiency function for human eyes' photonic vision, and φ_{sol} denotes the solar radiation spectrum for air mass 1.5. Above calculated value of CWO-OLA glass is 67.11 %, 11.21 %, 72.59 % and 49.12 %, respectively. The glazing sample with the composite film exhibits excellent visible light transmittance and near-infrared shielding performance. The glazing sample with the composite coating exhibits excellent spectral selectivity when compared to ordinary glass.

7.4 Conclusions

In this study, Cs_xWO_3 nanocrystals have been successfully synthesized to enhance the spectral tunability of small polaron transfer by a controllable one-pot method. The phase components, element compositions, valence state of W ions and microstructure of the as-prepared nanocrystals were systematically examined. Moreover, the absorption coefficient spectra of the samples were calculated by the Beer-Lambert Law. This study is the first case in the literature interpreting the prospective connection between oxygen defects and optical performance in Cs_xWO_3 nanocrystals, indicating that the addition of oleylamine in the precursor is an effective way to enhance the absorption coefficient. This strategy provides promising potential to improve the small polaron transfer of Cs_xWO_3 nanocrystals for the practical application of energy-efficient windows.

Chapter 8

Spraying fabrication of Sb-doped SnO_2/Li, F-codoped Cs_xWO_3/UV-curable WPUA in-situ polymerization coating for energy-efficient windows

8.1 Introduction

Glass functionalization is usually realized by a thin film layer based on spectrally selective materials applied on the glazing surface thus changing the way the glass interacting with the solar radiation and surrounding media. So far, the spectrally selective materials can be classified into three main types, namely metal, metal oxides and metalloid. The most commonly used metal for spectral selectivity is silver. Silver-based low-emissivity (low-E) glazing is composed of two glass panes for preventing the exposure of the low-E coating which is usually fabricated by magnetron sputtering requiring expensive equipment and complex operating parameters [13, 14]. This type energy-saving glass is not favorable for retrofitting the installed single-glazed windows due to its double structure. Metal oxides used for solar heat-shielding mainly include tin-doped indium oxide (ITO) [111, 131, 171], aluminum-doped zinc oxide (AZO) [10, 124, 127] and Sb-doped tin oxide (ATO) [22, 26, 55, 133, 172]. Among them, ITO and ATO can only block the wavelength higher than 1500nm, which might cause a lower shielding performance in the wavelength ranging from 780nm to 1500nm [29]. Also, the raw material (indium) for preparing ITO is expensive. It is reported that the method for preparing AZO is not efficient and it shows a higher transmittance in the near-infrared region [173]. As for metalloid, LaB_6, the most common rare-earth hexaborides, can effectively shield the near-infrared radiation. Furthermore, the spectrally selective coating based on the nanoparticles are usually prepared via spinning and rolling method [44, 48, 174]. However, spinning coating is a lab-scale method and rolling coating is not conductive to obtain an even coating surface. Simple and accessible deposition methods are important not only for academic study but also for industrial use.

The waterborne polyurethane acrylate, also known as WPUA, is an improved type of WPU. The introduction of acrylate groups can lead to the enhancement in the mechanical durability compared with WPU [54, 61, 133, 172, 175]. In previous studies, the transparent heat-insulation coating was prepared by physically blending the functional nanoparticles in the pre-synthesized dispersion. Nevertheless, the appearance of the heat-insulation coating was not clear enough and translucent, which was attributed to the uneven distribution of the nanoparticles in the coating matrix by physical blending method and hindered the practical application in the field of energy-efficient windows.

In this chapter, spraying fabrication of Sb-doped SnO_2/Li, F-codoped Cs_xWO_3/UV-curable WPUA in-situ polymerization coating for energy-efficient windows was proposed. Low-agglomerated ATO nanoparticles and Li, F-codoped Cs_xWO_3 nanoparticles were prepared based on our previous research. It is believed that the spraying fabrication of spectrally selective coating with improved near-infrared shielding performance has promising applied prospects for energy-efficient glazing.

8.2. Experimental study

8.2.1 Materials

The following reagents are of analytical grade and utilized as received without further treatment. Tin chloride pentahydrate ($SnCl_4 \cdot 5H_2O$), antimony chloride ($SbCl_3$), ammonium hydroxide solution ($NH_3 \cdot H_2O$ 25%–28%), polyvinyl alcohol (PVA), absolute ethanol (C_2H_5OH) and deionized water (H_2O).Ammonium metatungstate hydrate (AMT, $(NH_4)_6H_2W_{12}O_{40} \bullet aH_2O$), cesium carbonate ($Cs_2CO_3$), tartaric acid (TA, $C_4H_6O_6$), deionized water (H_2O), anhydrous ethanol (C_2H_5OH), lithium fluoride (LiF) oleylamine, polyisophthalic diglycol (PIDG), dimethylol propionic acid (DMPA), isophorone diisocyanate (IPDI), butanediol (BDO), ethylenediamine (EDA), methanol, 3-methacryloxypropyltrimethoxysilane (MPS), propyl alcohol and pentaerythritol triacrylate (PETA) were purchased from purchased from Macklin.

8.2.2 Synthesis of Li, F-codoped Cs_xWO_3 nanocrystals

The Li-doped Cs_xWO_3 nanocrystals were prepared by controllable one-pot method using AMT as W source, Cs_2CO_3 as Cs origin and LiF as Li, F origin respectively. First, a small amount of AMT was dissolved in ethanol with 1mol/L tartaric acid, and then Cs_2CO_3 and LiF were added to the AMT solution with a Cs/W molar ratio of 0.33. The total volume of the mixed solution was 70 ml, with 15 ml of oleylamine. The solution was then transferred to a Teflon-lined autoclave with a 200 ml interval volume, and the liquid phase reaction was carried out. Centrifugation was used to collect the products, which were then washed three times with anhydrous ethanol before being vacuum dried at 60°C. The Li, F-codoped Cs_xWO_3 nanocrystals synthesized with the LiF/W molar ratio of 0.4.

8.2.3 Synthesis of ATO nanocrystals

The ATO nanocrystals were prepared by co-precipitation method using $SnCl_4 \cdot 5H_2O$ as Sn source and $SbCl_3$ as Sb source respectively. First, a certain amount of $SnCl_4 \cdot 5H_2O$ was added into the deionized water, then $SbCl_3$ was introduced into the aqueous solution of $SnCl_4 \cdot 5H_2O$ with a Sb/(Sb + Sn) molar ratio of 10%. Diluted $NH_3 \cdot H_2O$, the precipitant, was dropped into the precursor solution at a constant speed to form the hydroxide precipitation. During this process, the titration endpoint of pH value reached 6. The resultant solution was kept at 60 °C for 1 hour and then centrifugated three times with absolute ethanol. The obtained precipitation was dried at 80 °C for 2 hours and then polished into powders. The as-prepared powders were subsequently placed a tube furnace and sintered at 1000 °C for 4 hours to get the desired samples.

8.2.4 The surface modification of functional nanoparticles

The surface modification of the as-prepared ATO/Li, F-codoped Cs_xWO_3 by MPS were conducted as follows. Firstly, a certain amount of the nanoparticles was blended with 50 ml methanol and 1 g MPS, and then the mixture was kept at 75 °C for 10 hours. After that, the resultant mixture was transferred to a rotary evaporator to remove the excessive MPS. Finally, the modified nanoparticle dispersion was obtained for being further processed.

8.2.5 The synthesis of WPUA emulsion

The synthesis of WPUA was conducted through the following steps. 30 g PIDG, 15 g IDPI and 0.1 g DBTDL were added into a flask with a mechanical stirrer and thermometer. The reaction was heated at 85 °C for 1 hour. Then, 2.35 g DMPA was added in the reaction precursor at 85 °C for 2 hours. Subsequently, 0.4 g BDO and 8.5 g PETA was introduced into the flask for 1 hour at 75 °C. When the precursor temperature was cooled down to the room temperature, 1.8 g TEA was putted in the flask to balance the carboxylic group for 10 mins under stirring for 1 hour with addition of the modified nanoparticle dispersion drop wisely. Finally, the 3 wt% photo-initiator was added into the as-prepared emulsion to obtain the final product.

8.2.6 Spraying fabrication of spectrally selective coatings on glazing

Certain amount of as-synthesized Li, F-codoped Cs_xWO_3 and ATO nanoparticles were added into the above WPUA emulsion with 1:1 mass ratio of Li, F-codoped Cs_xWO_3 and ATO. The obtained dispersion was then processed by ultrasonic treatment. Finally, the ATO/Li, F-codoped Cs_xWO_3/UV-curable WPUA emulsion was used to fabricate the spectrally selective coating on the clear glass by spraying method.

8.2.7 Characterization

The phase compositions of nanoparticles were examined by X-ray diffraction (XRD) with Cu Kα radiation. The morphologies and microstructures of the nanoparticles were obtained by transmission electron microscopy (TEM) with an energy dispersive spectrum (EDS) attachment. The chemical composition and binding energies of W 4f were obtained by X-ray photoelectron spectroscopy (XPS). The optical performance of the prepared samples was measured by an UV-vis-NIR spectrophotometer.

8.2.8 Near-infrared shielding test under simulated radiation

A box device was conducted to assess the heat-shielding property of the different glazing samples. The top facet of device was equipped with the different glazing. The light was provided by a 500 W infrared lamp with 20 cm over the coated glass. The thermocouple should avoid being directly irradiated by the infrared lamp. The temperature recorded by thermocouple represented the air temperature inside the sealed box device.

8.2.9 Model house field test

To evaluate the optical performance of the as-fabricated coating, a field experiment using the above model box was carried out in the summer of Hong Kong. One box was covered by the single glass with the as-fabricated composite coating, the other box was covered by ordinary glass without any functional coatings.

8.3 Results and discussion

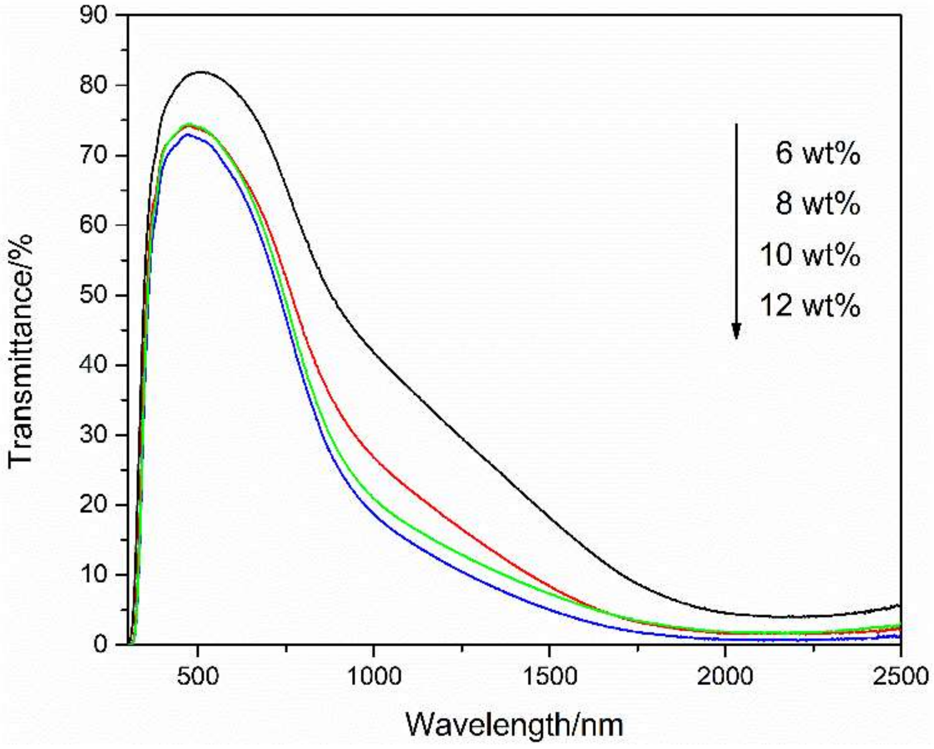

Figure 8.1 UV-Vis-NIR transmittance spectra of spectrally selective coatings prepared by dispersions with different solid content of the composite nanofiller.

Table 8.1 The optical parameters of the spectrally selective coatings with different solid content of composite nanofillers.

Solid content	T_{Vis} (%)	T_{NIR} (%)	K
6 wt%	76.31%	19.11%	6.03
8 wt%	71.65%	11.06%	6.47
10 wt%	70.76%	9.36%	7.56
12 wt%	68.81%	7.55%	9.11

To fabricate the spectrally selective coatings, the as-synthesized ATO and /LiF-codoped Cs_xWO_3 nanoparticles were combined with the same mass ratio as the composite nanofiller. Figure 8.1 presents the solar transmittance spectra of the coated glazing prepared by the dispersion with different nanofiller content of 6 wt%, 8 wt%, 10 wt% and 12 wt%. For the purpose of evaluating the optical properties of the coatings, three parameters, including T_{Vis} (average transmittance of visible light, 380-780 nm), T_{NIR} (average transmittance of near-infrared light, 780-2500 nm) and K (transparent heat-shieling index defined as $K = T_{\mathrm{Vis}} / T_{\mathrm{NIR}}$), were proposed [144, 170]. The corresponding values calculated by the fitting curve of transmittance spectra shown in Figure 8,1 are displayed in Table 8.1. It can be seen that the solid content of composite nanofiller plays a major role on improving the near-infrared blocking property. In general, higher K indicates better transparent heat-shielding performance of the coatings. As shown in Table 2, T_{NIR} declines with the increase of solid content, indicating higher near-infrared shielding ability. Although K is higher with the increase of solid content, T_{Vis} shows a decreasing trend. When the solid content attains to 12 wt%, T_{Vis} of the corresponding coating is below 70%, which is not conducive to visible transmittance. Therefore, a conclusion can be drawn that the spectrally selective coating with the solid content of 10 wt% displayed favorable transparent heat-shielding performance than the coatings with other solid contents.

Table S1 Optical properties comparison of various spectrally selective materials.

No.	Type	Materials	Fabrication technique	T_{Vis}(%)	T_{NIR}(%)	$K(T_{Vis}/T_{NIR})$	T_{lum}(%)	T_{sol}(%)	FOM(T_{lum}/T_{sol})	Refs
1	Metal	ZnS/Ag/ZnS	Sputtering	>80	< 20	-	-	-	-	[37]
2		NiO/Ag	Evaporation	-	-	-	68	44	1.55	[38]
3		MoO_3/Ag	Evaporation	-	-	-	71.6	47.4	1.51	[39]
4	Metal oxide	ITO	Dip coating	85	< 20 (above 1600 nm)	-	-	-	-	[40]
5			Solution casting	-	-	-	64.5	65.1	0.99	[41]
6		ATO	Suspension casting	-	-	-	90.83	62	1.47	[42]
7			Spin coating	80.15	23.31	3.44	-	-	-	[13]
8			Spray coating	77.24	19.54	3.95	-	-	-	[43]
9		Cs_xWO_3	Rolling coating	68.4	11.16	6.13	-	-	-	[44]
10			Rolling coating	69	14	4.93	-	-	-	[45]
11			Rolling coating	57.12	18.8	3.04	-	-	-	[46]
12			Rolling coating	73.26	23.31	3.14	-	-	-	[47]
13			Dispersion casting	-	-	-	70	43.4	1.61	[48]
14		Li, F-codoped Cs_xWO_3	Spray coating	68.75	9.16	7.51	73.36	44.59	1.65	This study

To evaluate the optical performance of the as-fabricated composite coating in this work, a comprehensive comparison with other types of spectrally selective materials, such as metal silver, tin-doped indium oxide (ITO) and antimony-doped tin oxide (ATO), was listed in Table 3 [37, 39, 41, 55, 61, 64, 74, 143, 176-180]. The optical properties and fabrication techniques were considered for the assessment of energy-saving performance. The ratio of T_{lum} to T_{sol} was defined as FOM (Figure of merit), and K indicates the ratio of T_{vis} to T_{NIR}. Thus, FOM and K are important factors to assess the spectrally selective ability of the samples. Among WO_3-based materials, the 0.4-LiFCWO/PVA composite film illustrates the highest values of FOM and K. Compared with silver-based Low-E coatings, the optical properties of the 0.4-LiFCWO/PVA composite film are still comparable, while the expensive and complex fabrication techniques can be replaced since the thin composite film is deposited on the window glazing by spraying fabrication. As for the spectrally selective coating prepared by ITO and ATO, their optical properties still have room for improvement because they can only effectively shield the near-infrared radiation higher than 1500nm. The spraying fabrication of the 0.4-LiFCWO/PVA composite coating provides superior optical performance, which is more appropriate for the retrofitting of existing windows.

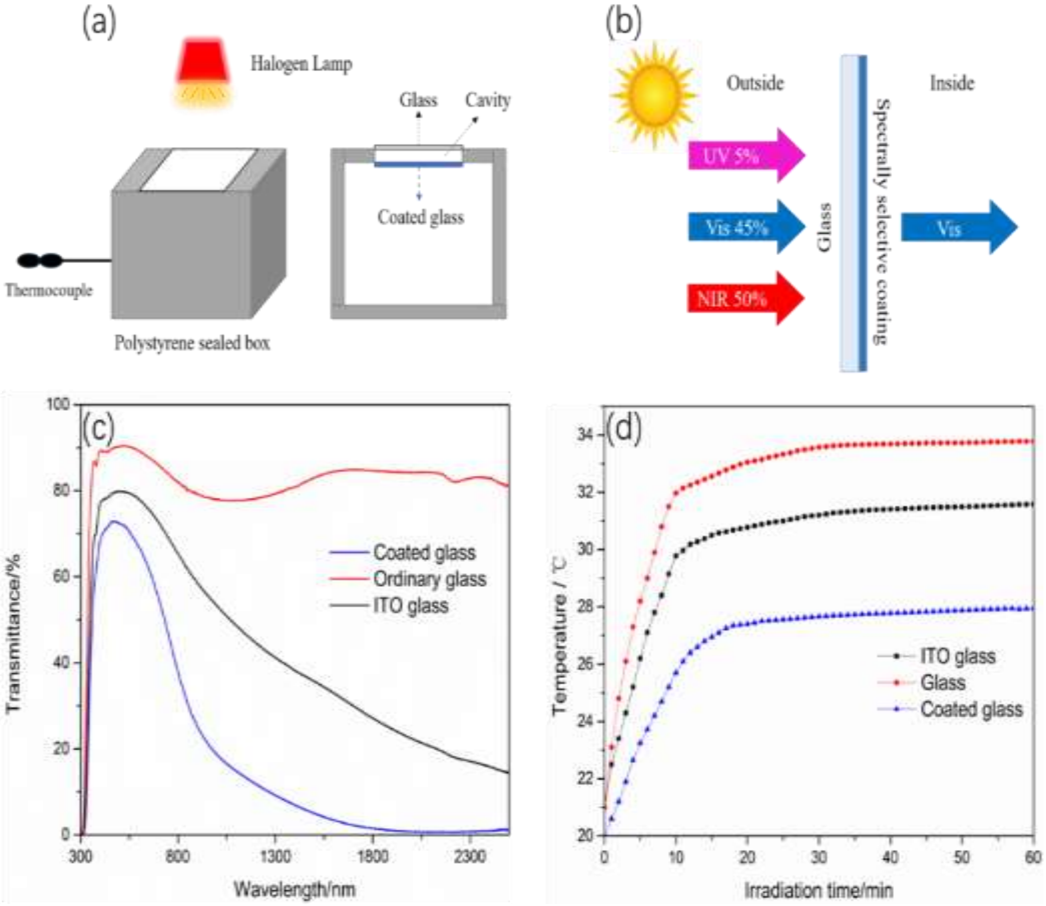

Figure 8.2 (a) Schematic of the device for near-infrared shielding test, (b) Diagram of the transparent heat-shielding mechanism for the coated glass, (c) The UV-Vis-NIR transmittance spectra of coated glass, ITO glass and ordinary glass and (d) The temperature variation of three glass samples with the irradiation time.

The near-infrared blocking property of the glass with as-prepared spectrally selective coating, ITO glass and ordinary glass was investigated by a simulated test using a 500 W halogen lamp as infrared source (Figure 8.2). The test device is shown in the Figure 8.2a, in which the temperature measured by thermocouple indicates the air temperature inside the sealed box. It can be seen that the top side of the device is composed of two glasses with a hollow structure and the sample glass pending test was placed under the ordinary glass. The reason for this design is to minimize the influence of non-radiative heat transfer. As shown in Figure 8.2b, the schematic of transparent heat-shielding mechanism is presented, which is ascribed to its superior spectral selectivity. The UV-Vis-NIR transmittance spectra of coated glass, ITO glass, and ordinary glass are shown in Figure 8.2c. It can be seen that the coated glass showed lower transmittance in the near-infrared wavelength range and maintain a relatively high visible transparency. Figure 8.2d presents the temperature variation recorded by thermocouple of the three glazing samples with the irradiation time. It is observed that the measured temperature with coated glass demonstrated slowest heating rate. The temperature gap between the coated glass and ordinary glass reaches 6.5℃ under 1 h radiation, indicating that the spectrally selective coating on the glass is of excellent near-infrared shielding property. The coated glass is expected to reduce the cooling loads of air-conditioning in summer, aiming to realize energy-saving and emission reduction. By contrast, the ITO glass shows worse near-infrared shielding performance than the coated glass, which only decreases the measured temperature by 2.8℃ compared with ordinary glass. Consequently, the coated glass demonstrates better spectral selectivity than the ITO glass, and it is expected that spectrally selective coatings with high visible transmittance and near-infrared shielding properties will promote practical applications in the field of energy-efficient glazing.

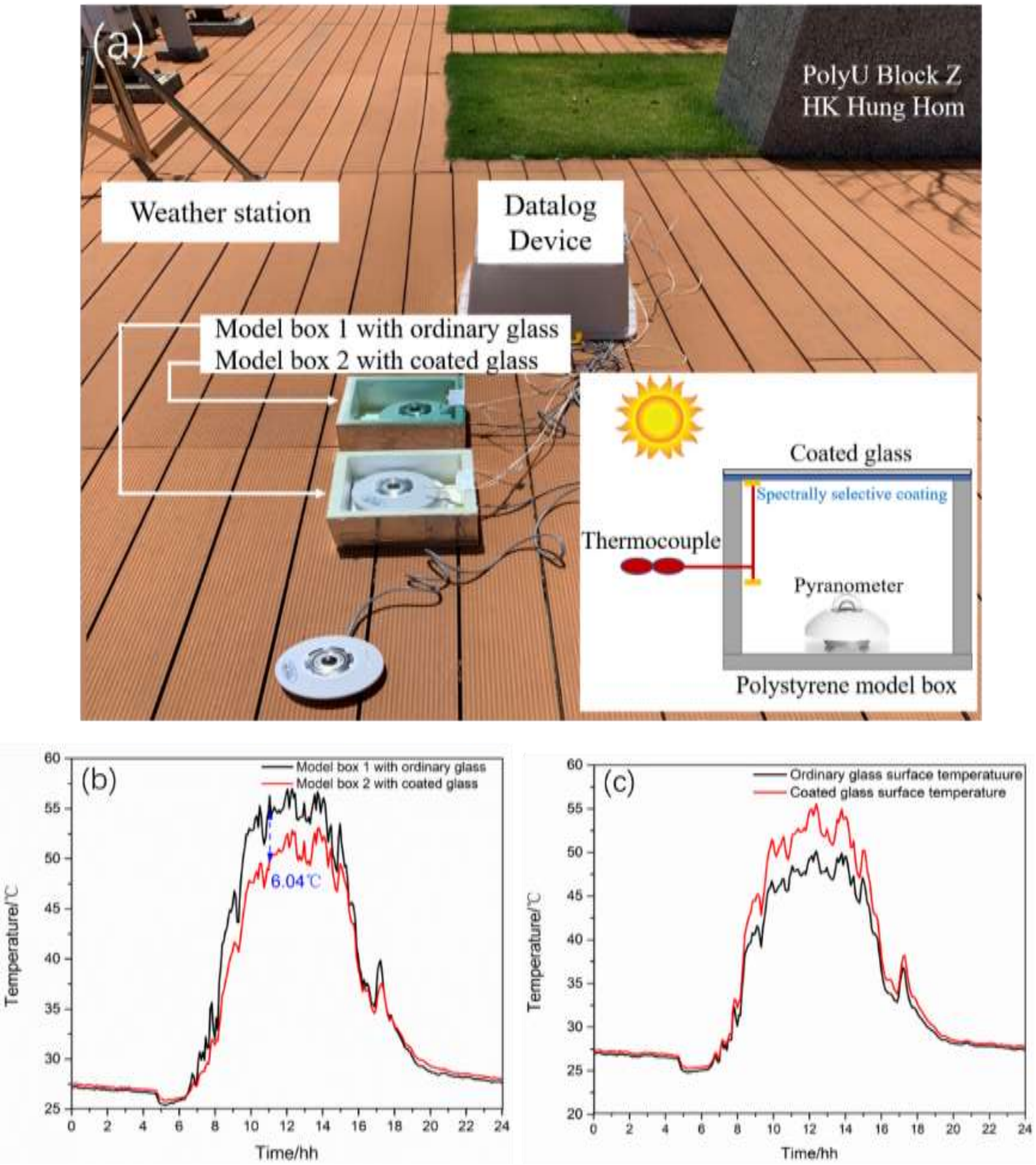

Figure 8.3 (a) Schematic of set up of the model house box, (b) the inside temperature of the two boxes for 24 hours, (c) the glass surface temperature of the two boxes for 24 hours.

As shown in Figure 8.3a, the model box set up was placed on a high-rise platform in PolyU. The glazing surfaces of the two boxes faced the heaven and were regarded as the roof windows. Each box was recorded the inside temperature and glazing surface temperature of the model house box. Figure 8.3b and Figure 8.3c present the temperature difference results. It can be seen that the inside temperature of the box covered by the coated glass demonstrated a lower temperature than that of the box covered by the ordinary glass. Notably, the big temperature difference for 24 hours was 6.04 °C, which further confirms the superior near-infrared shielding performance of the as-fabricated composite coating. Besides, the surface temperature of the box with the coated glass showed a higher temperature than that of the box with the ordinary glass, which can be attributed to the LSPR and small polaron transfer mechanisms.

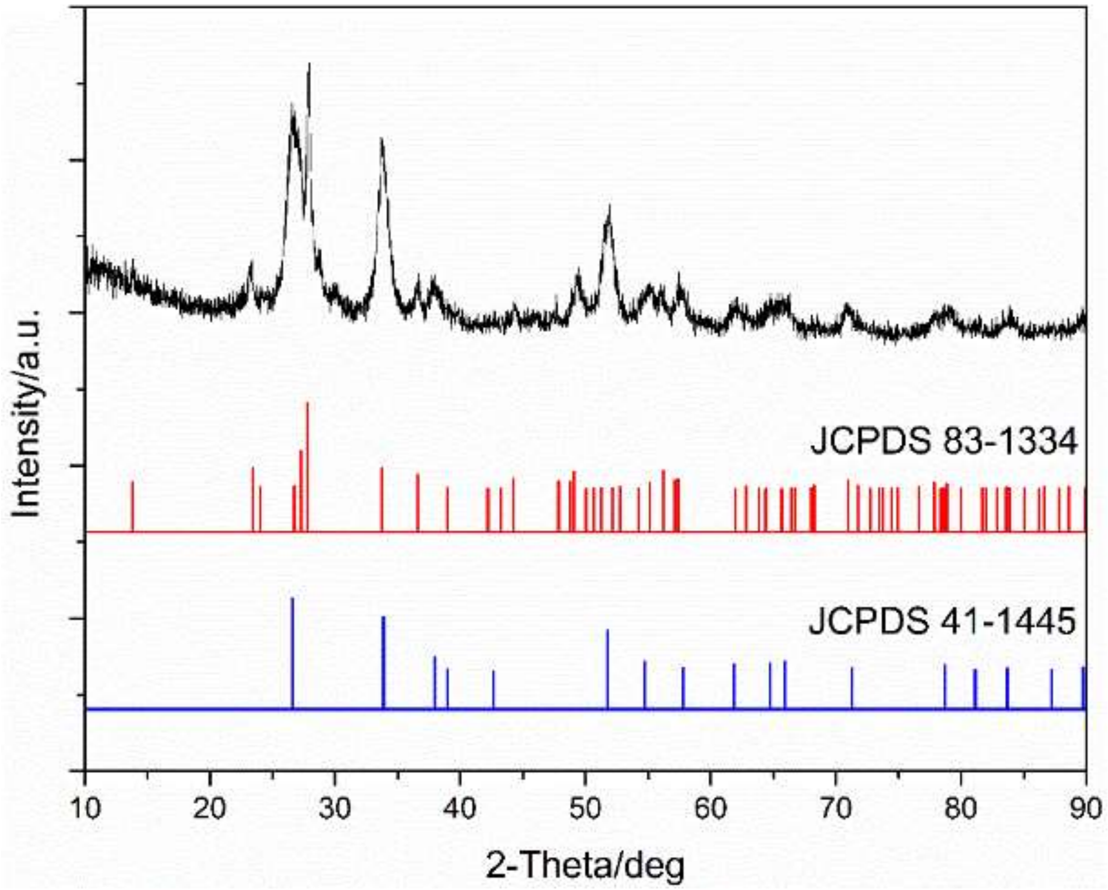

Figure 8.4 XRD pattern of the spectrally selective coating

Figure 8.4 presents the XRD pattern of the spectrally selective coating prepared by dispersion of the two kinds of nanocrystals. It can be seen that the diffraction peaks of the spectrally selective coating can be well indexed to the characteristic peaks of the standard patterns (JCPDS 83-1334 and JCPDS 41-1445). The results indicate that the phase composition of the as-prepared coating consists of two kinds of nanocrystals.

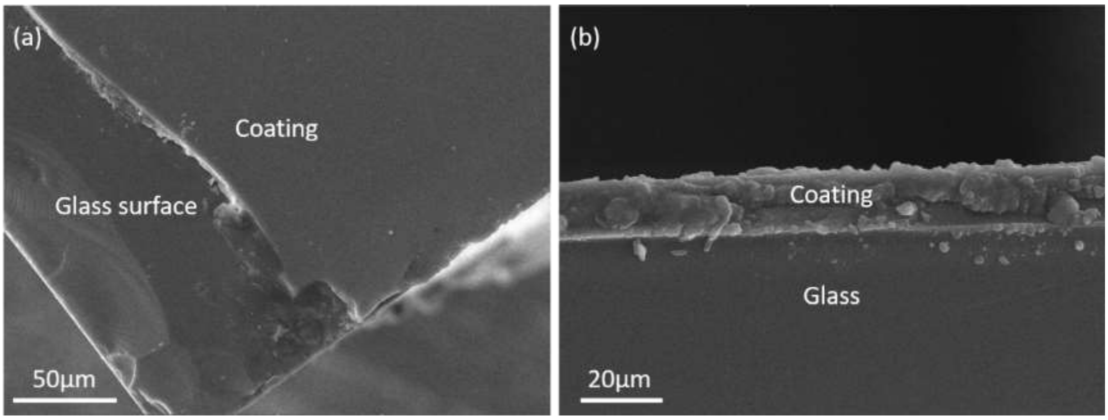

Figure 8.5 SEM images of the (a) top view and (b) cross section of the spectrally selective coating

Figure 8.5 presents the SEM images corresponding to the top view and cross section of the spectrally selective coating. It can be seen that there is a borderline between the coating and the glass surface in Figure. 8.5a. The coating showed homogeneous appearance without obvious grain boundaries, indicating the existence of a large part of amorphous phase. As shown in Figure 8.5b, it is found the cross section of the coating and the glass substrate. The thickness of the coating was estimated to be in range of 15 μm to 20 μm.

Figure 8.6 Photographs of ordinary glass (left) and ordinary glass with the spectrally selective coating

Figure 8.6 shows the photographs of ordinary glass (left) and ordinary glass with the spectrally selective coating with 10 wt%. This spraying technique can be used for both normal windows and skylight glazing. Generally, film-forming methods require a hydrophilic state between the liquid phase product and the substrate surface. Thus, the glazing surface should be pretreated. By contrast, the spraying technique can effectively atomize the liquid phase, which can maximize the contact area between the liquid phase and the glazing surface. Therefore, the spraying technique has better applied adaptability.

Fig. S1 Photos of top view and side view of the coated glass and ordinary glass.

The top view and side view of the box devices, which are covered by coated glass and ordinary glass, respectively, are shown in Fig. S1. On the top of the devices, the coated glass and ordinary glass are both the same size (250 mm × 250 mm × 4 mm). Compared with ordinary glass, the coated glass presents light blue, but it can still transmit most of the visible light because the inside pyranometer can be clearly observed.

The aging test was conducted to utilize fluorescent lamps which provided intense ultraviolet radiation. Standard ASTM G154 and ASTM D1148 was used. To achieve a life-span time of 10 years, a strong UV light (UVB 313) was chosen to conduct the aging test. The UV aging equipment is shown as follows.

Figure 8.7 The inside view of the UV aging equipment

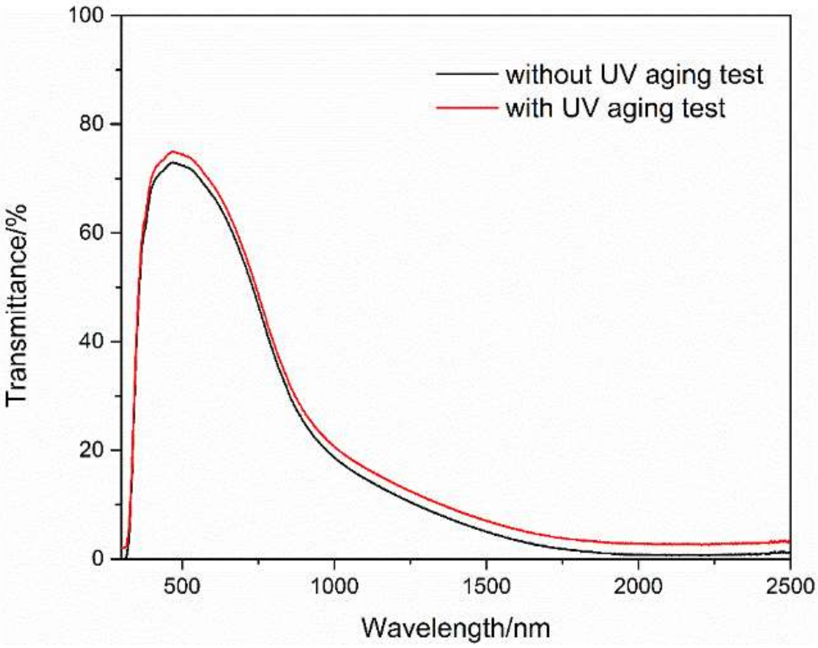

Figure 8.8 The spectra transmittance of the coating with and without UV aging test.

The coated glazing (10 wt%) was placed in the UV aging equipment for 240 hours. It can be seen that the spectra transmittance of the sample experienced the aging test shows an unobvious difference compared with the coating without undergoing the aging test (Figure 8.8).

The durability experiments regarding ambient temperature and relative humidity have not been conducted. As demonstrated in field test, the as-prepared composite coating can maintain spectral selectivity under the direct sunlight and the maximum temperature of the coating surface reached around 55 °C. Besides, the coating matrix used is WPUA and the nanofiller is a kind of inorganic nanoparticles. It is expected that the as-fabricated composite coating can keep stable spectral selectivity in the indoor environment of residential buildings. It was reported that Cs_xWO_3 nanocrystals tended to lose their spectral selectivity under high humidity environment. Because the w^{5+} ions can be oxidized to W^{6+} ions. As shown in the SEM image of the coating, the inorganic nanoparticles were included in the WPUA matrix. Therefore, it is important to prevent nanoparticles from exposing to the outside. Instead of investigating the stability of the as-fabricated coating under high humidity, it is better to investigate the hardness and adhesion of the coating. The adhesion performance of the as-prepared coating was evaluated by ASTM D3359. The coating surface was cut into a number of squares with 5 mm X 5 mm. The tape was placed over the grid and then removed rapidly. The results indicate that the as-fabricated composite coating shows Grade 1 adhesion performance. To assess the resin matrix hardness, the coating prepared by WPUA emulsion was compared with the coating prepared by pure acrylic emulsion and styrene-acrylic emulsion. The hardness of the coating matrix prepared by the WPUA emulsion reached 3H, which is almost the same as the commonly used film-forming resins on the market. The above results illustrate great potential for the practical application. The payback periods of different spectrally selective materials have been calculated and summarized [1]. The payback period of the spectrally selective material is defined as follows:

$$\mathrm{Yr} = \frac{\Delta W}{\Delta U}$$

Yr—payback period of the applying material, year

ΔW—additional initial cost of the applying material, USD

ΔU—annual air conditioning cost saving, USD

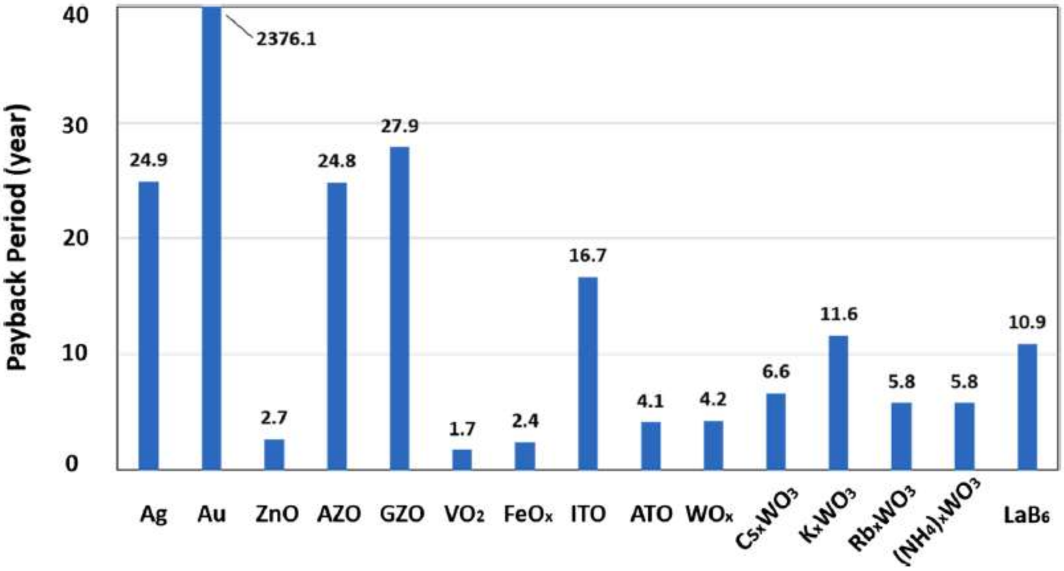

Fig. S2 Payback period of each spectrally selective material used for energy-efficient windows.

The conventional Low-E windows usually use Ag as the spectrally selective material, and it can be seen that the payback period of Ag is nearly 25 years. By contrast, the payback periods of ATO and Cs_xWO_3 are 4.1 and 6.6, respectively, which are competitive to realize practical application in building windows.

8.4 Conclusions

In this chapter, spectrally selective coating with improved near-infrared shielding property was successfully fabricated by simple spraying technique. The composite filler combined with Li, F-codoped Cs_xWO_3 and ATO improved the near-infrared blocking property of the spectrally selective coating. It is proved that the coating prepared the dispersion with solid content of 10 wt% for energy-efficient glazing was of visible T_{Vis} of 70.76%, T_{NIR} of 9.36% and K of 7.56. Furthermore, a directly simple spray fabrication of the spectrally selective coating with improved near-infrared shielding performance is of a positive impact to promote the practical application of the energy-efficient glazing.

Chapter 9

Development of Z-scheme Li, F-codoped Cs_xWO_3/g-C_3N_4 heterostructured composites with plasmonic-enhanced full-spectrum responsive photocatalytic activity and near-infrared shielding performance

9.1 Introduction

Lately, it has been reported that the spectrally selective mechanism of Cs_xWO_3 were highly depended on the free charge density and small polaron transfer. Thus, the majority of NIR energy was absorbed and shielded. Nevertheless, the absorbed NIR energy by Cs_xWO_3 was not further utilized, which is a common waste for the spectrally selective materials. The volatile organic compounds (VOCs) usually refers to benzene, toluene and formaldehyde. A green means to degrade VOCs is photocatalysis. To achieve high photocatalytic activity, two materials are usually combined to form heterostructured composites, especially Z-scheme structure can improve the division rate of holes and charge carriers [147, 155, 181-186]. As a type of cheap and environmentally friendly photocatalyst, g-C_3N_4 was regarded as a promising material with great compatibility, which can be combined with Cs_xWO_3 to form Z-scheme heterostructure.

In this chapter, the novel Z-scheme Li, F-codoped Cs_xWO_3/g-C_3N_4 heterostructured composites were developed as spectrally selective coating to achieve dual functions of spectral selectivity and photocatalysis. The NIR photocatalytic activity of $Cs_xWO_3$was enhanced by co-doping. The novel Z-scheme structure of Li, F-codoped Cs_xWO_3/g-C_3N_4 demonstrated a higher photocatalytic activity than Cs_xWO_3/g-C_3N_4 under full solar-spectrum radiation.

9.2 Experimental

9.2.1 Materials

Ammonium metatungstate hydrate (AMT, $(NH_4)_6H_2W_{12}O_{40} \bullet aH_2O$), cesium carbonate ($Cs_2CO_3$), tartaric acid (TA, $C_4H_6O_6$), deionized water (H_2O), anhydrous ethanol (C_2H_5OH), lithium fluoride (LiF), oleylamine, rhodamine B and melamine were purchased from Macklin. Silicone emulsion was purchased from ShinEtsu Japan.

9.2.2 The preparation of g-C_3N_4

The g-C_3N_4 was synthesized by the following steps. Typically, 15 g melamine was putted into the crucible with a cover. Then, the precursor was transferred into Muffle furnace and heated at 550 °C for 6 hours. The resultant products were grinded into powders and putted into 200 ml ethanol under ultrasonic process for 8 hours. The resultant suspension was centrifugated to remove the bulk g-C_3N_4 particles. Finally, the obtained g-C_3N_4 nanoparticles were dried at 60 °C overnight.

9.2.3 Synthesis of Li, F-codoped Cs_xWO_3 nanocrystals

The Li-doped Cs_xWO_3 nanocrystals were prepared by controllable one-pot method using AMT as W source, Cs_2CO_3 as Cs origin and LiF as Li, F origin respectively. First, a small amount of AMT was dissolved in ethanol with 1mol/L tartaric acid, and then Cs_2CO_3 and LiF were added to the AMT solution with a Cs/W molar ratio of 0.33. The total volume of the mixed solution was 70 ml, of which 15 ml was oleylamine. The solution was then transferred to a

Teflon-lined autoclave with a 200 ml interval volume, and the liquid phase reaction was carried out for 24 hours in a drying oven at 240 °C. Centrifugation was used to collect the products, which were then washed three times with anhydrous ethanol before being vacuum dried at 60°C. The Li, F-codoped Cs_xWO_3 nanocrystals were synthesized with LiF/W molar ratios of 0.2, 0.4, 0.6, and 0.8.

9.2.4 The preparation of Li, F-codoped Cs_xWO_3/g-C_3N_4 heterostructured composite coating

The as-synthesized g-C_3N_4 materials were dispersed in 100 ml ethanol through ultrasonic treatment to prepare the g-C_3N_4 suspension. Then, 10 g pre-synthesized Li, F-codoped Cs_xWO_3 nanoparticles were putted in the above suspension. The mass ratio of g-C_3N_4 relative to Li, F-codoped Cs_xWO_3 nanoparticles was 0.15, 0.30 and 0.45, respectively. The Li, F-codoped Cs_xWO_3/g-C_3N_4 suspension was heated at 50 °C for 10 hours in the vacuum oven to obtain the final product. The resultant nanocomposite was dispersed in the silicone emulsion with s solid content of 10 wt% to obtain a light blue slurry. Finally, the composite coating was fabricated by spin-coating.

9.2.5 Characterization

X-ray diffraction (XRD) with was used to examine the phase compositions of nanoparticles. The morphologies and microstructures of the nanoparticles were obtained by transmission electron microscopy (TEM) with an energy dispersive spectrum (EDS) attachment. X-ray photoelectron spectroscopy (XPS) was used to determine the chemical composition and binding energies of W 4f. The optical performance of the prepared samples was measured by an UV-vis-NIR spectrophotometer.

9.2.6 Photocatalytic test

The photocatalytic activities of the glass substrates with Li, F-codoped Cs_xWO_3/g-C_3N_4 composite coating and Cs_xWO_3/g-C_3N_4 composite coating respectively were determined by analyzing the photodegradation of rhodamine B (RhB) in the aqueous solution under the irradiation in different bands. To avoid the influence of absorption on the test results, the as-fabricated glass substrates were pretreated in 50 mL RhB solutions (25 mg/L) for 2 hours to achieve the absorption-desorption equilibrium. Subsequently, the samples were transferred and immersed in 50 mL RhB solution (10 mg/L), respectively. The RhB solutions containing the samples (10 mg/L) were sufficiently agitated in the dark for 30 minutes prior to irradiation to ensure the establishment of absorption-desorption equilibrium. Following that, the RhB solutions with the glass samples were irradiated with various light sources. A 500 W Mercury lamp was used as the UV light source, with the help of a filter to keep the wavelength below 400 nm. A 300 W Xenon lamp was used as the visible light source, with the help of a filter to keep the wavelength between 400 nm and 760 nm. A 300 W Infrared lamp was used as a near-infrared light source, with the help of a filter to keep the wavelength above 800 nm. During the test, 2 mL supernatant was collected and centrifugated at every irradiation interval (20 min). The residual concentration of RhB was determined by recording the absorbance of the supernatant at 554 nm. Here, C_0 indicates the initial RhB concentration of the supernatant collected from the solution before irradiation, and C represents the residual RhB concentration after the irradiation for each time interval.

9.3 Results and discussion

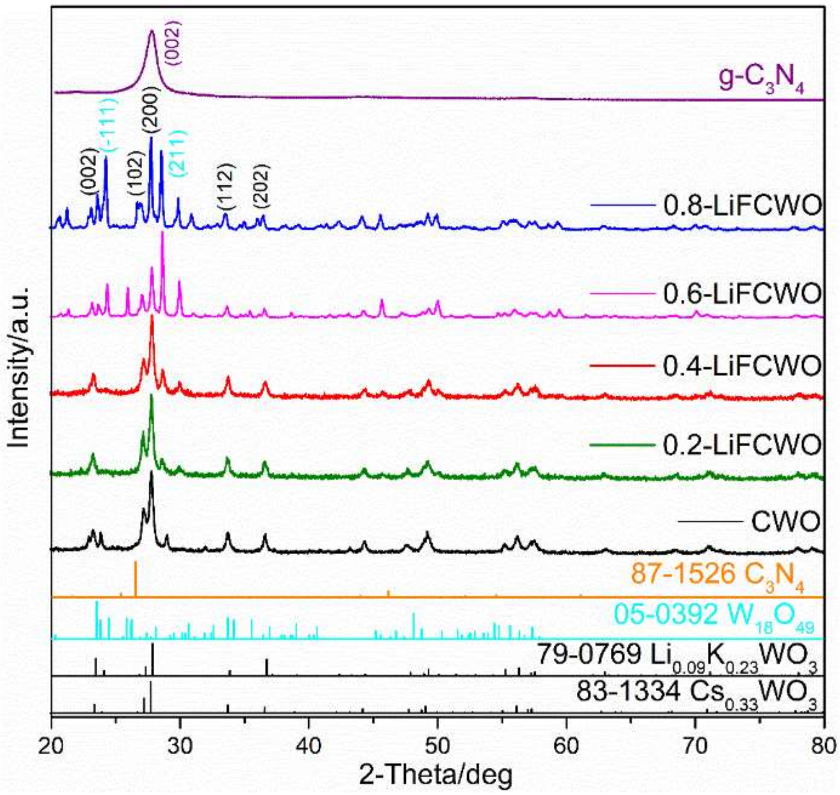

Figure 9.1 XRD patterns of g-C_3N_4, CWO, 0.2-LiFCWO, 0.4-LiFCWO, 0.6-LiFCWO and 0.8-LiFCWO.

XRD was usually utilized to determine the phase compositions and lattice information of the as-prepared samples. As illustrated in Figure 9.1, the XRD pattern of as-synthesized g-C_3N_4 can be well indexed to the C_3N_4 standard pattern (JCPDS NO. 87-1526). When the molar ration of LiF/W was increased to 0.4, a pure hexagonal cesium tungsten bronze has been formed without impurities. When the molar ration of LiF/W is equal to 0.6, insignificant amount of hexagonal phase $Li_{0.09}K_{0.23}WO_3$ (JCPDS NO. 79-0769) and monoclinic phase $W_{18}O_{49}$ (JCPDS NO. 05-0392) was appeared besides dominant hexagonal $Cs_{0.33}WO_3$ phase (JCPDS NO. 83-1334). The separation degree of the (200) and (102) diffraction peaks increased as the LiF proportion increased, which indicated that the product changed from $Cs_{0.33}WO_3$ (JCPDS NO.

83–1334) to $Li_{0.09}K_{0.23}WO_3$ phase (JCPDS NO. 79-0769). The results demonstrate that more Li^+ ions were doped into the crystal lattice of CWO.

As for 0.6-LiFCWO and 0.8-LiFCWO, (-111) and (211) crystal planes of $W_{18}O_{49}$ (JCPDS NO. 05-0392) can be observed, which can be attributed to the highly substitutional fluorine doping in the crystal structure. The results suggest that impurity phases have appeared in 0.6-LiFCWO and 0.8-LiFCWO. Furthermore, the relative intensity of the (200) peak to the (002) peak is higher than the standard level, revealing the preferential growth is along the *a*-axes for 0.4-LiFCWO. In addition, with the increase of LiF/W ratio, the (200) plane diffraction peak of 0.4-LiCWO slightly shifted to higher angle, suggesting that the (200) plane spacing becomes smaller. According to the Bragg equation, this can be explained as follows:

$$2d\sin\theta = n\lambda \tag{9.1}$$

where d stands for crystal interplanar spacing, θ represents incident angle, λ denotes incident light wavelength, and n stands for reflection order. Because nλ is a constant, increasing it implies a decrease in crystal interplanar spacing.

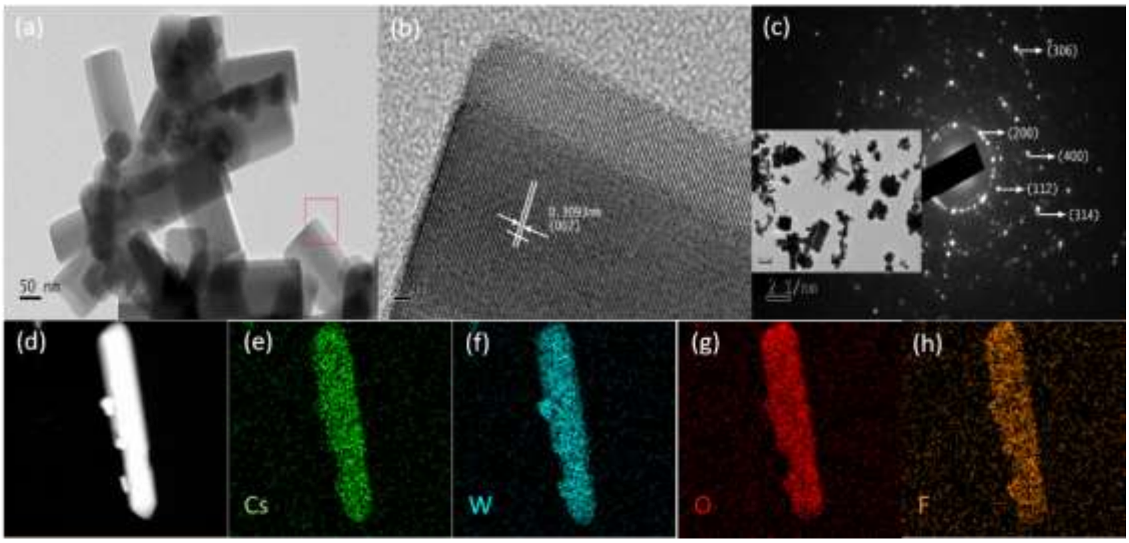

Figure 9.2 (a) TEM image, (b) HR-TEM image, (c) SAED pattern, (d) the TEM image for mapping and (e-h) the element mapping images of 0.4-LiFCWO.

Transmission electron microscopy was used to determine the TEM image, HR-TEM image, and SAED pattern of 0.4-LiFCWO. As illustrated in Figure 9.2a, the nanocrystals show rod-like shape with a certain extent of agglomeration. The lattice spacing of 0.3093 nm is shown in Figure 9.2b, which corresponds to the plane of (002). The hexagonal structure of 0.4LiCWO was verified by the SAED pattern in Figure 9.2c. As shown in Figure 9.2e-h, the elements of F, Cs, W and O are spatially distributed as proved by the element mapping images.

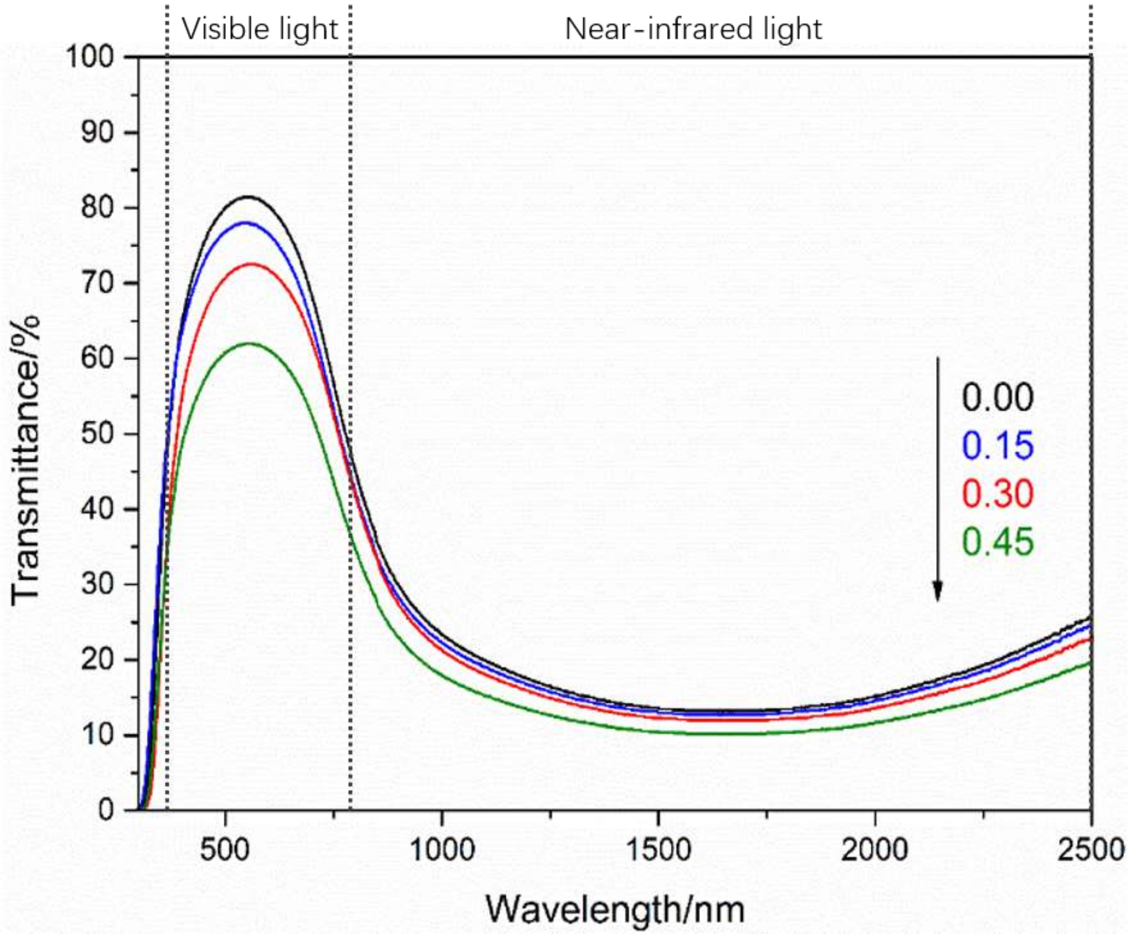

Figure 9.3 The transmittance spectra of composite coatings with different filler mass ratio of $g\text{-}C_3N_4$ to 0.4-LiFCWO

The transmittance spectra of the as-fabricated composite coatings with different filler mass ratio of $g\text{-}C_3N_4$ to 0.4-LiFCWO are presented in Figure 9.3. All of the spectra illustrated superior near-infrared shielding performance. As for the samples with filler mass ratio of 0.00, 0.15, and 0.30, they presented a high average visible transmittance over 70 %, respectively. As the filler mass ratio increased to 0.45, the average visible transmittance of the corresponding film sample significantly decreased to about 60 %, which was not conducive to the daylight requirement of the building windows. In order to balance the excellent spectral selectivity and potential photocatalytic ability of the composite coating, the filler mass ratio of g-C_3N_4 to 0.4-LiFCWO was chosen as 0.30 for further investiation, because the as-prepared coating sample only showed a slightly decrease in visible region compared with the sample with filler mass ratio of 0.45.

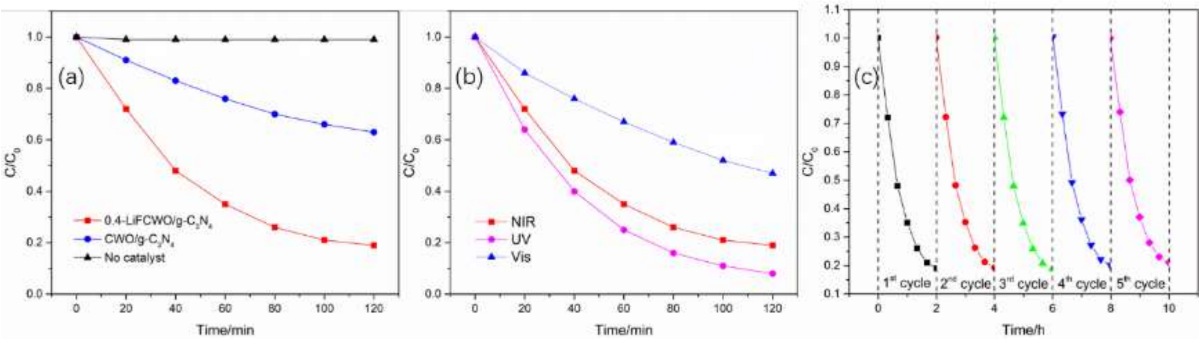

Figure 9.4 (a) Photocatalytic activity of the samples for the degradation of RhB solution when only exposed to NIR light, (b) photocatalytic activity of the composite coating prepared by 0.4-LiFCWO/g-C_3N_4 under different types of light sources, (c) recycling stability experiment of 0.4-LiFCWO/g-C_3N_4 coating in the photodecomposition of RhB under NIR light.

To investigate the photocatalytic activity of the composite coatings prepared by 0.4-LiFCWO/g-C_3N_4 and CWO/g-C_3N_4 with filler mass ratio of 0.30, the glazing sample covered by one of the composite coatings was immersed in RhB solution under different types of light sources, respectively. As shown in Figure 9.4a, the glass sample without the composite coating presented nearly no photocatalytic activity in RhB solution under near-infrared light source. As for the glazing sample covered by the CWO/g-C_3N_4 coating, about 30 % of RhB was decomposed under NIR light. By contrast, the glazing sample covered by the 0.4-LiFCWO/g-C_3N_4 coating illustrated a higher photodegradation efficiency and 80 % of RhB was decomposed after 2 hours exposure under NIR light, indicating that 0.4-LiFCWO are of better NIR catalytic activity than CWO. To further determine the photocatalytic activity of 0.4-LiFCWO/g-C_3N_4 under different types of solar radiation, the photodegradation performance in RhB solution was examined under ultraviolet light, visible light and near-infrared light, respectively. Figure 9.4b shows the photodegradation activity of the composite coating prepared by 0.4-LiFCWO/g-C_3N_4 under different types of light sources. When ultraviolet light was used during the test, the removal efficiency of the coating prepared by 0.4-LiFCWO/g-C_3N_4 was the highest and 90 % of RhB in the solution was decomposed after 2 hours under the exposure of ultraviolet. Besides, nearly 80 % of RhB was decomposed by 0.4-LiFCWO/g-C_3N_4 composite coating during the 2 hours exposure of NIR light. However, only 50 % RhB in the solution was removed after 2 hours under visible light, which was obviously lower than the photodegradation efficiency under ultraviolet and NIR light. Furthermore, recycling stability experiment of the as-fabricated coating was conducted to evaluate its potential long-term practical application. As shown in Figure 9.4, no evident decreases of photocatalytic activity can be observed after five continuous cycling experiments, indicating that the as-prepared composite coating is of a high stability.

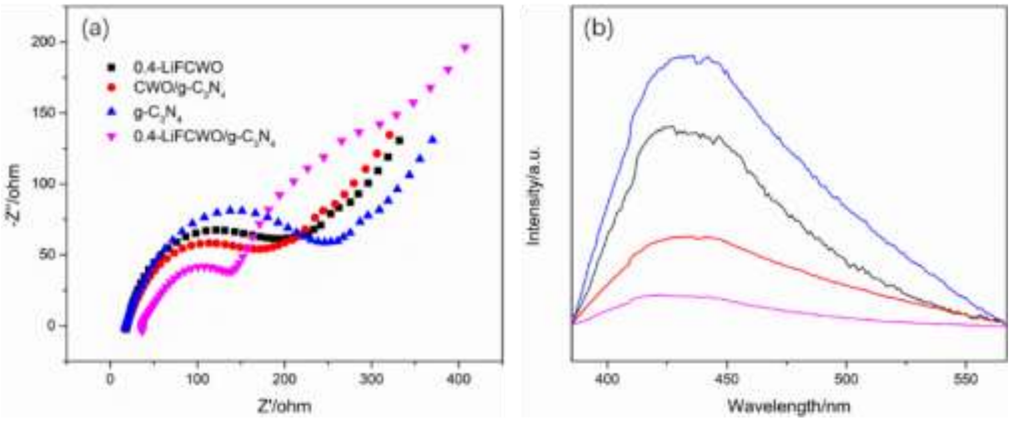

Figure 9.5 (a) Electrochemical impedance spectra and (b) photoluminescence spectra of g-C_3N_4, 0.4-LiFCWO, CWO/g-C_3N_4 and 0.4-LiFCWO/g-C_3N_4.

The degree of charge carrier separation of g-C_3N_4, 0.4-LiFCWO, CWO/g-C_3N_4 and 0.4-LiFCWO/g-C_3N_4 was examined by the electrochemical impedance experiment, respectively. As show in Figure 9.5a, the impedance-circle radius of 0.4-LiFCWO/g-C_3N_4 is obviously smaller than that of CWO/g-C_3N_4, suggesting that 0.4-LiFCWO exhibits a stronger synergistic effect on charge separation efficiency than CWO with the combination of g-C_3N_4. In addition, the extent of charge transition and separation was further investigated by the photoluminescence (PL) spectra of g-C_3N_4, 0.4-LiFCWO, CWO/g-C_3N_4 and 0.4-LiFCWO/g-C_3N_4. As illustrated in Figure 9.5b the photoluminescence spectra of g-C_3N_4 and 0.4-LiFCWO shows a significant emission peak at about 440 nm, which is attributed to photogenerated holes and electrons recombination. Compared with CWO/g-C_3N_4, 0.4-LiFCWO/g-C_3N_4 illustrated a weaker emissions intensity. The results indicate that 0.4-LiFCWO/g-C_3N_4 has highly charge separation efficiency, which leads to the superior photocatalytic activity.

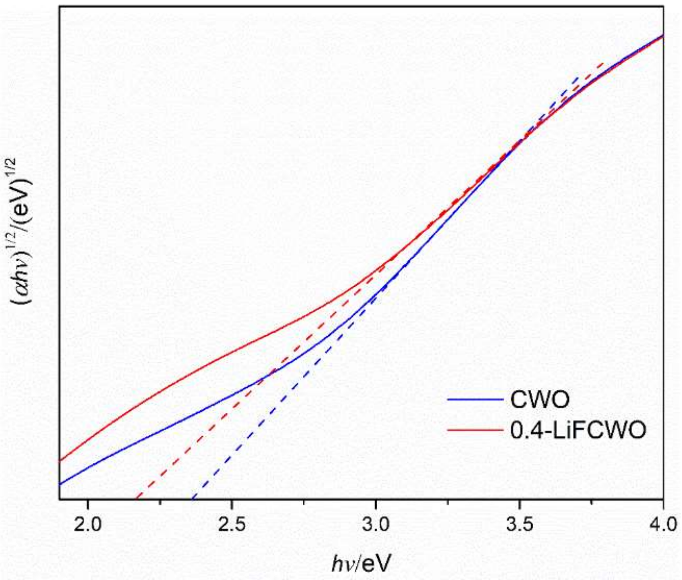

Figure 9.6 Tauc plot of CWO and 0.4-LiFCWO for the band gap

The Tauc plot of CWO and 0.4-LiFCWO are presented in Figure 9.6. It was discovered that the absorbance spectrum of 0.4-LiFCWO had a red shift when compared to that of CWO. The color of CWO powder also changed from blue to dark gray after doping LiF. The band gap of CWO and 0.4-LiFCWO are determined by the following formula:

$$\alpha h v = A(h v - E_g)^{n/2} \tag{9.2}$$

Where α indicates absorption coefficient, h is Plank constant and E_g represents the band gap. The value of n is 4 for indirect transition and 1for direct transition. Here, tungsten bronze is attributed to the indirect transition. A plot of $(\alpha h v)^{1/2}$ vs $h v$ can be used to calculate the value of band gap. The obtained band gap of CWO and 0.4-LiFCWO was 2.37 eV and 2.17 eV, respectively. After doping with LiF, the band gap can be declined, and the corresponding absorption spectrum makes a blue-shift. Consequently, the conduction band (CB) and valence band (VB) potential of 0.4-LiFCWO can be calculated by the following equations [181]:

$$E_{VB} = X - E_e + 0.5E_g \tag{9.3}$$

$$E_{CB} = E_{VB} - E_g \tag{9.4}$$

Where X represents the absolute electronegativity of the semiconductor, E_e (4.5 eV)indicates the free electron energy on the hydrogen scale and E_g is the value of the band gap energy for the semiconductor. The band gap energy of g-C_3N_4 was reported to be 2.70 eV, with the conduction band and valence band positions adopted as -1.13 eV and 1.57 eV, respectively. [182]. The conduction band and valence band positions of 0.4-LiFCWO were calculated as 0.42 eV and 2.59 eV, respectively. The related values were presented in Table 9.1.

Table 9.1 The absolute electronegativity, band gap, VB and CB positions of g-C_3N_4 and 0.4-LiFCWO.

Semiconductors	X (eV)	E_g (eV)	VB (eV)	CB (eV)
g-C_3N_4	4.67	2.70	1.57	-1.13
0.4-LiFCWO	6.00	2.17	2.59	0.42

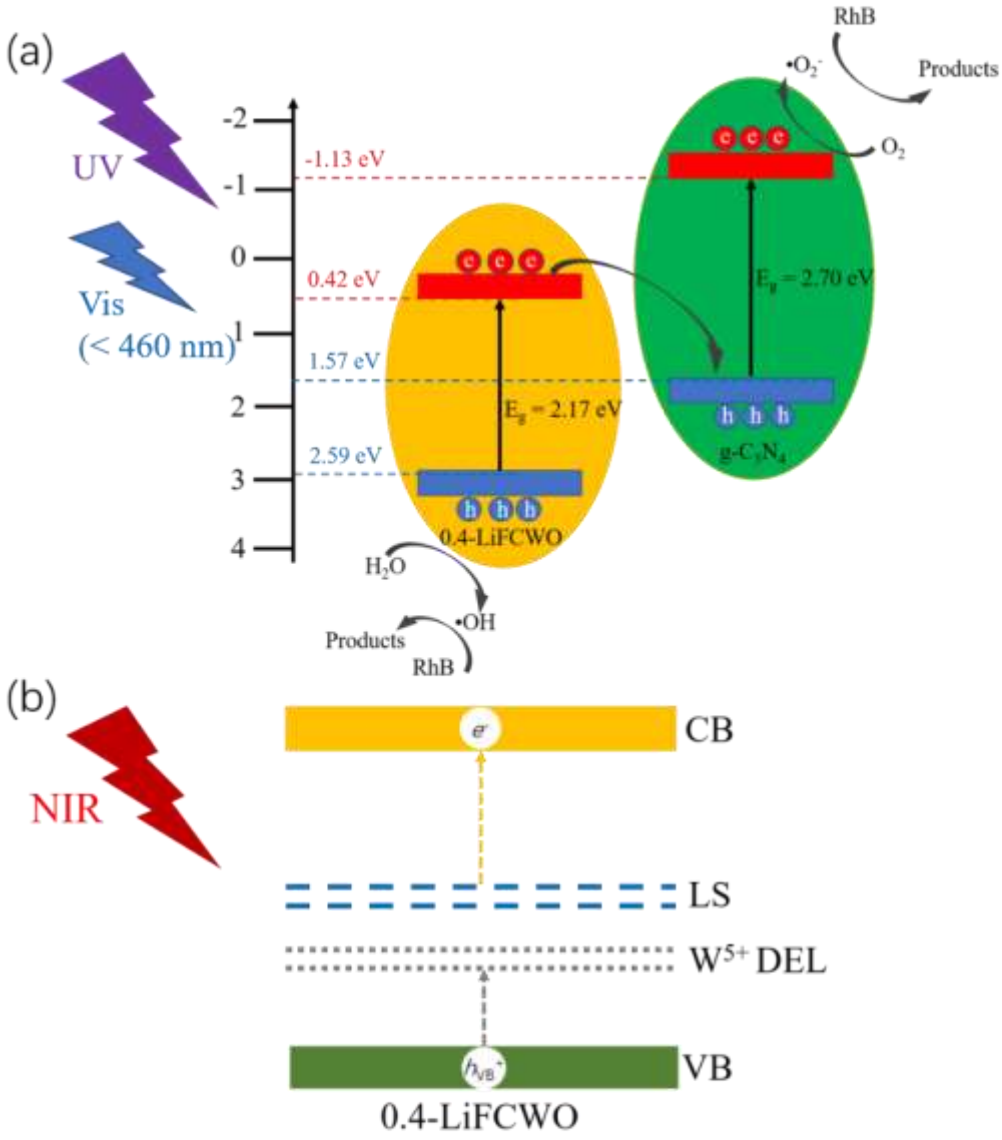

Figure 9.7 (a) Schematic diagram of 0.4-LiFCWO/g-C_3N_4 Z-scheme heterostructure under UV irradiation, (b) schematic representation of the NIR photocatalytic mechanism of 0.4-LiFCWO.

Accordingly, the combination of g-C_3N_4 and 0.4-LiFCWO can create a typical Z-scheme heterostructure. As shown in Figure 9.7a, the photogenerated electrons in the conduction band of 0.4-LiFCWO can easily move to the valence band of g-C_3N_4 under ultraviolet and part of visible radiation, which is conducive for the effective separation of photoexcited hole-electron pairs and enhances the photocatalytic activity. The results are in accordance with the results of photoelectrochemical and photoluminescence findings. Notably, a Z-scheme composite photocatalyst can be formed by the combination of g-C_3N_4 and 0.4-LiFCWO, and the photogenerated electrons and holes are effectively segregated. Figure 9.7b shows the NIR catalytic mechanism, which is related to the content of W^{5+} and localized electrons. The co-doping of LiF can increase the free electrons in the CWO, which contributes to the content of W^{5+} in the crystal structure corresponding to the above XPS findings. It has been reported that high concentration of W^{5+} can form a defect energy level (DEL) under the conduction band of CWO. Thus, the holes can be generated after the electrons are excited to the defect energy level under the NIR irradiation. The resultant holes are combined with H_2O and generate •OH. Besides, there are some electrons with localized states located at energy level under the conduction band [147]. The NIR wavelength ranging from 800 nm to 1100 nm can excite the localized electrons to move to the conduction band of 0.4-LiFCWO, which leads to the NIR photocatalysis. Compared with CWO, the co-doping of LiF can further enhance the content of free electrons and the localized electrons. As a result, the localized electrons excited into the conduction band can accelerate the generation of $\bullet O_2^-$. Finally, the resultant •OH and $\bullet O_2^-$ can effectively degrade RhB in the solution. The detailed mechanisms of NIR photocatalysis are demonstrated as follows:

$$\text{0.4-LiFCWO} + \text{NIR} \rightarrow h_{\text{VB}}^{+} + e^{-} \tag{9.5}$$

$$h_{\text{VB}}^{+} + H_2O \rightarrow \bullet OH \tag{9.6}$$

$$e^{-} + O_2 \rightarrow \bullet O_2^{-} \tag{9.7}$$

$$\bullet OH + \bullet O_2^{-} + \text{RhB} \rightarrow \text{Degradation} \tag{9.8}$$

9.4 Conclusions

Z-scheme Li, F-codoped Cs_xWO_3/g-C_3N_4 heterostructured composites were successfully prepared with plasmonic-enhanced full-spectrum responsive photocatalytic activity and near-infrared shielding performance for energy-efficient windows. The highly efficient charge separation mechanism was illustrated in detail. As a consequence, the Z-scheme Li, F-codoped Cs_xWO_3/g-C_3N_4 showed improved photocatalytic activity than Cs_xWO_3/g-C_3N_4, which can be ascribed to the effective holes and electrons separation. The combination of Li, F-codoped Cs_xWO_3/g-C_3N_4 is a promising way to promote dual function coating applied in the field of windows for buildings.

Chapter 10

Conclusion and Recommendation for Future Work

10.1 Summary of the findings and contributions

Solar radiation passing through the windows is the most significant source of heat gain in buildings. The energy-efficient windows with ideal spectrally selective coating can shield most of the near-infrared radiation. Accordingly, it is necessary to develop spectrally selective materials, which can be easily deposited on the glazing surface and have superior spectral selectivity. In this thesis, a comprehensive literature review on the different types of spectrally selective materials, its applications in buildings and deposition techniques was summarized. Besides, the corresponding research gaps were identified. Based on the pros and cons of existing spectrally selective materials, both of ATO and Li, F-codoped Cs_xWO_3 nanocrystals were developed to fabricate a novel composite coating with superior spectral selectivity. The significant findings are concluded as follows.

10.1.1 The development of low-agglomerated ATO nanoparticles with optimal doping ratio

Firstly, a dual co-precipitation method was developed to prepare the ATO nanoparticles with low agglomeration, which is conducive to prepare stable dispersion for spraying fabrication of spectrally selective coating. Various annealing temperatures, doping molar ratios and ethanol content of precursor solution were used to investigate the influence on the morphology and phase composition of the as-synthesized ATO powders. It has been proved that the dual-titration way is conducive to inhibit the aggregation of primary particles. The optimal experimental reaction conditions to synthesize ATO nanoparticles with near-infrared shielding performance show that the molar ratio is 10% and the annealing temperature is 1000°C. ATO primary nanoparticles were gained ranging from 45 to 55nm with a low aggregated degree.

Besides, the effect of the pH titration endpoint on doping level and optical performance was systematically studied. The phase composition, element composition, valence state of Sb ions, microstructure and thermal characteristics of ATO nanocrystals with different pH titration endpoint were comprehensively investigated. When the pH value of the titration endpoint was 6, the measured doping ratio of Sb was 10.81% which was close to the initial Sb doping level of 10%. Meanwhile, the content of Sb^{5+} ions also reached the maximum value of 76.4%, which indicates that the as-prepared ATO nanocrystals illustrate optimal optical performance.

10.1.2 The development of one-pot synthesis of Cs_xWO_3 nanocrystals and the investigation of the growth mechanism

A simple one-pot method for controllable synthesis of Cs_xWO_3 nanocrystals was developed using stable and relatively cheap ammonium metatungstate and cesium carbonate as starting materials to improve NIR shielding performance in the wavelength range of 1000 nm to 1500 nm. The reducibility of tartaric acid, tartaric acid with chloroplatinic acid were studied, and the possible synthetic mechanisms of Cs_xWO_3 nanocrystals with different crystalline phase were investigated in detail. In the as-synthesized product, tartaric acid with chloroplatinic acid as the reductant had the highest reducibility and could produce the most W5+ ions. It has been established that chloroplatinic acid has a significant impact on tartaric acid reducibility. It is of great significance for synthesizing low-cost production of hexagonal Cs_xWO_3 nanocrystals without post heat-treatment and promoting its practical application in the field of energy-efficient glazing.

10.1.3 The development of Cs_xWO_3 nanocrystals with enhanced localized surface plasmon resonance and small polaron transfer through LiF co-doping

For further improving the optical properties of Cs_xWO_3 nanocrystals, Li, F-codoped Cs_xWO_3 nanocrystals were successfully prepared with the highest reported absorption coefficient, which demonstrated stronger absorption performance than the Cs_xWO_3 nanocrystals without doping. The introduction of lithium and fluorine into the crystal structure as a cation-anion co-dopant can enhance the free carrier density of the nanocrystals, which leads to a higher absorption coefficient. The absorption coefficient variation of LSPR and small polaron transfer of Li, F-codoped Cs_xWO_3 nanocrystals was explained by the free carrier density and carrier mobility. This doping strategy allows Cs_xWO_3 nanocrystals to become spectrally tunable within the wavelength of near-infrared radiation. When the LiF/W molar ratio was 0.4, the free carrier density reached 11.94×10^{14} cm^{-3}. This doping strategy provides promising potential to improve the spectral tunability of Cs_xWO_3 nanocrystals for the practical application of energy-saving windows.

10.1.4 The development of Sb-doped SnO_2/Li, F-codoped Cs_xWO_3/UV-curable WPUA in-situ polymerization coating by spraying fabrication

For promoting the practical applications of the spectrally selective coating, spraying fabrication of Sb-doped SnO_2/Li, F-codoped Cs_xWO_3/UV-curable WPUA in-situ polymerization coating was developed for the retrofitting of installed windows. Low-agglomerated ATO nanoparticles and Li, F-codoped Cs_xWO_3 nanoparticles were combined to realize superior NIR shielding performance. The optical parameters of the composite coating prepared the dispersion with solid content of 10 wt% was T_{Vis} of 70.76%, T_{NIR} of 9.36% and K of 7.56. Compared with the coating prepared by the physical blending method, the in-situ polymerization coating showed better dispersion and higher visible transmittance. Besides, the film-forming agent used was UV-curable WPUA, which can help to fast form the composite layer and solve the problem of long film-forming time for other resins. The spraying fabrication of the in-situ polymerization coating with improved near-infrared shielding performance is of a positive impact to facilitate the practical application in the retrofitting of existing windows.

10.1.5 The development of Z-scheme Li, F-codoped Cs_xWO_3/g-C_3N_4 heterostructured composites with photocatalytic activity and near-infrared shielding performance

Finally, the novel Z-scheme Li, F-codoped Cs_xWO_3/g-C_3N_4 heterostructured composites were prepared to achieve dual functions of spectral selectivity and photocatalysis. The NIR photocatalytic activity of Cs_xWO_3 was enhanced by impurity co-doping. The novel Z-scheme structure of Li, F-codoped Cs_xWO_3/g-C_3N_4 demonstrated a higher photocatalytic activity than Cs_xWO_3/g-C_3N_4 under full solar-spectrum radiation. Both of the photoelectrochemical measurements and the photoluminescence spectra demonstrated that the Z-scheme Li, F-codoped Cs_xWO_3/g-C_3N_4 illustrated stronger photodegradation ability than Cs_xWO_3/g-C_3N_4, which can be ascribed to the effective holes and electrons separation. The combination of Li, F-codoped Cs_xWO_3/g-C_3N_4 provides dual function of the coating which can be applied in the field of windows. This strategy provided a novel idea into the preparation of the multifunctional coatings for smart windows.

10.2 Recommendations for future work

Spraying fabrication of the in-situ polymerization coating with superior spectral selectivity was successfully prepared and has been proved to effectively reduce the indoor temperature of the buildings. However, to continue to optimize the developed techniques and promote the commercialization, further works are required as follows:

1) Although simulated test and field test have been conducted, it still lacks the analysis of estimation of energy-saving by the developed energy-efficient glazing and the potential of energy-saving stays uncertain instead of quantified.
2) The combination of Li, F-codoped Cs_xWO_3 and g-C_3N_4 realized the dual function of photocatalysis and spectral selectivity. However, it still has a lot of room to explore other material combinations to achieve multifunction, maybe self-cleaning.
3) From the viewpoint of practical application, the developed coating should be of great wear-resistance ability and durability. As a result, the mechanical abilities of the coating need to be further investigated and evaluated in the future.

The above-mentioned works would give a better direction to optimize the spectrally selective coating. Therefore, the spectrally selective coating with great durability would spread into the commercial market in the near future.

REFERENCES

[1] Zheng L, Xiong T, Shah KW. Transparent nanomaterial-based solar cool coatings: Synthesis, morphologies and applications. Solar Energy. 2019;193:837-58.

[2] Garlisi C, Trepci E, Li X, Al Sakkaf R, Al-Ali K, Nogueira RP, et al. Multilayer thin film structures for multifunctional glass: Self-cleaning, antireflective and energy-saving properties. Applied Energy. 2020;264.

[3] Wu C-M, Naseem S, Chou M-H, Wang J-H, Jian Y-Q. Recent Advances in Tungsten-Oxide-Based Materials and Their Applications. Frontiers in Materials. 2019;6.

[4] Ke Y, Chen J, Lin G, Wang S, Zhou Y, Yin J, et al. Smart Windows: Electro-, Thermo-, Mechano-, Photochromics, and Beyond. Advanced Energy Materials. 2019;9.

[5] Ji H, Liu D, Cheng H, Tao Y. Large area infrared thermochromic VO2 nanoparticle films prepared by inkjet printing technology. Solar Energy Materials and Solar Cells. 2019;194:235-43.

[6] Tällberg R, Jelle BP, Loonen R, Gao T, Hamdy M. Comparison of the energy saving potential of adaptive and controllable smart windows: A state-of-the-art review and simulation studies of thermochromic, photochromic and electrochromic technologies. Solar Energy Materials and Solar Cells. 2019;200.

[7] Rezaei SD, Shannigrahi S, Ramakrishna S. A review of conventional, advanced, and smart glazing technologies and materials for improving indoor environment. Solar Energy Materials and Solar Cells. 2017;159:26-51.

[8] Chao L, Bao L, Wei W, Tegus O. A review of recent advances in synthesis, characterization and NIR shielding property of nanocrystalline rare-earth hexaborides and tungsten bronzes.

Solar Energy. 2019;190:10-27.

[9] Aburas M, Soebarto V, Williamson T, Liang R, Ebendorff-Heidepriem H, Wu Y. Thermochromic smart window technologies for building application: A review. Applied Energy. 2019;255.

[10] Jelle BP, Kalnæs SE, Gao T. Low-emissivity materials for building applications: A state-of-the-art review and future research perspectives. Energy and Buildings. 2015;96:329-56.

[11] Hee WJ, Alghoul MA, Bakhtyar B, Elayeb O, Shameri MA, Alrubaih MS, et al. The role of window glazing on daylighting and energy saving in buildings. Renewable and Sustainable Energy Reviews. 2015;42:323-43.

[12] Cuce E, Riffat SB. A state-of-the-art review on innovative glazing technologies. Renewable and Sustainable Energy Reviews. 2015;41:695-714.

[13] Abundiz-Cisneros N, Sanginés R, Rodríguez-López R, Peralta-Arriola M, Cruz J, Machorro R. Novel Low-E filter for architectural glass pane. Energy and Buildings. 2020;206.

[14] Ye X, Wang Z, Zhang L, Wang Q, Xiao X, Cai S, et al. Synthesis and infrared emissivity properties of novel polyurethane/Ag/ZnO array composite coatings. Infrared Physics & Technology. 2019;102.

[15] Lin S, Wang H, Zhang X, Wang D, Zu D, Song J, et al. Direct spray-coating of highly robust and transparent Ag nanowires for energy saving windows. Nano Energy. 2019;62:111-6.

[16] Sun K, Tang X, Yang C, Jin D. Preparation and performance of low-emissivity Al-doped ZnO films for energy-saving glass. Ceramics International. 2018;44:19597-602.

[17] Chow T-t, Li C, Lin Z. Innovative solar windows for cooling-demand climate. Solar Energy Materials and Solar Cells. 2010;94:212-20.

[18] Sun H, Deng K, Zhu Y, Liao M, Xiong J, Li Y, et al. A Novel Conductive Mesoporous Layer with a Dynamic Two-Step Deposition Strategy Boosts Efficiency of Perovskite Solar Cells to 20. Adv Mater. 2018;30:e1801935.

[19] Huang A, Lei L, Zhu J, Yu Y, Liu Y, Yang S, et al. Fast Fabrication of a Stable Perovskite Solar Cell with an Ultrathin Effective Novel Inorganic Hole Transport Layer. Langmuir. 2017;33:3624-34.

[20] Liu C, Cheng YB, Ge Z. Understanding of perovskite crystal growth and film formation in scalable deposition processes. Chem Soc Rev. 2020;49:1653-87.

[21] Cuce E, Harjunowibowo D, Cuce PM. Renewable and sustainable energy saving strategies for greenhouse systems: A comprehensive review. Renewable and Sustainable Energy Reviews. 2016;64:34-59.

[22] Wang M, Xu Y, Liu Y, Wu W, Xu S. Synthesis of Sb-doped SnO2 (ATO) hollow microspheres and its application in photo-thermal shielding coating. Progress in Organic Coatings. 2019;136.

[23] Qin Y, Zhang M, Guan Y, Huang X. Laser absorption and infrared stealth properties of Al/ATO composites. Ceramics International. 2019;45:14312-5.

[24] Li Y, Zeng G, Yang G, Wu Q, Zhang H, Li W, et al. Synthesis, characterization and properties of ATO/potassium silicate film prepared by twice spray pyrolysis. Journal of Alloys and Compounds. 2019;772:240-6.

[25] Huang X-J, Zeng X-F, Wang J-X, Zhang L-L, Chen J-F. Synthesis of monodispersed ZnO@SiO2 nanoparticles for anti-UV aging application in highly transparent polymer-based nanocomposites. Journal of Materials Science. 2019;54:8581-90.

[26] Yang L, Huang J, Shi L, Cao L, Liu H, Liu Y, et al. Sb doped SnO2-decorated porous g-C3N4 nanosheet heterostructures with enhanced photocatalytic activities under visible light irradiation. Applied Catalysis B: Environmental. 2018;221:670-80.

[27] Yu N, Peng C, Wang Z, Liu Z, Zhu B, Yi Z, et al. Dopant-dependent crystallization and photothermal effect of Sb-doped SnO2 nanoparticles as stable theranostic nanoagents for tumor ablation. Nanoscale. 2018;10:2542-54.

[28] Hu Y, Zhong H, Wang Y, Lu L, Yang H. TiO2/antimony-doped tin oxide: Highly water-dispersed nano composites with excellent IR insulation and super-hydrophilic property. Solar Energy Materials and Solar Cells. 2018;174:499-508.

[29] Xu X, Zhang W, Hu Y, Wang Y, Lu L, Wang S. Preparation and overall energy performance assessment of wide waveband two-component transparent NIR shielding coatings. Solar Energy Materials and Solar Cells. 2017;168:119-29.

[30] Huang H, Ng M, Wu Y, Kong L. Solvothermal synthesis of Sb:SnO2 nanoparticles and IR shielding coating for smart window. Materials & Design. 2015;88:384-9.

[31] Sharma S, Volosin AM, Schmitt D, Seo D-K. Preparation and electrochemical properties of nanoporous transparent antimony-doped tin oxide (ATO) coatings. J Mater Chem A. 2013;1:699-706.

[32] Liu S, Jiang W, Liu C, Ding W, Chai W. Preparation and characterization of ATO nanoparticles by various coprecipitation. Journal of Materials Science: Materials in Electronics. 2012;24:594-600.

[33] Liu S-m, Ding W-y, Chai W-p. Influence of Sb doping on crystal structure and electrical property of SnO2 nanoparticles prepared by chemical coprecipitation. Physica B: Condensed

Matter. 2011;406:2303-7.

[34] Gokulakrishnan V, Parthiban S, Jeganathan K, Ramamurthi K. Investigations on the structural, optical and electrical properties of Nb-doped SnO2 thin films. Journal of Materials Science. 2011;46:5553-8.

[35] Zhang J, Gao L. Synthesis and characterization of antimony-doped tin oxide (ATO) nanoparticles by a new hydrothermal method. Materials Chemistry and Physics. 2004;87:10-3.

[36] Zhang J, Gao L. Synthesis and characterization of antimony-doped tin oxide (ATO) nanoparticles. Inorganic Chemistry Communications. 2004;7:91-3.

[37] Song X, Liu J, Shi F, Fan C, Ran S, Zhang H, et al. Facile fabrication of KmCsnWO3 with greatly improved near-infrared shielding efficiency based on W5+-induced small polaron and local surface plasmon resonance (LSPR) modulation. Solar Energy Materials and Solar Cells. 2020;218.

[38] Liu G, Kong F, Xu J, Li R. Novel synthesis of 0D, 1D and 2D nano-CsxWO3 and their tunable optical-thermal response performance. Journal of Materials Chemistry C. 2020.

[39] Qi S, Xiao X, Lu Y, Huan C, Zhan Y, Liu H, et al. A facile method to synthesize small-sized and superior crystalline Cs0.32WO3 nanoparticles for transparent NIR shielding coatings. CrystEngComm. 2019;21:3264-72.

[40] Peng L, Chen W, Su B, Yu A, Jiang X. CsxWO3 nanosheet-coated cotton fabric with multiple functions: UV/NIR shielding and full-spectrum-responsive self-cleaning. Applied Surface Science. 2019;475:325-33.

[41] Liu J, Ran S, Fan C, Qiao Y, Shi F, Yang J, et al. One pot synthesis of Pt-doped CsxWO3 with improved near infrared shielding for energy-saving film applications. Solar Energy.

2019;178:17-24.

[42] Fan C-Y, Liu J-X, Shi F, Ran S, Chen B, Zhou J, et al. Facile synthesis of urchin-like CsxWO3 particles with improved transparent thermal insulation using bacterial cellulose as a template. RSC Advances. 2019;9:5804-14.

[43] Zheng B, Han Z, Wu G, Liu Y, Liu C, Ma F. Synthesis of near infrared-activatable KxWO3 nanorods for photothermal therapy. Materials Letters. 2018;212:194-7.

[44] Yao Y, Zhang L, Chen Z, Cao C, Gao Y, Luo H. Synthesis of Cs x WO 3 nanoparticles and their NIR shielding properties. Ceramics International. 2018;44:13469-75.

[45] Xu Q, Xiao L, Ran J, Tursun R, Zhou G, Deng L, et al. Cs0.33WO3 as a high-performance transparent solar radiation shielding material for windows. Journal of Applied Physics. 2018;124.

[46] Tahmasebi N, Madmoli S, Farahnak P. Synthesis of cesium tungsten bronze nanofibers with different crystalline phases. Materials Letters. 2018;211:161-4.

[47] Liu J, Chen B, Fan C, Shi F, Ran S, Yang J, et al. Controllable synthesis of small size CsxWO3 nanorods as transparent heat insulation film additives. CrystEngComm. 2018;20:1509-19.

[48] Ran S, Liu J, Shi F, Fan C, Chen B, Zhang H, et al. Greatly improved heat-shielding performance of KxWO3 by trace Pt doping for energy-saving window glass applications. Solar Energy Materials and Solar Cells. 2018;174:342-50.

[49] Huang XJ, Bao J, Han Y, Cui CW, Wang JX, Zeng XF, et al. Controllable synthesis and evolution mechanism of tungsten bronze nanocrystals with excellent optical performance for energy-saving glass. Journal of Materials Chemistry C. 2018;6:7783-9.

[50] Hirano T, Nakakura S, Rinaldi FG, Tanabe E, Wang W-N, Ogi T. Synthesis of highly crystalline hexagonal cesium tungsten bronze nanoparticles by flame-assisted spray pyrolysis. Advanced Powder Technology. 2018;29:2512-20.

[51] Zhou Y, Li N, Xin Y, Cao X, Ji S, Jin P. CsxWO3 nanoparticle-based organic polymer transparent foils: low haze, high near infrared-shielding ability and excellent photochromic stability. Journal of Materials Chemistry C. 2017;5:6251-8.

[52] Chew C, Bishop P, Salcianu C, Carmalt CJ, Parkin IP. Aerosol-assisted deposition of gold nanoparticle-tin dioxide composite films. RSC Adv. 2014;4:13182-90.

[53] Carboni M, Carravetta M, Zhang XL, Stulz E. Efficient NIR light blockage with matrix embedded silver nanoprism thin films for energy saving window coating. Journal of Materials Chemistry C. 2016;4:1584-8.

[54] Tao P, Viswanath A, Schadler LS, Benicewicz BC, Siegel RW. Preparation and optical properties of indium tin oxide/epoxy nanocomposites with polyglycidyl methacrylate grafted nanoparticles. ACS Appl Mater Interfaces. 2011;3:3638-45.

[55] Shen B, Wang Y, Lu L, Yang H. Synthesis and characterization of Sb-doped SnO2 with high near-infrared shielding property for energy-efficient windows by a facile dual-titration co-precipitation method. Ceramics International. 2020;46:18518-25.

[56] Lee S-Y, Park B-O. Structural, electrical and optical characteristics of SnO2:Sb thin films by ultrasonic spray pyrolysis. Thin Solid Films. 2006;510:154-8.

[57] Kim D-W, Kim D-S, Kim Y-G, Kim Y-C, Oh S-G. Preparation of hard agglomerates free and weakly agglomerated antimony doped tin oxide (ATO) nanoparticles by coprecipitation reaction in methanol reaction medium. Materials Chemistry and Physics. 2006;97:452-7.

[58] Elangovan E, Ramamurthi K. A study on low cost-high conducting fluorine and antimony-doped tin oxide thin films. Applied Surface Science. 2005;249:183-96.

[59] Lu HF, Hong RY, Wang LS, Xie HD, Zhao SQ. Preparation of ATO nanorods and electrical resistivity analysis. Materials Letters. 2012;68:237-9.

[60] Ojha DP, Karki HP, Kim HJ. Design of ternary hybrid ATO/g-C3N4/TiO2 nanocomposite for visible-light-driven photocatalysis. Journal of Industrial and Engineering Chemistry. 2018;61:87-96.

[61] Yao Y, Chen Z, Wei W, Zhang P, Zhu Y, Zhao Q, et al. Cs0.32WO3/PMMA nanocomposite via in-situ polymerization for energy saving windows. Solar Energy Materials and Solar Cells. 2020;215.

[62] Liu G, Xu J, Li R. Chemical and morphological mechanisms of synthesizing rectangular cesium tungsten bronze nanosheets with broadened visible-light absorption and strong photoresponse property. Materials & Design. 2020;194.

[63] Xiao X, Huan C, Cheng H, Lu Y, Qi S, Zhan Y, et al. A novel method to improve phase transition of VO2 thermochromic films by Cs0.32WO3 nanoparticles. Materials Letters. 2019;249:95-8.

[64] Ran S, Liu J, Shi F, Fan C, Yang J, Chen B, et al. Microstructure regulation of CsxWO3 nanoparticles by organic acid for improved transparent thermal insulation performance. Materials Research Bulletin. 2019;109:273-80.

[65] Wei G, Yang D, Zhang T, Yue X, Qiu F. Fabrication of multifunctional coating with high luminous transmittance, self-cleaning and radiative cooling performances for energy-efficient windows. Solar Energy Materials and Solar Cells. 2019;202.

[66] Okada M, Ono K, Yoshio S, Fukuyama H, Adachi K. Oxygen vacancies and pseudo Jahn-Teller destabilization in cesium-doped hexagonal tungsten bronzes. Journal of the American Ceramic Society. 2019.

[67] Liang X, Guo C, Chen M, Guo S, Zhang L, Li F, et al. A roll-to-roll process for multi-responsive soft-matter composite films containing CsxWO3 nanorods for energy-efficient smart window applications. Nanoscale Horiz. 2017;2:319-25.

[68] Wu X, Yin S, Xue D, Komarneni S, Sato T. A Cs(x)WO3/ZnO nanocomposite as a smart coating for photocatalytic environmental cleanup and heat insulation. Nanoscale. 2015;7:17048-54.

[69] Liu J, Xu Q, Shi F, Liu S, Luo J, Bao L, et al. Dispersion of Cs0.33WO3 particles for preparing its coatings with higher near infrared shielding properties. Applied Surface Science. 2014;309:175-80.

[70] Yang C, Chen J-F, Zeng X, Cheng D, Cao D. Design of the Alkali-Metal-Doped WO3as a Near-Infrared Shielding Material for Smart Window. Industrial & Engineering Chemistry Research. 2014;53:17981-8.

[71] Mattox TM, Bergerud A, Agrawal A, Milliron DJ. Influence of Shape on the Surface Plasmon Resonance of Tungsten Bronze Nanocrystals. Chemistry of Materials. 2014;26:1779-84.

[72] Liu J, Luo J, Shi F, Liu S, Fan C, Xu Q, et al. Synthesis and characterization of F-doped Cs0.33WO3−F particles with improved near infrared shielding ability. Journal of Solid State Chemistry. 2015;221:255-62.

[73] Mattox TM, Agrawal A, Milliron DJ. Low Temperature Synthesis and Surface Plasmon

Resonance of Colloidal Lanthanum Hexaboride (LaB6) Nanocrystals. Chemistry of Materials. 2015;27:6620-4.

[74] Tang H, Su Y, Hu T, Liu S, Mu S, Xiao L. Synergetic effect of LaB6 and ITO nanoparticles on optical properties and thermal stability of poly(vinylbutyral) nanocomposite films. Applied Physics A. 2014;117:2127-32.

[75] Xiao L, Su Y, Zhou X, Chen H, Tan J, Hu T, et al. Origins of high visible light transparency and solar heat-shielding performance in LaB6. Applied Physics Letters. 2012;101.

[76] Chen C-J, Chen D-H. Preparation of LaB6 nanoparticles as a novel and effective near-infrared photothermal conversion material. Chemical Engineering Journal. 2012;180:337-42.

[77] Pasquarelli RM, Ginley DS, O'Hayre R. Solution processing of transparent conductors: from flask to film. Chem Soc Rev. 2011;40:5406-41.

[78] Tandon B, Ghosh S, Milliron DJ. Dopant Selection Strategy for High-Quality Factor Localized Surface Plasmon Resonance from Doped Metal Oxide Nanocrystals. Chemistry of Materials. 2019;31:7752-60.

[79] Zhou Y, Huang A, Luo H, Jin P. Localized surface plasmon resonance induced excellent solar-shielding ability for TiN nanoparticles-based hybrid polymer optical foils with high transparency. Journal of Alloys and Compounds. 2019;782:1087-93.

[80] Wang L, Zhu G, Wang M, Yu W, Zeng J, Yu X, et al. Dual plasmonic Au/TiN nanofluids for efficient solar photothermal conversion. Solar Energy. 2019;184:240-8.

[81] Staller CM, Robinson ZL, Agrawal A, Gibbs SL, Greenberg BL, Lounis SD, et al. Tuning Nanocrystal Surface Depletion by Controlling Dopant Distribution as a Route Toward Enhanced Film Conductivity. Nano Lett. 2018;18:2870-8.

[82] Kriegel I, Scotognella F, Manna L. Plasmonic doped semiconductor nanocrystals: Properties, fabrication, applications and perspectives. Physics Reports. 2017;674:1-52.

[83] Gu Y, Zhu Z, Song J, Zeng H. Triangle-, tripod-, and tetrapod-branched ITO nanocrystals for anisotropic infrared plasmonics. Nanoscale. 2017;9:19374-83.

[84] Crockett BM, Jansons AW, Koskela KM, Johnson DW, Hutchison JE. Radial Dopant Placement for Tuning Plasmonic Properties in Metal Oxide Nanocrystals. ACS Nano. 2017;11:7719-28.

[85] Rosli NN, Ibrahim MA, Ahmad Ludin N, Mat Teridi MA, Sopian K. A review of graphene based transparent conducting films for use in solar photovoltaic applications. Renewable and Sustainable Energy Reviews. 2019;99:83-99.

[86] Lyu J, Liu Z, Wu X, Li G, Fang D, Zhang X. Nanofibrous Kevlar Aerogel Films and Their Phase-Change Composites for Highly Efficient Infrared Stealth. ACS Nano. 2019;13:2236-45.

[87] Ma L, Wang J, Zhao F, Wu D, Huang Y, Zhang D, et al. Plasmon-mediated photothermal and superhydrophobic TiN-PTFE film for anti-icing/deicing applications. Composites Science and Technology. 2019;181.

[88] Chen Y, Zhu J, Ma H, Chen L, Li R, Jin P. VO2/Nickel-bromine-ionic liquid composite film for thermochromic application. Solar Energy Materials and Solar Cells. 2019;196:124-30.

[89] Jansons AW, Koskela KM, Crockett BM, Hutchison JE. Transition Metal-Doped Metal Oxide Nanocrystals: Efficient Substitutional Doping through a Continuous Growth Process. Chemistry of Materials. 2017;29:8167-76.

[90] Jung D, Kim U, Cho W. Fabrication of pure monoclinic VO2 nanoporous nanorods via a mild pyrolysis process. Ceramics International. 2018;44:6973-9.

[91] Henrist C, Toussaint C, de Vroede J, Chatzikyriakou D, Dewalque J, Colson P, et al. Surfactant-assisted ultrasonic spray pyrolysis of hematite mesoporous thin films. Microporous and Mesoporous Materials. 2016;221:182-6.

[92] Chatzikyriakou D, Maho A, Cloots R, Henrist C. Ultrasonic spray pyrolysis as a processing route for templated electrochromic tungsten oxide films. Microporous and Mesoporous Materials. 2017;240:31-8.

[93] Li C-P, Wolden CA, Dillon AC, Tenent RC. Electrochromic films produced by ultrasonic spray deposition of tungsten oxide nanoparticles. Solar Energy Materials and Solar Cells. 2012;99:50-5.

[94] Deokate RJ, Pawar SM, Moholkar AV, Sawant VS, Pawar CA, Bhosale CH, et al. Spray deposition of highly transparent fluorine doped cadmium oxide thin films. Applied Surface Science. 2008;254:2187-95.

[95] Li X-H, Liu C, Feng S-P, Fang NX. Broadband Light Management with Thermochromic Hydrogel Microparticles for Smart Windows. Joule. 2019;3:290-302.

[96] Gunay AA, Kim H, Nagarajan N, Lopez M, Kantharaj R, Alsaati A, et al. Optically Transparent Thermally Insulating Silica Aerogels for Solar Thermal Insulation. ACS Appl Mater Interfaces. 2018;10:12603-11.

[97] Nadarajah A, Carnes ME, Kast MG, Johnson DW, Boettcher SW. Aqueous Solution Processing of F-Doped SnO2 Transparent Conducting Oxide Films Using a Reactive Tin(II) Hydroxide Nitrate Nanoscale Cluster. Chemistry of Materials. 2013;25:4080-7.

[98] Dua L, Biswas PK. Synthesis and photoluminescence property of nanostructured sol–gel antimony tin oxide film on silica glass. Chemical Physics Letters. 2013;572:66-72.

[99] Luo L, Rossell MD, Xie D, Erni R, Niederberger M. Microwave-Assisted Nonaqueous Sol–Gel Synthesis: From Al:ZnO Nanoparticles to Transparent Conducting Films. ACS Sustainable Chemistry & Engineering. 2012;1:152-60.

[100] Reidinger M, Rydzek M, Scherdel C, Arduini-Schuster M, Manara J. Low-emitting transparent coatings based on tin doped indiumoxide applied via a sol–gel routine. Thin Solid Films. 2009;517:3096-9.

[101] Santos-Cruz J, Torres-Delgado G, Castanedo-Perez R, Zúñiga-Romero CI, Zelaya-Angel O. Optical and electrical characterization of fluorine doped cadmium oxide thin films prepared by the sol–gel method. Thin Solid Films. 2007;515:5381-5.

[102] Zhao G, Schwartz Z, Wieland M, Rupp F, Geis-Gerstorfer J, Cochran DL, et al. High surface energy enhances cell response to titanium substrate microstructure. J Biomed Mater Res A. 2005;74:49-58.

[103] Pinna N, Niederberger M. Surfactant-free nonaqueous synthesis of metal oxide nanostructures. Angew Chem Int Ed Engl. 2008;47:5292-304.

[104] Lu Y, Xiao X, Fu J, Huan C, Qi S, Zhan Y, et al. Novel smart textile with phase change materials encapsulated core-sheath structure fabricated by coaxial electrospinning. Chemical Engineering Journal. 2019;355:532-9.

[105] Luo L, Bozyigit D, Wood V, Niederberger M. High-Quality Transparent Electrodes Spin-Cast from Preformed Antimony-Doped Tin Oxide Nanocrystals for Thin Film Optoelectronics. Chemistry of Materials. 2013;25:4901-7.

[106] Sb-doped SnO, transparent conducting oxide from the sol-gel dip-coating technique.

[107] Ziming C, Fuqiang W, Dayang G, Huaxu L, Yong S. Low-cost radiative cooling blade

coating with ultrahigh visible light transmittance and emission within an “atmospheric window”. Solar Energy Materials and Solar Cells. 2020;213.

[108] DeForest N, Shehabi A, Selkowitz S, Milliron DJ. A comparative energy analysis of three electrochromic glazing technologies in commercial and residential buildings. Applied Energy. 2017;192:95-109.

[109] Shen B, Wang Y, Lu L, Yang H. Spraying fabrication of spectrally selective coating with improved near-infrared shielding performance for energy-efficient glazing. Ceramics International. 2021.

[110] Shen Y, Wu Y, Tao J, Zhu C, Chen H, Wu Z, et al. Spraying Fabrication of Durable and Transparent Coatings for Anti-Icing Application: Dynamic Water Repellency, Icing Delay, and Ice Adhesion. ACS Appl Mater Interfaces. 2019;11:3590-8.

[111] Maho A, Comeron Lamela L, Henrist C, Henrard L, Tizei LHG, Kociak M, et al. Solvothermally-synthesized tin-doped indium oxide plasmonic nanocrystals spray-deposited onto glass as near-infrared electrochromic films. Solar Energy Materials and Solar Cells. 2019;200.

[112] Ge D, Yang L, Wu G, Yang S. Spray coating of superhydrophobic and angle-independent coloured films. Chem Commun (Camb). 2014;50:2469-72.

[113] Ravichandran K, Philominathan P. Analysis of critical doping level of sprayed antimony doped tin oxide films. Journal of Materials Science: Materials in Electronics. 2010;22:158-61.

[114] Lee W-J, Sharp J, Umana-Membreno GA, Dell J, Faraone L. Investigation of crystallized germanium thin films and germanium/silicon heterojunction devices for optoelectronic applications. Materials Science in Semiconductor Processing. 2015;30:413-9.

[115] Jia S, Li G, Liu P, Cai R, Tang H, Xu B, et al. Highly Luminescent and Stable Green Quasi-2D Perovskite-Embedded Polymer Sheets by Inkjet Printing. Advanced Functional Materials. 2020;30.

[116] Sun G, Cao X, Zhou H, Bao S, Jin P. A novel multifunctional thermochromic structure with skin comfort design for smart window application. Solar Energy Materials and Solar Cells. 2017;159:553-9.

[117] Zhou A, Yu Z, Chow CL, Lau D. Enhanced solar spectral reflectance of thermal coatings through inorganic additives. Energy and Buildings. 2017;138:641-7.

[118] Liang R, Sun Y, Aburas M, Wilson R, Wu Y. Evaluation of the thermal and optical performance of thermochromic windows for office buildings in China. Energy and Buildings. 2018;176:216-31.

[119] Liang R, Sun Y, Aburas M, Wilson R, Wu Y. An exploration of the combined effects of NIR and VIS spectrally selective thermochromic materials on building performance. Energy and Buildings. 2019;201:149-62.

[120] Sun Y, Wu Y, Wilson R. A review of thermal and optical characterisation of complex window systems and their building performance prediction. Applied Energy. 2018;222:729-47.

[121] Jelle BP, Hynd A, Gustavsen A, Arasteh D, Goudey H, Hart R. Fenestration of today and tomorrow: A state-of-the-art review and future research opportunities. Solar Energy Materials and Solar Cells. 2012;96:1-28.

[122] Jelle BP. Solar radiation glazing factors for window panes, glass structures and electrochromic windows in buildings—Measurement and calculation. Solar Energy Materials and Solar Cells. 2013;116:291-323.

[123] Liu S, Du YW, Tso CY, Lee HH, Cheng R, Feng SP, et al. Organic Hybrid Perovskite (MAPbI3−xClx) for Thermochromic Smart Window with Strong Optical Regulation Ability, Low Transition Temperature, and Narrow Hysteresis Width. Advanced Functional Materials. 2021.

[124] Jiang S, Xu J, Miao D, Peng L, Shang S, Zhu P. Water-repellency, ultraviolet protection and infrared emissivity properties of AZO film on polyester fabric. Ceramics International. 2017;43:2424-30.

[125] Alonso-Álvarez D, Ferre Llin L, Mellor A, Paul DJ, Ekins-Daukes NJ. ITO and AZO films for low emissivity coatings in hybrid photovoltaic-thermal applications. Solar Energy. 2017;155:82-92.

[126] Miao D, Jiang S, Shang S, Chen Z. Infrared reflective properties of AZO/Ag/AZO trilayers prepared by RF magnetron sputtering. Ceramics International. 2014;40:12847-53.

[127] Hamza MK, Bluet JM, Masenelli-Varlot K, Canut B, Boisron O, Melinon P, et al. Tunable mid IR plasmon in GZO nanocrystals. Nanoscale. 2015;7:12030-7.

[128] Li Y-Q, Kang Y, Xiao H-M, Mei S-G, Zhang G-L, Fu S-Y. Preparation and characterization of transparent Al doped ZnO/epoxy composite as thermal-insulating coating. Composites Part B: Engineering. 2011;42:2176-80.

[129] Zhao Q, Fang Y, Qiao K, Wei W, Yao Y, Gao Y. Printing of WO3/ITO nanocomposite electrochromic smart windows. Solar Energy Materials and Solar Cells. 2019;194:95-102.

[130] Schimpf AM, Lounis SD, Runnerstrom EL, Milliron DJ, Gamelin DR. Redox chemistries and plasmon energies of photodoped In2O3 and Sn-doped In2O3 (ITO) nanocrystals. J Am Chem Soc. 2015;137:518-24.

[131] Liu H, Zeng X, Kong X, Bian S, Chen J. A simple two-step method to fabricate highly transparent ITO/polymer nanocomposite films. Applied Surface Science. 2012;258:8564-9.

[132] Khorshidi B, Hosseini SA, Ma G, McGregor M, Sadrzadeh M. Novel nanocomposite polyethersulfone- antimony tin oxide membrane with enhanced thermal, electrical and antifouling properties. Polymer. 2019;163:48-56.

[133] Wang X, Hu Y, Song L, Xing W, Lu H, Lv P, et al. Effect of antimony doped tin oxide on behaviors of waterborne polyurethane acrylate nanocomposite coatings. Surface and Coatings Technology. 2010;205:1864-9.

[134] Takeda H, Adachi K. Near Infrared Absorption of Tungsten Oxide Nanoparticle Dispersions. Journal of the American Ceramic Society. 2007;0:070922001254002-???

[135] Guo C, Yin S, Zhang P, Yan M, Adachi K, Chonan T, et al. Novel synthesis of homogenous CsxWO3 nanorods with excellent NIR shielding properties by a water controlled-release solvothermal process. Journal of Materials Chemistry. 2010;20.

[136] Adachi K, Asahi T. Activation of plasmons and polarons in solar control cesium tungsten bronze and reduced tungsten oxide nanoparticles. Journal of Materials Research. 2012;27:965-70.

[137] Adachi K, Ota Y, Tanaka H, Okada M, Oshimura N, Tofuku A. Chromatic instabilities in cesium-doped tungsten bronze nanoparticles. Journal of Applied Physics. 2013;114.

[138] Zhang L, Wang W, Sun S, Jiang D. Near-infrared light photocatalysis with metallic/semiconducting H x WO 3 /WO 3 nanoheterostructure in situ formed in mesoporous template. Applied Catalysis B: Environmental. 2015;168-169:9-13.

[139] Li Y, Wang J, Feng B, Duan K, Weng J. Synthesis and characterization of antimony-doped

tin oxide (ATO) nanoparticles with high conductivity using a facile ammonia-diffusion co-precipitation method. Journal of Alloys and Compounds. 2015;634:37-42.

[140] Xi G, Ye J. Ultrathin SnO2 nanorods: template- and surfactant-free solution phase synthesis, growth mechanism, optical, gas-sensing, and surface adsorption properties. Inorg Chem. 2010;49:2302-9.

[141] Peters K, Zeller P, Stefanic G, Skoromets V, Němec H, Kužel P, et al. Water-Dispersible Small Monodisperse Electrically Conducting Antimony Doped Tin Oxide Nanoparticles. Chemistry of Materials. 2015;27:1090-9.

[142] Choi DY, Kang HW, Sung HJ, Kim SS. Annealing-free, flexible silver nanowire-polymer composite electrodes via a continuous two-step spray-coating method. Nanoscale. 2013;5:977-83.

[143] Li Y, Liu J, Liang J, Yu X, Li D. Tunable solar-heat shielding property of transparent films based on mesoporous Sb-doped SnO(2) microspheres. ACS Appl Mater Interfaces. 2015;7:6574-83.

[144] Cai L, Wu X, Gao Q, Fan Y. Effect of morphology on the near infrared shielding property and thermal performance of K0.3WO3 blue pigments for smart window applications. Dyes and Pigments. 2018;156:33-8.

[145] Xu JM, Li L, Wang S, Ding HL, Zhang YX, Li GH. Influence of Sb doping on the structural and optical properties of tin oxide nanocrystals. CrystEngComm. 2013;15.

[146] Li N, Chang T, Gao H, Gao X, Ge L. Morphology-controlled WO3-x homojunction: hydrothermal synthesis, adsorption properties, and visible-light-driven photocatalytic and chromic properties. Nanotechnology. 2019;30:415601.

[147] Li Y, Wu X, Li J, Wang K, Zhang G. Z-scheme g-C3N4@CsxWO3 heterostructure as smart window coating for UV isolating, Vis penetrating, NIR shielding and full spectrum photocatalytic decomposing VOCs. Applied Catalysis B: Environmental. 2018;229:218-26.

[148] Guo C, Yin S, Yan M, Sato T. Facile synthesis of homogeneous CsxWO3 nanorods with excellent low-emissivity and NIR shielding property by a water controlled-release process. Journal of Materials Chemistry. 2011;21.

[149] Lu Y, Li Y, Wang Y, Zhang J. Two-photon induced NIR active core-shell structured WO3/CdS for enhanced solar light photocatalytic performance. Applied Catalysis B: Environmental. 2020;272.

[150] Wei W, Yao Y, Zhao Q, Xu Z, Wang Q, Zhang Z, et al. Oxygen defect-induced localized surface plasmon resonance at the WO3-x quantum dot/silver nanowire interface: SERS and photocatalysis. Nanoscale. 2019;11:5535-47.

[151] Yang C, Chen JF, Zeng X, Cheng D, Huan H, Cao D. Enhanced near-infrared shielding ability of (Li,K)-codoped WO3 for smart windows: DFT prediction validated by experiment. Nanotechnology. 2016;27:075203.

[152] Giannuzzi R, De Donato F, De Trizio L, Monteduro AG, Maruccio G, Scarfiello R, et al. Tunable Near-Infrared Localized Surface Plasmon Resonance of F, In-Codoped CdO Nanocrystals. ACS Appl Mater Interfaces. 2019;11:39921-9.

[153] Cho SH, Ghosh S, Berkson ZJ, Hachtel JA, Shi J, Zhao X, et al. Syntheses of Colloidal F:In2O3 Cubes: Fluorine-Induced Faceting and Infrared Plasmonic Response. Chemistry of Materials. 2019;31:2661-76.

[154] Swallow JEN, Williamson BAD, Whittles TJ, Birkett M, Featherstone TJ, Peng N, et al.

Self-Compensation in Transparent Conducting F-Doped SnO2. Advanced Functional Materials. 2018;28.

[155] Kang Y, Wu X, Gao Q. Plasmonic-Enhanced Near-Infrared Photocatalytic Activity of F-Doped (NH4)0.33WO3 Nanorods. ACS Sustainable Chemistry & Engineering. 2019;7:4210-9.

[156] Agrawal A, Singh A, Yazdi S, Singh A, Ong GK, Bustillo K, et al. Resonant Coupling between Molecular Vibrations and Localized Surface Plasmon Resonance of Faceted Metal Oxide Nanocrystals. Nano Lett. 2017;17:2611-20.

[157] Kim J, Agrawal A, Krieg F, Bergerud A, Milliron DJ. The Interplay of Shape and Crystalline Anisotropies in Plasmonic Semiconductor Nanocrystals. Nano Lett. 2016;16:3879-84.

[158] Jansons AW, Hutchison JE. Continuous Growth of Metal Oxide Nanocrystals: Enhanced Control of Nanocrystal Size and Radial Dopant Distribution. ACS Nano. 2016;10:6942-51.

[159] Mendelsberg RJ, McBride PM, Duong JT, Bailey MJ, Llordes A, Milliron DJ, et al. Dispersible Plasmonic Doped Metal Oxide Nanocrystal Sensors that Optically Track Redox Reactions in Aqueous Media with Single-Electron Sensitivity. Advanced Optical Materials. 2015;3:1293-300.

[160] Diroll BT, Gordon TR, Gaulding EA, Klein DR, Paik T, Yun HJ, et al. Synthesis of N-Type Plasmonic Oxide Nanocrystals and the Optical and Electrical Characterization of their Transparent Conducting Films. Chemistry of Materials. 2014;26:4579-88.

[161] Indium Tin Oxide Nanoparticles with Compositionally Tunable Surface Plasmon Resonance Frequencies in the Near-IR Region. 2009.

[162] Edwards PP, Porch A, Jones MO, Morgan DV, Perks RM. Basic materials physics of

transparent conducting oxides. Dalton Trans. 2004:2995-3002.

[163] Staller CM, Gibbs SL, Saez Cabezas CA, Milliron DJ. Quantitative Analysis of Extinction Coefficients of Tin-Doped Indium Oxide Nanocrystal Ensembles. Nano Lett. 2019;19:8149-54.

[164] Ye X, Fei J, Diroll BT, Paik T, Murray CB. Expanding the spectral tunability of plasmonic resonances in doped metal-oxide nanocrystals through cooperative cation-anion codoping. J Am Chem Soc. 2014;136:11680-6.

[165] Machida K, Okada M, Adachi K. Excitations of free and localized electrons at nearby energies in reduced cesium tungsten bronze nanocrystals. Journal of Applied Physics. 2019;125.

[166] Li Y, Cheng J, Liu Y, Liu P, Cao W, He T, et al. Manipulation of Surface Plasmon Resonance in Sub-Stoichiometry Molybdenum Oxide Nanodots through Charge Carrier Control Technique. The Journal of Physical Chemistry C. 2017;121:5208-14.

[167] Lounis SD, Runnerstrom EL, Llordes A, Milliron DJ. Defect Chemistry and Plasmon Physics of Colloidal Metal Oxide Nanocrystals. J Phys Chem Lett. 2014;5:1564-74.

[168] Li G, Zhang S, Guo C, Liu S. Absorption and electrochromic modulation of near-infrared light: realized by tungsten suboxide. Nanoscale. 2016;8:9861-8.

[169] Lee J-S, Liu H-C, Peng G-D, Tseng Y. Facile synthesis and structure characterization of hexagonal tungsten bronzes crystals. Journal of Crystal Growth. 2017;465:27-33.

[170] Zhao Z, Bai Y, Ning W, Fan J, Gu Z, Chang H, et al. Effect of surfactants on the performance of 3D morphology W18O49 by solvothermal synthesis. Applied Surface Science. 2019;471:537-44.

[171] Swallow JEN, Williamson BAD, Sathasivam S, Birkett M, Featherstone TJ, Murgatroyd PAE, et al. Resonant doping for high mobility transparent conductors: the case of Mo-doped

In2O3. Materials Horizons. 2020;7:236-43.

[172] Wu K, Xiang S, Zhi W, Bian R, Wang C, Cai D. Preparation and characterization of UV curable waterborne poly(urethane-acrylate)/antimony doped tin oxide thermal insulation coatings by sol-gel process. Progress in Organic Coatings. 2017;113:39-46.

[173] Zhang W, Jiang S, Lv D. Fabrication and characterization of a PDMS modified polyurethane/Al composite coating with super-hydrophobicity and low infrared emissivity. Progress in Organic Coatings. 2020;143.

[174] Wang Q, Li C, Xu W, Zhao X, Zhu J, Jiang H, et al. Effects of Mo-doping on microstructure and near-infrared shielding performance of hydrothermally prepared tungsten bronzes. Applied Surface Science. 2017;399:41-7.

[175] Althues H, Henle J, Kaskel S. Functional inorganic nanofillers for transparent polymers. Chem Soc Rev. 2007;36:1454-65.

[176] Al-Shukri AM. Thin film coated energy-efficient glass windows for warm climates. Desalination. 2007;209:290-7.

[177] Al-Kuhaili MF, Ahmad SHA, Durrani SMA, Faiz MM, Ul-Hamid A. Application of nickel oxide thin films in NiO/Ag multilayer energy-efficient coatings. Materials Science in Semiconductor Processing. 2015;39:84-9.

[178] Al-Kuhaili MF, Ahmad SHA, Durrani SMA, Faiz MM, Ul-Hamid A. Energy-saving spectrally-selective coatings based on MoO3/Ag thin films. Materials & Design. 2015;73:15-9.

[179] Jiang C, Cheng M, Liu H, Shao L, Zeng X, Zhang Y, et al. Fabricating Transparent Multilayers with UV and Near-IR Double-Blocking Properties through Layer-by-Layer Assembly. Industrial & Engineering Chemistry Research. 2013;52:13393-400.

[180] Shen B, Wang Y, Lu L, Yang H. pH-dependent doping level and optical performance of antimony-doped tin oxide nanocrystals as nanofillers of spectrally selective coating for energy-efficient windows. Ceramics International. 2021.

[181] Wu X, Wang J, Zhang G, Katsumata K-i, Yanagisawa K, Sato T, et al. Series of MxWO3/ZnO (M = K, Rb, NH4) nanocomposites: Combination of energy saving and environmental decontamination functions. Applied Catalysis B: Environmental. 2017;201:128-36.

[182] Tian N, Huang H, Guo Y, He Y, Zhang Y. A g-C3N4/Bi2O2CO3 composite with high visible-light-driven photocatalytic activity for rhodamine B degradation. Applied Surface Science. 2014;322:249-54.

[183] Gao Q, Wu X, Cai L. Dual functionality of K0.3WO3/Ag2O nanocomposites for smart window: Energy saving and visible photocatalytic self-cleaning performance. Solar Energy Materials and Solar Cells. 2019;196:111-8.

[184] Li Y, Li J, Zhang G, Wang K, Wu X. Selective Photocatalytic Oxidation of Low Concentration Methane over Graphitic Carbon Nitride-Decorated Tungsten Bronze Cesium. ACS Sustainable Chemistry and Engineering. 2019;7:4382-9.

[185] Yu J, Wang Y, Xiao W. Enhanced photoelectrocatalytic performance of SnO2/TiO2 rutile composite films. Journal of Materials Chemistry A. 2013;1.

[186] Zheng M, Ni J, Liang F, Wang M-C, Zhao X. Effect of annealing temperature on the crystalline structure, growth behaviour and properties of SnO2:Sb thin films prepared by radio frequency (RF)-magnetron sputtering. Journal of Alloys and Compounds. 2016;663:371-8.